

**ELECTROPULSING TO ASSIST CONVENTIONAL
MANUFACTURING PROCESSES**



*A dissertation submitted to
the Universitat Politècnica de Catalunya for the
degree of Doctor of Philosophy in Mechanical Engineering*

Antonio J. Sánchez Egea

Advisor: Hernán A. González Rojas

Barcelona, September 2015

*PhD program in Mechanical Engineering, Fluids and Aeronautics
Department of Mechanical Engineering
Universitat Politècnica de Catalunya*

Contents

Foreword	13
Acknowledgements	17
1 Introduction	19
1.1 Objectives	24
1.2 Scope	25
1.3 Thesis organization	26
1.4 Article authorship	27
1.5 Congress and research collaborations	28
1.6 Short research stays	29
2 Bottom bending process assisted by electropulsing	31
2.1 Introduction	31
2.2 Objective	32
2.3 Methodology	32
2.3.1 Microcurrent pulse generator	32
2.3.2 Experimental configuration	33
2.3.3 Thermal behavior	34
2.3.4 Numerical simulation	35
2.4 Results and discussion	36
2.4.1 Electroplastic effects	38
2.5 Conclusions	43
3 Round turning process assisted by electropulsing	45
3.1 Introduction	45
3.2 Objectives	46
3.3 Methodology	47
3.3.1 Experimental configuration	47
3.3.2 Microcurrent pulse generator	48
3.4 Results and discussion	49
3.4.1 Thermal behavior	49
3.4.2 Surface roughness	50
3.4.3 Material hardness	52
3.4.4 Power consumption	54
3.5 Conclusions	58

4	Wire drawing process assisted by electropulsing	59
4.1	Introduction	59
4.2	Objectives	60
4.3	Methodology	61
4.3.1	Experimental configuration	61
4.3.2	Electropulses generator	62
4.3.3	Numerical simulation	64
4.4	Results and discussion	65
4.4.1	Thermal behavior	65
4.4.2	Electropulsing effect	67
4.4.3	Mechanical behavior	70
4.4.4	Material hardness	72
4.5	Metallography	72
4.5.1	Microstructure	72
4.5.2	Material phase determination	74
4.5.3	Material texture	79
4.6	Conclusions	88
5	General Discussions	89
5.1	Thermal behavior	89
5.2	Electric material resistivity	93
5.3	Electroplastic threshold	94
5.4	Cutting tool	95
5.5	Material characterization	96
6	Conclusions and recommendations for future work	101
6.1	Conclusions	101
6.2	Contribution to research	102
6.3	Recommendations for future work	103
Appendix A	Electric configuration of a current pulse generator	105
A.1	Electropulses generator power circuit	105
A.1.1	Power supply	106
A.1.2	Stage of charging and safety	106
A.1.3	Stage of capacitor discharge	106
A.2	Trigger electropulses circuit	107
A.2.1	Electropulses generator with silicon thyristor	107
A.2.2	Power supply, safety relay and ventilation	108
A.2.3	Stage of signal filter and tension limitation	108
A.2.4	Electropulses generation stage	108
A.2.5	Electropulses generator controlled by power MOSFETs	109
A.2.6	Electropulses generation stage controlled by power MOSFETs	110
Appendix B	Mechanical formulation	113
Appendix C	Electropulses generator quotation	115

Appendix D Research activities schedule	119
Appendix E Short research stays	121
E.1 Short research stay at Pereira, Colombia	121
E.2 Short research stay at Santiago de Chile, Chile	124
E.3 Short research stay at Chicago, United States	127
Bibliography	129

List of Figures

1	Electropulse generator outline.	33
2	Bottom bending process schematic diagram and engineering drawing.	34
3	Electric signals of a electropulse.	34
4	Bottom bending process characterization at node P.	36
5	Computed effective plastic strain during the bottom bending process.	37
6	Von Mises stresses evolution during the bottom bending process.	38
7	Aluminium (a) and stainless steel (b) relative bending forces for the different electrically assisted configurations.	39
8	Bending process phase D (a), aluminium (b) and stainless steel (c) relative elastic bending forces at phase D.	41
9	Aluminium (a) and stainless steel (b) relative elastic bending forces for the different electrically assisted configurations.	42
10	Electrically assisted turning process schema.	48
11	Microcurrent pulse generator schema and EP profile.	49
12	Maximum registered thermal values.	49
13	Roughness values for SAE 1020 (a-b), SAE 1045 (c-d) and SAE 4140 (e-f).	51
14	Relative material hardness.	53
15	Active power consumption profile for the conventional and assisted turning process.	55
16	Power consumption comparison between conventional and assisted process for pulse durations of (a) 200 μs and (b) 50 μs	55
17	Mechanized workpiece geometric parameters.	57
18	Electrically assisted wire drawing process schema.	62
19	Microcurrent pulse generator schema and EPs profile.	63
20	Maximum electric output power configuration.	64
21	Maximum bulk temperature of the conventional and assisted processes.	66
22	Wire drawing forces for convectional and assisted processes.	67
23	Electroplastic experimental fitting coefficient.	69
24	Relative energy efficiency for the different assisted processes configurations.	70
25	Effective plastic strain and von Mises stress evolution along radial coordinate.	70
26	Tensile mechanical behavior of CD and EAD specimens.	71
27	Material hardness distribution along the cross sectional area.	72
28	Surface observation of B material (a), CD specimens (b), EAD specimens (c) and cracks found in the EAD specimens (d).	73
29	Etched microstructure of B (a), CD (b) and EAD (c) specimens.	74

30	(a) XRD profile of B, CD and EAD specimens. (b) Main differences of phases composition at $\gamma(111)$ and $\alpha(110)$	75
31	Preferential microstructural orientation for the B, CD and EAD specimens.	78
32	The Kikuchi bands registered during the EBSD with 20 kV field emission electron.	79
33	Grain boundaries and twins.	80
34	High-angle grain boundaries and low-angle grain boundaries distribution.	81
35	Surface normal-projected inverse pole figure microstructure mapping.	82
36	IPF scattering contribution of B, CD and EAD specimens.	83
37	Pole figure of as-received specimen.	84
38	Pole figure of conventional wire drawn specimen.	84
39	Pole figure of electrically assisted wire drawn specimen.	85
40	3D diffracted region representations with respect to the three Euler angles.	85
41	ODFs of as-received specimen.	86
42	ODFs of conventional wire drawn specimen.	87
43	ODFs of electrically assisted wire drawn specimen.	87
44	Infrared image of an electrically assisted round turning process.	89
45	Aluminium bending forces and elastic recovery forces. It is seen that the bending force drops when is applied a certain values of current density. That force drops affected by the current density varies from one material to another. In this case a current density of $25 A/mm^2$ reduces by 14% the necessary force to bend aluminium. While the elastic restoring force is significantly reduced, about 20% on average	95
46	SEM images of BUE and BUL in machined AA2014 (T4) alloy [49].	96
47	Surface defects on the 308L stainless steel.	97
48	Etched microstructure of as-received (left column), conventional wire drawn (middle column) and electrical-assisted wire drawn (right column) specimens.	97
49	Electric schema of the main electropulse generator.	105
50	Rectifier system output signal outline.	106
51	Capacitor output signal: electropulses.	107
52	Silicon thyristor trigger electropulses circuit schema.	108
53	Electropulses generation schema operate by a silicon thyristor.	109
54	Power MOSFETs trigger electropulses circuit schema.	110
55	Electronic region and output terminals to control the frequency discharge.	110
56	Electronic region and output terminals to control the pulse duration.	111
57	Research activities schedule.	120
58	Invitation letter signed by Dr. Valentina Kallewaard.	122
59	Short research stay certificate of Pereira, Colombia.	123
60	Invitation letter signed by Dr. Diego J. Celentano.	125
61	Short research stay certificate of Santiago de Chile, Chile.	126
62	Invitation letter signed by Dr. Jian Cao.	128

List of Tables

1	Material dimensions and transmitted peak current densities.	33
2	Mechanical parameters of 1050 aluminium alloy.	35
3	Materials chemical composition.	47
4	Turning operation parameters.	47
5	Electropulsing operation parameters and maximum bulk temperature.	48
6	Energy consumed and saved under different electric configuration.	56
7	Specific cutting energy percentage reduction.	58
8	Materials chemical composition and initial diameter.	61
9	Drawing operation parameters.	61
10	Electropulsing operation parameters.	61
11	Material parameters of 308L alloy used in the numerical simulation processes.	65
12	XRD contribution for the different studied specimens.	77
13	Percentage of volume fraction of each phase for the different studied specimens.	77
14	Analysis of the preferential microstructural orientation in austenite phase.	78
15	Grain dimensions and area measure in the three specimens.	81
16	Electric properties of a 308L stainless steel.	91
17	Thermal properties of the air at 160 °C and 1 bar.	93
18	The main characteristics of the bottom bending and wire drawing finite element simulations.	114
19	Electronic components list needed for a electropulse generator.	116
20	Personal list for manufacturing a current pulse generator.	117

Foreword

This thesis presents a study on the variation of the mechanical properties of some materials. These variations are registered for processes as bottom bending, wire drawing or round turning, which are performed under high density electropulses. This research implied the study of several issues related to the manufacturing processes and the electric pulses. For example, some isolated systems are developed for each process. This is required for protecting the monitoring devices and machinery from electric drifts.

On the other hand, several electropulse generators are designed and manufactured to electrically assist the aforementioned manufacturing processes. The electrical connectors is the main technological issue in each process to ensure good electrical contact during experimentation. Once the manufacturing setup is under control, electropulses are applied on various materials whilst its physical properties are measured and recorded. In particular, the processes are achieved under different electric configurations to infer the influence of the electropulses. The obtained results show that different mechanical and manufacturing properties like elastic restoring forces, yield strength, power consumption, surface roughness and material hardness among others are modified when the manufacturing process is assisted with a pulsed electric field. Additionally, the machinability and formability is improved when the metallic material is affected by current pulses. However, it should be noted that the mechanical properties behavior under different electrical parameters, like current density, frequency discharge and pulse duration, is complex and does not follow an expected relationship. Furthermore, numerical simulation analyses is required to study and understand the complex behavior of the mechanical properties.

The manufacturing process of bending, machining and drawing process was done at the Universitat Politècnica de Catalunya (Spain) in collaboration with the Northwestern University (USA), the Universidad Pontificia Universidad Católica de Chile (Chile) and the Universidad Tecnológica de Pereira (Colombia). This thesis is funded by the Ministry of Economy and Competitiveness of Spain, reference project: DPI2011-26326 (grant no. BES-2012-056760).

Along the document detailed information on methodology for the aforementioned processes and some conclusions are provided.

Prefaci

En aquesta tesi s'estudia la variació de les propietats mecàniques en diversos materials. Aquestes variacions són registrades en diversos processos de fabricació com el doblegat, mecanitzat i trefilat, quan aquests processos són assistits amb generadors d'electropulsos d'alta densitat de corrent. Aquesta investigació comporta l'estudi de diversos problemes tecnològics relacionats amb processos de fabricació assistits amb corrent elèctric. Com per exemple, haver de desenvolupar sistemes específics d'aïllament per a cada procés. Això és necessari per protegir els equips de monitorització i les màquines davant dels corrents de deriva.

D'altra banda, diversos generadors d'electropulsos han estat dissenyats i fabricats per assistir elèctricament els processos de fabricació esmentats. El contacte elèctric és el principal problema tecnològic a resoldre en cada procés per assegurar el pas de corrent durant l'experimentació. Una vegada que el procés és configurat, s'indueixen polsos de corrent elèctric en diferents materials per enregistrar el comportament d'algunes propietats físiques. En particular, els processos s'assisteixen amb diferents configuracions elèctriques per determinar la influència en cada cas dels polsos elèctrics. Els resultats obtinguts mostren que les propietats mecàniques i de fabricació, com les forces de recuperació elàstica, límit elàstic, potència consumida, rugositat superficial i la duresa superficial entre altres presenten diferències quan el procés de fabricació és assistit amb un corrent elèctric polsant. En resum, s'observa que la maquinabilitat i conformabilitat del material metàl·lic millora quan és fabricat sota la influència dels polsos elèctrics. Tot i això, cal indicar que el comportament de les propietats mecàniques anteriors sota els termes elèctriques són complexes i no segueixen una relació trivial. Per això, s'ha necessitat de programes de simulació numèrica per estudiar i comprendre el comportament de les propietats mecàniques.

Els processos de fabricació de doblegat, mecanitzat i trefilatge han estat realitzats a la Universitat Politècnica de Catalunya (Espanya) amb col·laboració de la Northwestern University (Estats Units), la Pontificia Universitat Catòlica de Xile (Xile) i la Universitat Tecnològica de Pereira (Colòmbia). Aquesta tesi ha estat finançada pel Ministeri d'Economia i Competitivitat d'Espanya amb referència DPI2011-26326 (nombre de concessió BES-2012-056760).

Al llarg del document es detalla la metodologia d'estudi dels diferents processos esmentats i es constaten algunes conclusions.

Prefacio

En esta tesis se estudia la variación de las propiedades mecánicas en varios materiales. Estas variaciones son registradas en diversos procesos de fabricación como doblado, mecanizado y trefilado, cuando estos procesos son asistidos con generadores de electropulsos de alta densidad de corriente. Esta investigación conlleva el estudio de varios problemas tecnológicos relacionados con procesos de fabricación y pulsos eléctricos. Como por ejemplo desarrollar sistemas de aislación para cada proceso. Esto es requerido para proteger los equipos de monitorización y las máquinas de las corrientes de deriva.

Por otro lado, varios generadores de electropulsos han sido diseñados y fabricados para asistir eléctricamente los procesos de fabricación mencionados. El contacto eléctrico es el principal problema tecnológico a resolver en cada proceso para asegurar el paso de corriente durante la experimentación. Una vez que el proceso es configurado, se inducen pulsos de corriente eléctrica en diferentes materiales para registrar el comportamiento de algunas propiedades físicas. En particular, los procesos se asisten con diferentes configuraciones eléctricas para determinar la influencia en cada caso de los pulsos eléctricos. Los resultados obtenidos muestran que las propiedades mecánicas y de fabricación, como las fuerzas de recuperación elástica, límite elástico, potencia consumida, rugosidad superficial y la dureza superficial entre otras presentan diferencias cuando el proceso de fabricación es asistido con una corriente eléctrica pulsante. En resumen, se observa que la maquinabilidad y conformabilidad del material metálico mejora cuando es fabricado bajo la influencia de los pulsos eléctricos. Aun así, cabe indicar que el comportamiento de las propiedades mecánicas anteriores bajo las condiciones eléctricas son complejas y no siguen una relación trivial. Por ello, se ha necesitado de programas de simulación numérica para estudiar y comprender el comportamiento de las propiedades mecánicas.

Los procesos de fabricación de doblado, mecanizado y trefilado han sido realizados en la Universitat Politècnica de Catalunya (España) en colaboración con la Northwestern University (Estados Unidos), la Pontificia Universidad Católica de Chile (Chile) y la Universidad Tecnológica de Pereira (Colombia). Esta tesis ha sido financiada por el Ministerio de Economía y Competitividad de España con referencia: DPI2011-26326 (número de concesión BES-2012-056760).

A lo largo del documento se detalla la metodología de estudio de los diferentes procesos mencionados y se constatan algunas conclusiones.

Acknowledges

First of all, I want to express my sincerity and deeply acknowledgement to my thesis director Dr. Hernán Alberto González Rojas. Thanks for bringing me the opportunity to take part in such a challenging project. Your valuable tutorship, dedication and patience along these years have made possible the development of the present work.

It is acknowledged the important contribution done by the entire DEFAM group and the collaboration of Dr. Diego J. Celentano, Dr. Jian Cao, Dr. Valentina Kallewaard and M.Sc. Carlos A. Montilla. All these people have accomplished an essential role in this thesis. They have also created an optimum social and work environment.

My gratitude to the Universitat Politècnica de Catalunya, Northwestern University, Pontificia Universidad Católica de Chile and the Universidad Tecnología de Pereira for letting me develop and improve my professional and scientific career.

Thanks to the Ministry of Economy and Competitiveness by the research scholarship, reference project DPI2011-26326 (grant no. BES-2012-056760). That financial award has covered my research duties during 48 months.

Lastly, I would like to give a special mention to my family Clemen, Alonso, Pablo and Elena, either my couple Lidia. In spite of the distance, they have supported, inspired and encouraged me at any time. I hope to enjoy yourselves during many more years and share many others successes and joys.

My profoundly gratitude to all the people mentioned here and those non mentioned that I worked with along the way.

Chapter 1

Introduction

The electroplasticity phenomenon is linked to both thermal and athermal effects. This phenomenon was firstly described by Troitskii and Likhtman (1963) [1] and subsequently explained theoretically by Troitskii (1969) [2]. In his last work, he investigated the influence of electric current pulses on the plastic strain behavior of a material. At the same time, magnetic and electric fields were studied to modify the material lattice. First, Kravchenko (1967) [3] proved that there is a dislocation movement in both metals and semiconductors when an external magnetic field was applied. Later, Conrad (2000) [4] showed the influence of an electric field on the plastic strain of metals and ceramic materials. Afterwards, Conrad (2001) [5] showed that electroplasticity could be largely promoted by dragging dislocations to the interstitial space among the grains of the microstructure of the material. The dislocation movement leads to the modification of material microstructure, changing the dimensions of interstitial gaps. Such microstructure variation changes the mechanical properties of the material.

Currently, despite the research carried out, the physic aetiology of electroplasticity phenomenon is not fully defined. The most recent mechanisms are presented here to give an explanation about the metallurgical and mechanical behavior of the physical properties of a given material under the influence of an electromagnetic field coupled to thermal and athermal effects. To understand these mechanisms it is necessary to grasp the theoretical models for the interaction between thermal and athermal electroplastic effects.

Theoretical models of electroplasticity

Theoretical models of electroplasticity can be grouped according to skin and pinch effects, thermal effects and electron wind effect. Each material effect will be explained independently by assuming the possibility of coexistence in several sections simultaneously.

Skin and pinch effects:

The skin effect is based on the induced electric current concentration at the material surface layers. Okazaki et al. (1980) [6] parametrized the skin effect depth by δ . This parameter can be calculated as follows:

$$\delta = \frac{\pi \cdot f \cdot \mu^{-1/2}}{\rho},$$

where f is frequency discharge, μ is permeability and ρ is electric resistivity.

This theory was rejected by Conrad and coworkers, Sprecher (1986) [7], who proved that the electric current distribution is uniform along the material cross sectional area. Furthermore, they also demonstrated that the electric current induction generates a pinch effect. That effect causes radial compression stress which is described by $\Delta\sigma_{pinch}$. This quantity is given by:

$$\Delta\sigma_{pinch} = \nu \cdot \mu \cdot J^2 \cdot \frac{a^2}{2},$$

where ν is the Poisson coefficient, a is the specimen radius and J is the current density.

These compression stresses are insignificant compared with the stresses arising from plastic deformations of the material. However, at a microscopic level these stresses can enhance the twin and atoms mobility and reduce the strength of the obstacles opposing dislocation motion. These two factors can induce a local recrystallization in the material lattice, as Song and Wand (2011) [8] reported.

Thermal effect:

The thermal effect is based on the Joule effect and it is the most significant effect in the electroplasticity phenomenon. The observation scale on the study of thermal expansion should be taken into account since the bulk temperature (macro scale) could be negligible. However, at the microscopic level, the instantaneous values of phase transition temperature could be achievable. Conrad and Sprecher (1989) [9] and Okazaki et al. (1980) [6] estimated the thermal expansion assuming an adiabatic case, as described in the following equation:

$$\Delta T = \frac{\rho \cdot J^2 \cdot t_p}{C_p \cdot d},$$

where ρ is the resistivity, t_p is the pulse duration, C_p is the specific heat, d is density and J is current density.

Thermal expansion for electrically assisted specimens has a very short response time compared with the conventional thermal treatments. Due to this reason, Tang et al. (1993) [10] studied that instantaneous thermal expansion caused by current pulses induces compressive stress in the material lattice. This stress, σ_{max} , is given by

$$\sigma_{max} = E \cdot \alpha \cdot \Delta T,$$

where E is Young's modulus, α is the thermal expansion coefficient and ΔT is the instantaneous thermal difference.

Goldman et al. (1981) [11] and Timsit (1981) [12] considered that the thermal effect in the electroplasticity phenomenon is just the effect that modifies the material properties,

although an extensive experimental literature proved the importance of athermal effects in the electroplasticity phenomenon. Those effects have been described by Troitski (1985) [13], Okazaki et al. (1980) [6] and Sprecher et al. (1986) [7]. They showed that athermal effects facilitate an atomic diffusion which will be addressed in the following subsection.

Electron wind effect:

The electron wind theoretical model was initially described by Kravchenko (1966) [14] and is based on the atomic diffusion phenomenon. The electron wind effect consists in a force that goes through the material, the force is expressed as the impact interaction between electrons and atoms. The electron wind force can be estimated by the following equation:

$$F_{ew} = e \cdot n_e \cdot J \cdot \frac{\rho}{N_D},$$

where F_{ew} is electron wind force per unit dislocation length, (ρ/N_D) is the specific resistivity per unit dislocation length, N_D dislocation density and n_e is the electron density.

Conrad and Sprecher (1989) [9], Yang and Conrad (2001) [15], Antolovich and Conrad (2004) [16] and Conrad (2002) [17] reported an increase of material plasticity mainly due to the dislocation movements. Those dislocation movements depend on the induced electromagnetic field, which increases the lattice mobility defined by the interaction between electrons and atoms of the material. The interaction causes the stacking fault energy of material changes to a lower energy state and facilitates the dislocation movements towards the grain boundaries, Conrad (2001) [5].

However, Molotskii and Fleurov (1995) [18] proved that the electron wind force could be neglected when compared with the forces required for plastic deformation in material due to the different order of magnitude. Those authors reported a theory in which the material lattice mobility is caused by a magnetic field, related to the induced electric field. That magnetic field generates a shear force (pinch effect) in the material and facilitates the dislocation movements. However, that shear force can be considered significant only when ferromagnetic materials are studied.

Although all these theoretical models have been thoroughly studied, they still are far from entirely defining the electroplasticity phenomenon by themselves. Several mechanisms have been proposed based on those theories that tried to explain the influence of thermal and athermal effects in a more complex manner.

Electroplasticity mechanisms phenomenon

The most referenced mechanisms of electroplasticity phenomenon explain the increase of vacancies mobility in the crystal lattice when an electric field is induced through the material. These mechanisms state that the dynamic recrystallization of the material could take place at a relatively low temperature due to coupling action of thermal and athermal effects, as it was noted by Xu et al. (2007) [19]. The material recrystallization can be defined as an increase of vacancies mobility activation, which can be achieved through an increase of crystal

lattice energy state. That change of energy state, which subsequently defines the interaction probability between electrons and atoms, is estimated by the electrons induced to the crystal lattice. Conrad and Sprecher (1989) [9] proved that the total atomic flux can be estimated by the vacancies activation as follow:

$$j = \frac{D_1}{k \cdot T} \cdot (\tau \cdot \Omega + K_{ew} \cdot \Omega \cdot J_m + N_1 \cdot \rho \cdot e \cdot Z_1^* \cdot J_m),$$

where D_1 is the lattice diffusion coefficient, k is the Boltzmann constant, T is the absolute temperature, t is external stress, Ω is the atom volume, K_{ew} is the coefficient of electron wind force, J_m is the amplitude of current density of electropulsing, N_1 is the number of lattice atoms per unit volume, and eZ_1^* is the effective charges of lattice atoms.

Despite being a model that fits well with the experimental behavior, the order of magnitude of the theoretical values is lower than that found through the experimental tests, as it was proved by Molotskii and Fleurov (1995) [18]. Therefore, it is understood that other relevant factors must also affect the atomic diffusion.

Another mechanism that has been considered studied the magnification of the thermal and athermal effects during the plastic deformation of the material. When plastic deformation occurs, an increase of structural defects appears in material microstructure. These defects change the grain size, dislocations, grain boundaries, twins, vacancies, inclusions, etc. They also affect the material microstructure heterogeneous distribution and the material electrical resistivity. Doherty et al. (1997) [20] reviewed that the thermal and athermal effects are pronounced at those material structural defects during deformation, primarily attributable to a material resistivity modification. The athermal and thermal effects influence on the stress variation can be obtained as follows:

$$\Delta P = P_{th} + P_{ath},$$

where P_{th} is the thermal compressive stress due to local thermal expansion, while P_{ath} is the electron wind force.

By expanding these two terms, the parameters that influence the thermal and athermal electroplastic effects are observed:

$$\Delta P = \left(\frac{2a \cdot \Delta S \cdot \nabla T}{\varphi} \right) + \left(\frac{\rho_D}{N_D} \cdot e \cdot n_e \cdot j \right),$$

where ΔS is the difference in the entropy between the grain boundary and crystal (approximately equal to entropy of melting), ∇T is the temperature gradient, $2a$ is the thickness of the grain boundary, φ is the atomic volume, ρ_D/N_D is the specific resistivity per unit dislocation length, N_D is the dislocation density, n_e is the electron density, and j is the current density.

The results indicated that thermal and athermal effects considerably increase the structural defects such as grain boundaries and dislocations. As a consequence, an increase of stack fault energy state and defects migration towards grain boundaries can be found. Those

two indicators imply that a dynamic recrystallization could take place at a relatively low temperature. It is assumed that the temperature may grow up to significant values in a micro scale level due to material resistivity changes.

Furthermore, there exist some studies on how current a phase transformation on a given material. For example, Conrad (2000) [4] and To et al. (2009) [21] reported that there are two stages in which phase transformation is conducted due to the influence of current pulses. The first stage is the material transformation to a saturate state, similar to a tempering treatment. Then, the second stage is the reverse process, the material lattice changes from a stable state to a superior thermal state. The energies that lead to the phase transformation are composed by Gibbs free energy, deformation energy, surface energy, Gibbs energy induced by the current pulses, among others terms.

$$\Delta G = \Delta G_{chem} + \Delta G_{stress} + \Delta G_{surface} + \Delta G_{EP} + \dots,$$

where Gibbs free energy (ΔG_{chem}) is the main factor for a material phase transformation. The stress and surface energies (ΔG_{stress} , $\Delta G_{surface}$) state depends on the material initial intrinsic stress, which is related to the manufacturing process used. Finally, the Gibbs energy induced by the current pulses ΔG_{EP} is an additional energy to force the material phase transformation.

From a thermodynamic point of view, Jiang et al. (2009) [22] found that the athermal effects can be relevant only when minimum thermal conditions are achieved, such as in this case, the interaction between electrons and atoms will generate a greater atomic flux in the material lattice.

Despite the recent progresses, these mechanisms are far from fully defining the complex mechanical and metallurgical variations of material under electroplastic effects. Therefore, extensive studies are required at an atomic scale to be able to explain the influence of current pulses on the material lattice and mechanical properties, as well as to improve on the proposed mechanisms.

Nevertheless a large number of experimental publications have proved that electroplasticity has a direct industrial impact, as stated in Guan et al. (2010) [23], being a suitable tool to assist conventional forming and machining processes. The substantial interest of this technique is the ability to modify the mechanical properties of the material during processing. For example, Magargee et al. (2013) [24] reported that a current density of 16 A/mm^2 could reduce the true stress in an electrically-assisted tensile test by nearly 50%; Roth et al. (2008) achieved around 400% material elongation by applying a pulsed current to tensile specimens; Zhang et al. (2002) [25] proved that electroplasticity can reduce the drawing stress and yield stress at an industrial wire-drawing speed; Stolyarov (2009) [26] determined that ultimate tensile strength decreased while ductility increased; Xu et al. (2007) [19] reported that electroplasticity induces microstructure modifications by reducing the annealing process; Tang et al. (2000) [27] concluded that elongation increased and reduced the resistivity of cold-draw steel, raising its productivity and Heigel et al. (2005) [28] studied that electric

currents through 6160 aluminium workpiece reduced the presence of Mg_2Si among others precipitates. The energy reduction required to perform the tensile test can be explained by the precipitates absorption.

The above mentioned studies have demonstrated that the application of an electric current on the material reduces the force needed to produce plastic strain, although the main cause of the reduction is the thermal electroplasticity effect. During experimentation the variations of the properties of material such as yield strength, ultimate tensile strength, ductility and elongation are closely related to the type of material, the amount of accumulated plastic deformation and the current intensity flowing through the material. The impact of the athermal effects on these mechanical and metallurgical properties remains under investigation.

The present study focuses on the electroplastic effects. Several short current pulses generators were designed and manufactured. The aim was to induce electric field through different metallic specimens, whilst undergoing a bottom bending, a round turning and wire drawing processes. The main objective of the study is to analyze the impact of the electroplastic effects on the mechanical and metallurgical properties of different materials.

The main objective and the specific objectives of this research are listed on the following section.

1.1 Objectives

The main goal of this study is to study the manufacturing improvements when different industrial processes are assisted with several electropulses configurations. This will help to solve conventional manufacturing issues. The manufacturing processes studied are: bottom bending, round turning and wire drawing processes. All of these processes are electrically assisted with short time current pulses to reduce the thermal effects (Joule effect) and to focus on the athermal effects.

In order to accomplish the main goal of the study the following specific objectives were also focused upon.

- Design and manufacture an electrical isolation system for each manufacturing process. Also to establish a signal processing data procedure to register the desired working parameters for each manufacturing process.
- Minimize the thermal effects (Joule effect). To do so, short time electropulses generators were designed and manufactured for each specific manufacturing process. It must be ensured that athermal effects have an influence on the mechanical behavior variation when the processes are assisted.

- Compare the conventional bottom bending process with the bottom bending process assisted by electropulsing. The aim here is to determine the bending forces and elastic recovery forces variation for the conventional and the assisted process.
- Study the round turning process when it is assisted with different electropulses conditions and estimate the impact on the surface roughness, material hardness and the power consumption in each case. The manufacturing improvements are compared with the conventional round turning process.
- Examine the mechanical and metallurgical behavior when the wire drawing process is assisted with different electropulsing configurations. Here the aim is to focus on the material formability enhancements. It is also analyzed the power consumption variation for the different electrical configurations.

Collectively, the specific objectives aim to prove that the short electropulses induction is a powerful and novel technique, which could help to solve conventional manufacturing process issues.

1.2 Scope

While the main goal of the study is to improve the conventional manufacturing processed with the electropulses influence, the scope of the study is listed in different activities as follows:

- a. Design and manufacture different current pulses generators to assist conventional manufacturing machines. The electrical working parameters needed are the following ones:
 - a.1. Current pulse intensity range from 90 to 300 A.
 - a.2. Frequency range from 100 to 400 Hz.
 - a.3. Current pulse duration range from 50 to 250 μ s.
- b. Design and manufacture specific electrical isolation system for each manufacturing process. This isolation system will prevent the machine and the researcher from suffering any accident when an electrical current field is induced.
- c. An experimental methodology is followed with several equipments to control and record electrical and mechanical parameters.
 - c.1. The electrical parameters are monitored by an oscilloscope and a multimeter with frequency meter. The power consumption is recorded with a quality energy analyser.

(<http://dx.doi.org/10.1016/j.jmatprotec.2015.03.018>).

Journal ranking position (Manufacturing Engineering category): 9th out of 82th at Q1 and 9th out of 415th from total. The ranking information is obtained from SCImago Journal and Country Rank. (<http://www.scimagojr.com/>).

Impact factor: 2.236 (estimated in 2014).

- III.** Chapter 4: This chapter addresses the mechanical behavior of the wire drawing process assisted with different electropulsing configurations. The impact of the current pulses on the mechanical and metallurgical properties is studied. This article has been sent to the Materials and Design and is currently under review.

Journal ranking position (Mechanics of Materials category): 10th out of 78th at Q1 and 10th out of 309th from total. The ranking information is obtained from SCImago Journal and Country Rank. (<http://www.scimagojr.com/>).

Impact factor: 2.335 (estimated in 2014).

- IV.** Chapter 5: This chapter contains the main discussion of the limitations behind the methodology and results of this thesis.

- V.** Chapter 6: This chapter summarize the main conclusions of this thesis. As well as future research activities that could be achieved in the following years.

1.4 Article authorship

Chapter 2 has been published in the Journal of Materials Processing Technology in April 2014. The experimental procedure was done by M.Sc. Antonio Sánchez and Dr. Jordi Llumà, the current generator was designed and manufactured by Dr. Hernán González, the numerical mechanical approximation was implemented by Dr. Diego Celentano, the signal data processing was done by M.Sc. Antonio Sánchez and the article composition was done by M.Sc. Antonio Sánchez and Dr. Jordi Llumà, the article review was achieved by Dr. Hernán González, Dr. Jose A. Travieso, Dr. Diego Celentano and Dr. Jordi Llumà.

Chapter 3 has been published in the Journal of Materials Processing Technology in March 2015. The experimental procedure was done by M.Sc. Antonio Sánchez, M.Sc. Carlos Montilla and Dr. Valentina Kallewaard, the current generator was designed and manufactured by Dr. Hernán González, the signal data processing was performed by M.Sc. Antonio Sánchez and M.Sc. Carlos Montilla, the article composition was done by M.Sc. Antonio Sánchez and the article review was performed by Dr. Hernán González.

Chapter 4 has been submitted in the Journal of Materials Processing Technology in August 2015. The experimental procedure was done by M.Sc. Antonio Sánchez, the current

generator was designed and manufactured by Dr. Hernán González, the numerical mechanical approximation was implemented by Dr. Diego Celentano, the microstructure observation, x-ray diffraction and electron backscatter diffraction analyses were conducted by Dr. Jordi Jorba and M.Sc. Antonio Sánchez, the signal data processing and the article composition was done by M.Sc. Antonio Sánchez, Dr. Diego Celentano and Dr. Jordi Jorba, the article composition was done by M.Sc. Antonio Sánchez and the article review was achieved by Dr. Hernán González, Dr. Jordi Jorba and Dr. Diego Celentano.

1.5 Congress and research collaborations

Listed below there are other research activities done during the research fellowship.

Congress:

"Bottom bending process assisted by short current pulses - characterization via numerical simulation". WCCM XI - 11th World Congress on Computational Mechanics. Barcelona, 20-25/07/2014.

"Study of surface roughness and hardness in workpieces machining by a turning process assisted by electroplasticity". AMDM 2014, International Conference on Advanced Mechanics, Design and Manufacturing Technology. Bogotá, 22-24/10/2014.

"Improvement of cold wire drawing process by electropulsing". 6th International Conference of the Manufacturing Engineering Society (MESIC). Barcelona, 22-24/ 07/2015.

"Turning process assisted in situ by short time current pulses". 6th International Conference of the Manufacturing Engineering Society (MESIC). Barcelona, 22-24/ 07/2015.

Research collaborations:

- Article's collaboration: *Predictive model for polishing times in mould finishing*. This article has been sent to the Tribology International Journal, it is currently under review.

Journal ranking position (Material Engineering category): 32th out of 81th at Q1 and 32th out of 359th from total. The ranking information is obtained from SCImago Journal and Country Rank. (<http://www.scimagojr.com/>).

Impact factor: 1.936 (estimated in 2014).

- Article's collaboration: *Electroplastic cutting influence on power consumption during drilling process*. This article has been sent to International Journal of Advanced Manufacturing Technology, it is currently under review.

Journal ranking position (Manufacturing Engineering category): 34th out of 82th at Q1 and 34th out of 415th from total. The ranking information is obtained from SCImago Journal and Country Rank. (<http://www.scimagojr.com/>).
Impact factor: 1.458 (estimated in 2014).

1.6 Short research stays

1. Two months research stay at the Mechanical Department in the Technological University of Pereira in Colombia, under Dr. Valentina Kalleward supervision. There, the turning process electrically assisted experiments was done. Dates: from 01/10/2013 to 30/11/2013.
2. Four months research stay at the Mechanical and Metallurgic Department in the Pontifical Catholic University of Chile in Chile, under Dr. Diego J. Celentano supervision. There, the drawing process electrically assisted experiments and the numerical model validation was done. Dates: from 01/04/2014 to 31/07/2014.
3. Four months research stay at the Mechanical Department in the Northwestern University in the United States, under Dr. Jian Cao supervision. There, the incremental forming process electrically assisted experiments and the numerical model validation are proposed. Dates: from 15/08/2014 to 15/12/2014.

Chapter 2

Bottom bending process assisted by electropulsing

In this chapter is studied the influence of the electropulsing influence on the bottom bending process when the Joule effect is minimized to negligible values. To do so a current pulse generator is designed and manufactured. Different materials are studied like sheets of 1050-H18 aluminium alloy and X5CrNi18-10 stainless steel. A finite element software is used to characterize the different phases of the mechanical behavior during the bottom bending process. The influence of current pulses on different bending phases is studied, specifically on the elastic restoring force and the maximum effective plastic strain condition. Compared to the conventional process, the results of the electrically assisted bending process show that the bending forces drop up to 18% in aluminium and 6% in stainless steel. In addition the elastic restoring force is also reduced up to 21% in aluminium and 12% in stainless steel. Therefore it can be concluded that electropulsing treatment have an influence on the material formability.

2.1 Introduction

Bending is the simplest operation process commonly used on the manufacturing industry. In this metal working process by which a straight length is transformed into a curved length. To do that, the material plastic strain in this process is allocated on the contact area, where the die impresses its shape on the sheet metal. The contact area shows two faces divided by the neutral (unstrained) fiber located in the middle of the sheet's thickness. The inner face suffers strain values under compression and the outer face under tension, Hu et al. (2002) [29]. This plastic strain operation presents a recurrent difficulty which is the springback phenomenon. This phenomenon gets complicated when accurate bending radius fabrication are required. Thus, it is necessary to predict the material elastic recovery behavior, in order to achieve the technical drawings specification. A higher bending radius is commonly used to compensate the springback phenomenon.

The hypothesis of this study is to analyze if the electroplastic effects have an influence on the bending forces and elastic recovery forces. If so, the bottom bending process is assisted by electropulses (EPs) will improve the springback manufacturing issue, and subsequently

enhance the material formability. Previous electrically assisted bending process studies have combined electroplastic thermal and athermal effects, for example Salandro et al. (2011) [30] carried out conventional sheet metal bending experiments. Jones and Mears (2010) [31] studied traction-led sheet metal bending. Green et al. (2009) [32] focused on springback elimination in previously bent metal sheets. All of these authors used pulses oscillating between 1 and 4 s and electric current densities of 10 to 90 A/mm^2 , which lead to an increase in sheet metal temperature of 100 up to 400 °C. This article studies the sheet metal bending process assisted by high density EPs and focuses just on the athermal effects of electroplasticity. To do so, an electric field is induced through different flat metallic specimens, while undergoing a bottom bending process. The bending forces are measured to determine force variation due to the induction of high EPs application. In order to focus on the athermal effects, a novel EPs generator was designed and manufactured.

2.2 Objective

The objective of this chapter is to analyze the impact of the effects of electroplasticity on the electrically assisted metal sheet bending process of 1050-H18 aluminium alloy and X5CrNi18-10 stainless steel. The studied mechanical parameters will be the bending forces and the elastic recovery forces. It will be also characterized the bottom bending phases by the plastic strain behavior throughout the process.

2.3 Methodology

2.3.1 Microcurrent pulse generator

A microcurrent pulse generator was manufactured to minimize the thermal effects in the test pieces during the electrically assisted bending process. The generator has two circuits: the main circuit and the trigger control circuit. The function of the main circuit is to induce the current intensity in the test piece through a capacitor discharge. The electric discharges are controlled by a silicon thyristor, which defines when the current pulses are transmitted through the material. Discharge time and/or pulse duration are defined by an RLC circuit configuration. A coil is needed to protect the silicon thyristor from sharp current drifts. The left hand half of Figure 1 outlines the main components of the EPs generator whilst the right hand half shows how the EPs flows through the material.

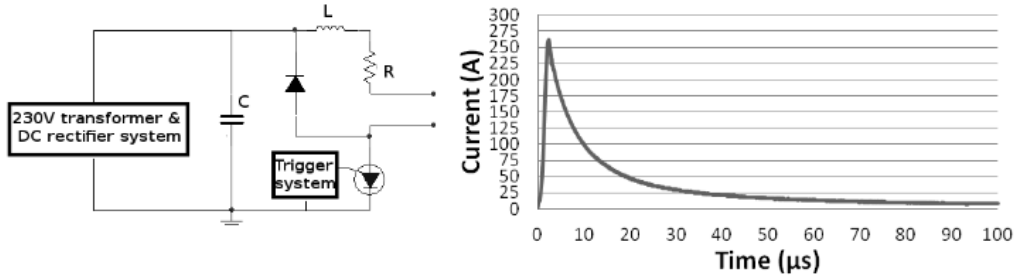


Figure 1: Electropulse generator outline.

The trigger circuit controls the frequency of induced EPs. This circuit is a relaxation oscillator made with a programmable unijunction transistor (PUT). The characteristics of EPs are: 50 μs pulse duration, 75 to 250 Hz frequency range and 300 A maximum current intensity. Xu et al. (2007) [19] used similar EPs magnitudes to evaluate the influence of electroplasticity on the electrically assisted drawing process.

2.3.2 Experimental configuration

The chemical composition of both commercial materials investigated are: 1050-H18 aluminium alloy (0.05 wt.% Cu, 0.25 wt.% Si, 0.4 wt.% Fe, 0.05 wt.% Mn, 0.07 wt.% Zn, 0.05 wt.% Ti, balance Al) and X5CrNi18-10 stainless steel (0.05 wt.% C, 1.97 wt.% Mn, 8.31 wt.% Ni, 18.38 wt.% Cr, 0.22 wt.% Mo, 0.32 wt.% Cu, 0.048 wt.% N, 0.005 wt.% S, balance Fe). Both sheet metal dimensions and induced peak current densities for each material are showed in Table 1.

Table 1: Material dimensions and transmitted peak current densities.

Material	L (mm)	W (mm)	T (mm)	Frequency (Hz)	Current density (A/mm^2)
Aluminio 1050	120	32	0.5	100	17.2
				200	15.9
	130	30/20/10		100	17.6 / 26.5 / 53
				200	17 / 25.5 / 51
X5CrNi18-10	130	25 / 19 / 14 / 9	1	100	11 / 14.6 / 19.6 / 30.5
				200	10.6 / 13.4 / 18.9 / 29.4

A nylon V-die with an angle of 90° and a 3 mm inner bending radius was used in the bottom bending process. The bending operation was performed by a Micro Test EM1/20/FR Universal Testing machine with a constant velocity of 162 mm/min. Two HBM load cells, model reference numbers S9M/500 N and S9M/2KN, were used, with a scale range of 500 N and 2 kN respectively. An infrared thermographic camera was used to measure the surface temperature variation. The effects of electroplasticity on the bottoming bending forces were regularly registered with a Spider 8 data acquisition module, operating at a sampling rate of 600 Hz. A schematic diagram and the engineering drawing of the electrically assisted bottom bending process are presented in Figure 2.

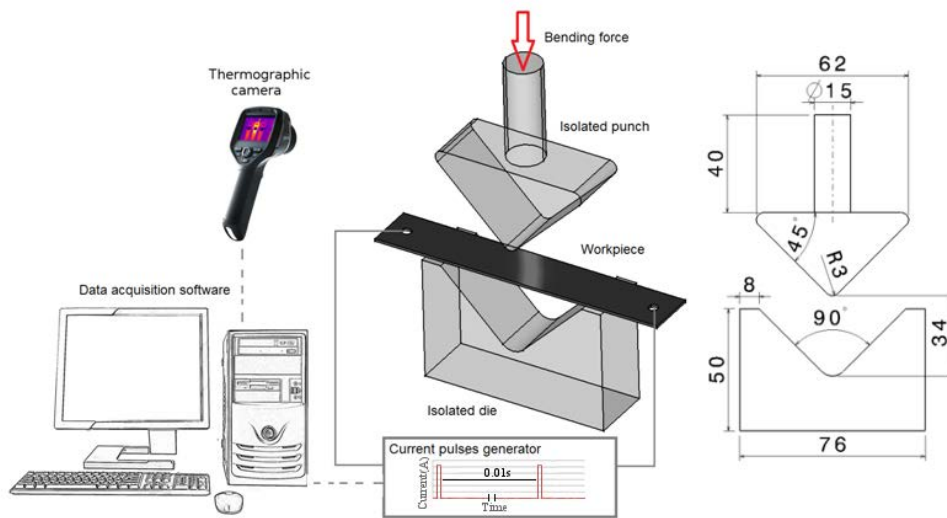


Figure 2: Bottom bending process schematic diagram and engineering drawing.

2.3.3 Thermal behavior

The temperature variation of the material was determined to assess the relevance of the Joule effect. As the bulk temperature directly depends on the electric energy consumed, the heat flux was estimated from the EPs electric signal induced during the bending process. Figure 3 shows the electric signal's current intensity and voltage applied to the stainless steel sheet metal. The consumed mean power of such a pulse is 0.29 W per second.

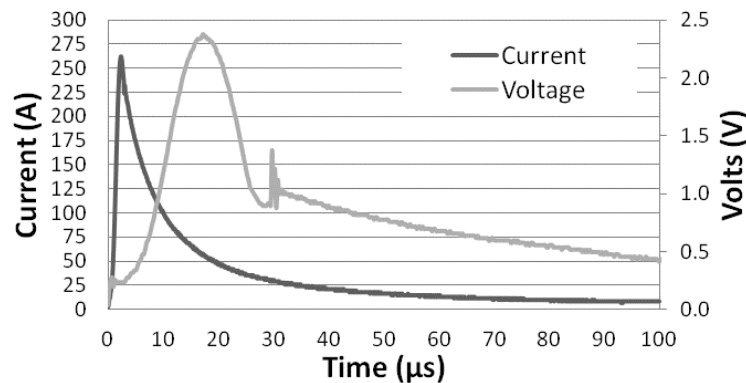


Figure 3: Electric signals of a electropulse.

The test pieces induced with an EPs did not show a significant thermal variation during the process. The theoretical temperature, estimated by using an adiabatic model, showed that the electric flux generates a thermal variation of 5.8 °C, although, the temperature variation of the tested specimen would always be smaller than the adiabatic temperature due to heat dissipation by natural conduction and convention. Furthermore, the thermographic camera used could not capture any thermal variation on the test piece, probably due to its bulk temperature variation being lower than the camera's sensitivity (± 2 °C). Therefore, it can be concluded that the Joule effect can be disregarded, mainly due to the low pulse

duration (in the order of 50 μ s) and the EPs frequency (below 250 Hz).

2.3.4 Numerical simulation

The mechanical formulation used in the present work is based on that proposed by Celentano et al. (2011) [33]. A classical plasticity model has been adopted to describe the material behavior during the bending process in which the von Mises function F is defined as:

$$F = \sqrt{3 \cdot J_2} - \bar{\sigma} \quad (2.1)$$

where J_2 is the second invariant of the deviatoric part of the stress tensor σ ($\sigma_{eq} = \sqrt{3 \cdot J_2}$ is the so-called equivalent or von Mises stress), and $\bar{\sigma}$ is the flow stress given by the linearization of the Ludwik equation:

$$\bar{\sigma} = \sigma_y + k \cdot \bar{\varepsilon} \quad (2.2)$$

where $\bar{\varepsilon}$ is the effective plastic strain, k is the parameter aimed at characterizing the isotropic strength behavior of the material and σ_y is the yield strength defining the initial material elastic bound.

The contact and friction model adopted in this work is based on the frictional-plasticity analogy that has been developed and successfully used in many applications over the last years. The main aspects of this model can be found in Celentano et al. (2011) [33]. The governing equations together with the material constitutive and contact-friction models are discretized within the framework of the finite element method according to the numerical approach detailed by Celentano et al. (2004) [34]. The mechanical parameters of the 1050 aluminium alloy used in the numerical simulation are summarised in Table 2. Since the values of initial yield strength and ultimate tensile strength approximately fit a linear interpolation within the tensile strain interval of this material (which exhibits a relatively low ductility with a tensile rupture elongation of 6% to 8%), a linear hardening law has been adopted for simplicity purposes. The sheet was two-dimensionally discretized with 428 four-noded isoparametric plane stress elements that consider a B-bar interpolation to avoid the numerical locking due to plastic incompressibility. Moreover, a friction coefficient of 0.10 was used in the punch-sheet and die-sheet interfaces described via a mesh composed of 420 two-noded isoparametric elements. Finally, the sheet deformation was achieved by incrementally imposing (in 1000 steps) a prescribed vertical displacement of 27 mm on the punch.

Table 2: Mechanical parameters of 1050 aluminium alloy.

Young's modulus E [GPa]	69
Poisson's ratio ν	0.33
Initial yield strength σ_y [MPa]	125
Strength coefficient K [MPa]	100

2.4 Results and discussion

The bottom bending process was firstly characterized via experiments and simulation, without considering the effects of electroplasticity. Figure 4 shows computed and experimental (averaged values measured from 5 strips) results for the bending force corresponding to a 0.5 mm thick 1050 aluminium sheet metal. Moreover, a numerical prediction of the effective plastic strain at the location where the sheet experiences the maximum stretching (node P) is also plotted. The abscissa in Figure 4 is a dimensionless time ($t^* = t / 12.5$ s), since 12.5 s is the last instant of phase C. The maximum force applied during the bending process is achieved when the time is $t^* = 1$. The bottom bending process is performed allowing for clearance to avoid contact between the upper and lower parts of the die. The above mentioned clearance is twice the thickness of the bent test piece.

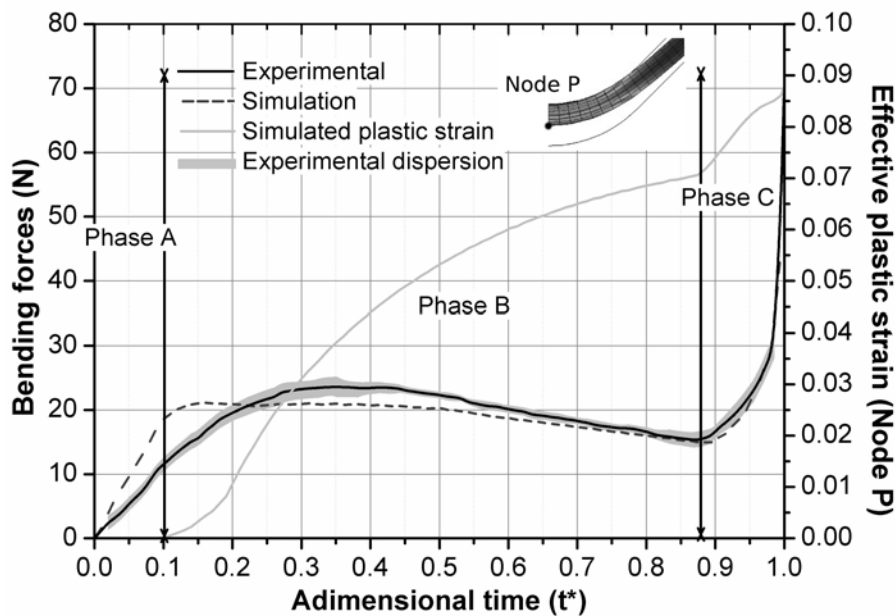


Figure 4: Bottom bending process characterization at node P.

The grey curve reports the effective plastic strain in the bending process. Before the dimensionless time of 0.1, node P does not exhibit any plastic strain (phase A). From 0.1 onwards, significant strain becomes evident at node P, as well as a von Mises stress of 143 MPa, slightly higher than aluminium's yield strength (phase B). These two indicators represent the start of plastic strain on the sheet metal (phase B), although the effective plastic strain is just localized on the surface. From the adimensional time of 0.4 onwards, the bending force starts decreasing. This force drop is likely due to a sliding contact between sheet metal and die. During this phase, the von Mises stress remains substantially constant at node P. The small stress variation, attributed to the hardening of aluminium, is in the order of 16 MPa. From a dimensionless time of 0.88 onwards, the bending force increases drastically and the upper and lower parts of the die draw close (phase C). Although there is no contact in the vicinity of node P, contact occurs in other areas of the sheet metal. It is at this time when the sheet metal is in closer contact with the die and the curvature radius of the latter is impressed on

the sheet metal. This phenomenon is also registered in the slope change that occurs on the strain curve, leading to the greatest strain found.

In summary, the bending process characterization is defined by four phases. Phase A is characterized by metal-die coupling without noticeable strain. Phase B is marked by metal-die slippery contact and plastic strain initiation. Phase C is characterized by a large plastic strain. Finally, phase D is defined by stress relaxation behavior. The finite element simulation enabled to determine properly the material's mechanical behavior during the bending process. Since the computed load values reasonably fit the corresponding experimental measurements during the whole evolution of the bending process, it is assumed in this work that the computed von Mises stress and effective plastic strain contours and evolutions shown below constitute realistic and representative measures of the material's response.

Figure 5 shows effective plastic strain contours for phases B and C, at two dimensionless times (0.3 and 1, respectively). Due to the symmetry of the test piece, only half of it was considered for optimizing computational time. Performed simulations show that the neutral (unstrained) fiber is located in the middle of the sheet's thickness. In contrast, the sheet edges present the maximum strain values, where, as expected, its inner face is under compression and its outer face is under tension.

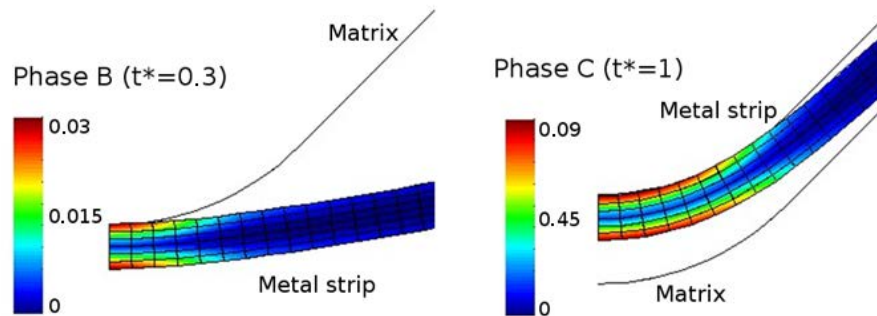


Figure 5: Computed effective plastic strain during the bottom bending process.

Initially, the contact surface between the upper part of the die and the test piece is small. However, in the final bending stages the contact section increases. It is at the final stage when the greatest strain occurs due to the die impressing its shape on the sheet metal which leads to the material adopting the V-shape of the die. Figure 6 shows how the von Mises stress at node P evolves during a bending cycle. As already mentioned, the material response during phase A is elastic while in phases B and C plastic strains clearly take place.

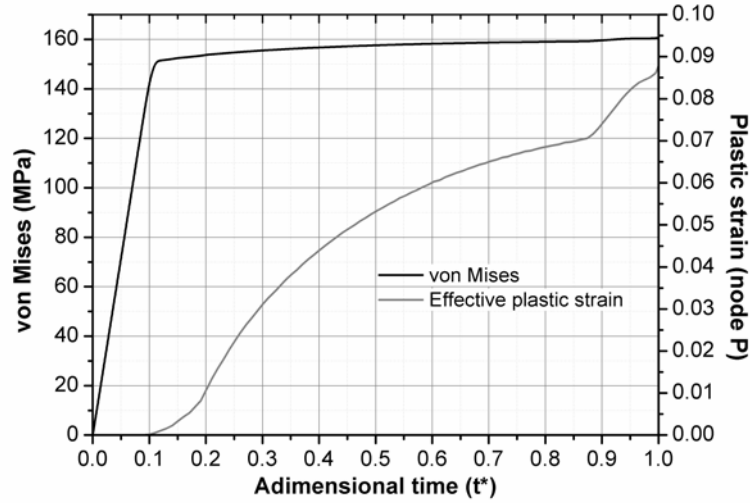


Figure 6: Von Mises stresses evolution during the bottom bending process.

2.4.1 Electroplastic effects

Two variables of interest are recorded: the average bending force in phase C and the elastic restoring force of the sheet metal occurring in phase D, after the maximum force peak. The forces obtained in a bending process assisted by high density current pulses are compared with those resulting from a conventional bending process performed without current pulses. These two variables are selected because the forces associated with great plastic strain are, in general, very sensitive to high density current pulses. Tang et al. (2000) [27] proved that drawing forces decrease when a 300 Hz current pulse is assisting the process. Therefore, the focus is on phase C, where both the largest stresses and the highest material strain rates occur. It is expected that those deformations have an impact on phase D, where elastic recovery is recorded. Previous authors, such as Salandro et al. (2011) [30], have already reported a bending force and a springback reduction on stainless steel when the bending process was electrically assisted. However, it is important to note that, in contrast to the present work, the Joule effect was significant on Salandro's study.

Bending forces

The average bending force in phase C is represented as a relative force. This is the average force within the dimensionless time interval [0.88-1.0 s] for a EPs assisted process and it is expressed as a fraction of the average force in a conventional bending process (i.e., that without electroplastic effects). Figure 7 shows the relative force (the error bars correspond to a 95% confidence interval), determined by current density and pulse frequency, for pulses of 50 μ s.

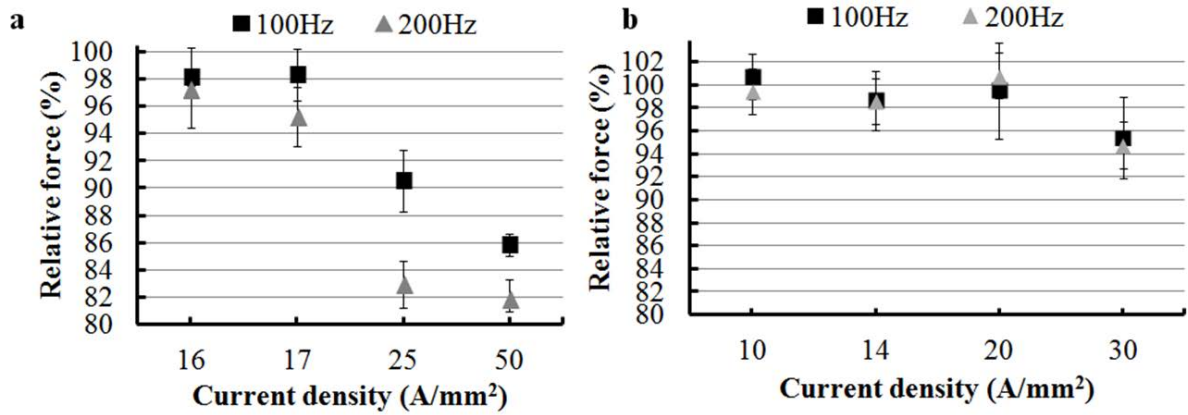


Figure 7: Aluminium (a) and stainless steel (b) relative bending forces for the different electrically assisted configurations.

When the process is assisted by high density current pulses, the results of the average force required to bend aluminium decrease. However, the results for stainless steel reveal that further studies with higher densities need to be carried out to confirm the same decreasing trend. This is due to the fact that an apparent force drop is only observed after applying the maximum density considered in this study. The effect produced by the current pulses varies from one material to another. A current density of $25 A/mm^2$ reduces by 14% the necessary force to bend aluminium. Instead, a current density of $30 A/mm^2$ only decreases by 4% the force required to bend a stainless steel sheet metal.

Overall, the bending strength is inversely proportional to the current density (i.e., if the current density increases, the force required for bending the sheet decreases). The pulse frequency behaves in a similar way (i.e., when the frequency increases, the bending force decreases). For example, for 1050-H18 aluminium, the reduction in bending force can be as high as 18% when assisted by pulses of $50 \mu s$, 200 Hz and $50 A/m^2$. Whilst for X5CrNi18-10 steel with a current density of $30 A/mm^2$ force reduction is only 6%. The aluminium bending force is more sensitive to pulse frequency than to current density. On the other hand, the relative contribution to steel of current density and frequency performs as follows: an increase in current density from 10 to $30 A/mm^2$ produces an average decrease of about 5%; whereas a frequency increase of 100 to 200 Hz with the same current density results in a relative force decrease of 0.7%. Those values are found within the error band interval, so there is no significant difference between the responses corresponding to both frequencies. Figure 7a, which plots the relative contribution of current density and frequency for aluminium, shows that an increase in current density from 25 to $50 A/mm^2$ produces an average relative force decrease of 3.5% and, in contrast, a frequency increase of 100 Hz to 200 Hz with the same current density leads to a relative force decrease of 6%.

The difference in the behavior of materials could be explained either by the different cold work - and the associated density of dislocations - accumulated in both materials, or by the possibility of twinning in steel (due to its low stacking fault energy), as it was deeply studied

by Hull and Bacon (2001) [35]. Additionally, as the electropulsing enhance the dislocation movement through the material lattice, there will appear higher stress – strain fields when impurities or material defects are reached that will promote new dislocation generation as it was stated by Roylance (2001) [36].

Elastic restoring force

The material's yield strength in the bottom bending process, phase D, is estimated from the elastic restoring force. This force is recorded once the universal tensile and compression testing machine used for bending the sheet metal stops working. The elastic restoring force starts off with the damped oscillation associated to the machine coming to a halt. The damping takes less than 1 s and is followed by a relaxation behavior which converges to a constant limit force.

Figure 8a shows the experimental elastic restoring force behavior associated to the bending process of a 1 mm thick stainless steel (phase D). Figures 8b and 8c show the relative experimental restoring force registered in the assisted process ($50 A/mm^2$ in aluminium and $30 A/mm^2$ in steel) as compared to the conventional process. A relative force of 1 means that the restoring force obtained in the assisted process is equal to the restoring force in a conventional bending process. It also shows that the elastic restoring force transient period is approximately 18 s. To study the variation of this force, the time interval between damping completion and transient disappearance is considered. The variation experimented by the force during this time interval is the result of the interaction of two coupled behaviors. This is due to the reaction of the polymeric base (bending die) and the remaining elastic force as a product of the bending process. For this reason, the comparison between forces is performed in a relative way: assisted processes with frequencies of 100 and 200 Hz are compared in relation to a conventional bending process.

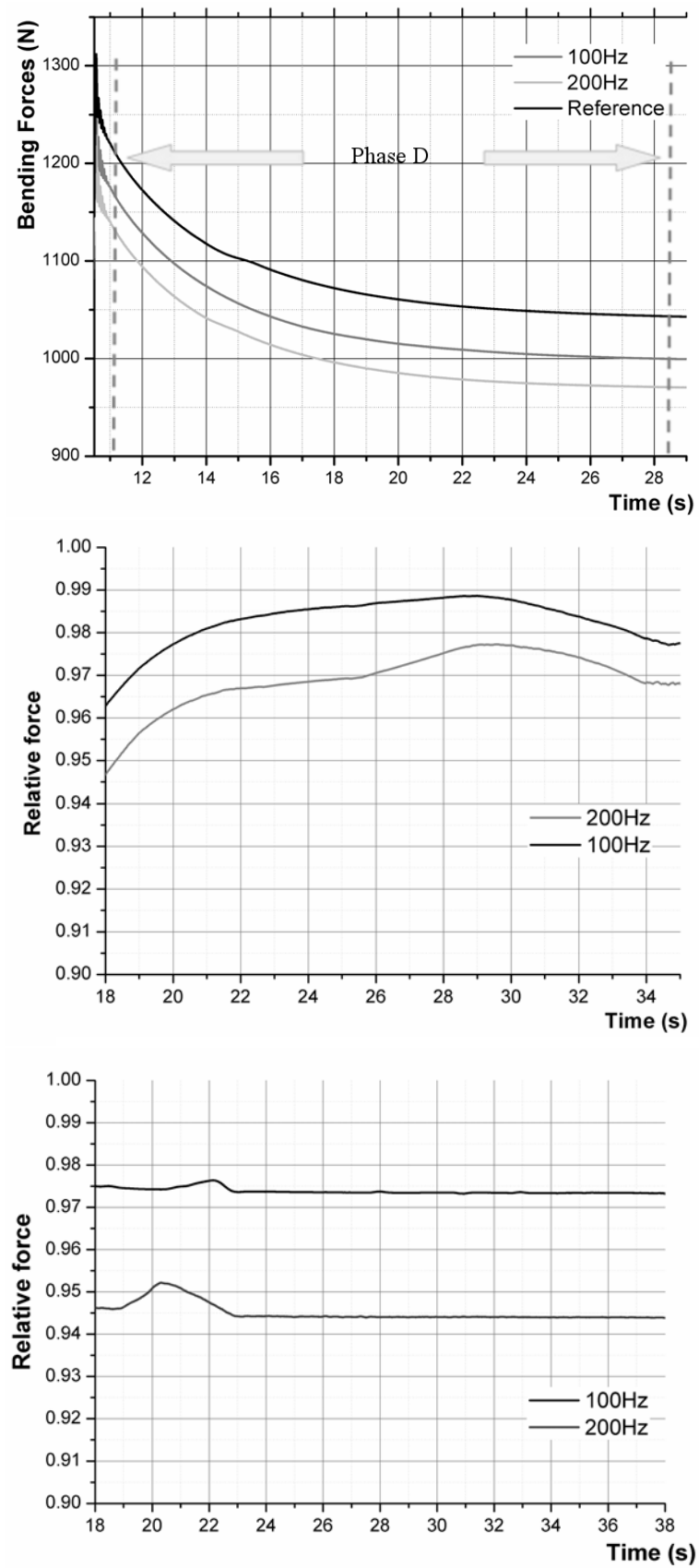


Figure 8: Bending process phase D (a), aluminium (b) and stainless steel (c) relative elastic bending forces at phase D.

Figures 8b and 8c show the experimental relative elastic force for a current density of $50 A/mm^2$ in aluminium and $30 A/mm^2$ in stainless steel. In both figures, it can be seen that the higher the frequency, the lower the elastic restoring force and, consequently, the lower the yield strength. Moreover, the elastic restoring force is smaller in assisted bending processes than in conventional ones.

Figures 9a and 9b summarize the variations in elastic restoring force for aluminium and stainless steel under different current densities and pulse frequencies.

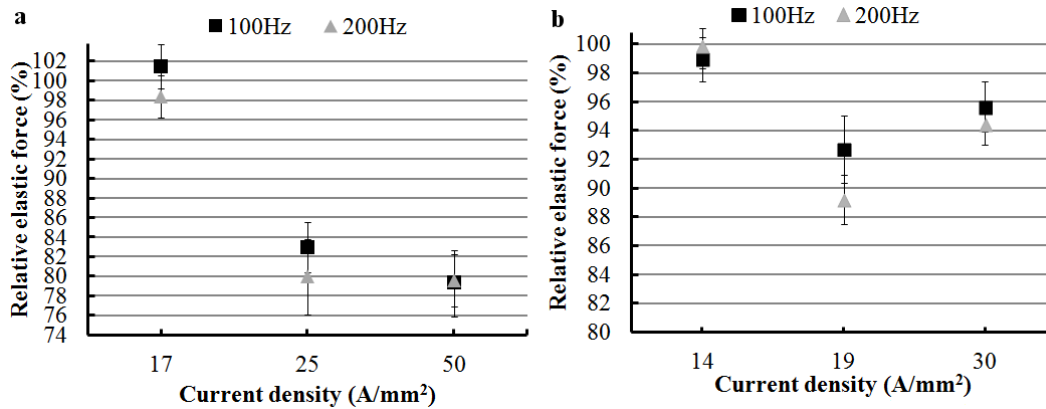


Figure 9: Aluminium (a) and stainless steel (b) relative elastic bending forces for the different electrically assisted configurations.

It is shown that only the 1050 aluminium elastic restoring force is significantly reduced, about 20% on average, when current density is around and above $25 A/mm^2$. On the other hand, the stainless steel shows an average of 7% on the relative elastic forces reduction when current density is around and above $20 A/mm^2$. However, for stainless steel, the error bars indicate that the force reduction could be 2.5% in the worst case. Perkins et al. (2007) [37] proved that the effect of electroplasticity varies depending on the material. Each material has a current density threshold to initiate improvements in workability, and minor current density changes could reveal significant altered results. Despite the average the steel relative force values increase around 4% for $30 A/mm^2$ compared with $19 A/mm^2$ tested workpiece, the relative force error bars show that the difference between those values could be smaller than 2%. So, it is believed that the induced electric flow's effect for these two current densities do not lead any improvement difference in the mechanical formability on the bottom bending process. The results dispersion could be explained by small radial and length material properties differences, variability in electrical resistance due to internal lattice defects or impurities and fixture effects like friction. Although these factors could induce small differences, the result clearly exhibit the mechanical behavior change when the process is electrically assisted.

The frequencies used do not show any influence on the elastic behavior attenuation, because the 100 Hz and 200 Hz values are present within the errors values. Although Salandro et al. (2011) [30] reported a springback reduction of up to 77%, it should be noted that their experiments included the influence of the Joule effect, where reported temperature values

were about 115 to 335 °C. On the other hand, in the present analysis a maximum reduction of 21% is reported but considering a negligible Joule effect, which means that the decrease is only attributable to the athermal electroplasticity phenomenon. Finally, although the elastic restoring forces decrease with current densities over 20 A/mm^2 , future studies need to be carried out to study the threshold where the current density / pulse duration combinations begin to show improvements in formability.

2.5 Conclusions

The mechanical influence of athermal electroplastic effects on the bottom bending process has been addressed. The induced electric pulses do not increase the bulk temperature of the workpiece to any notable amount. A numerical simulation has allowed for the characterization of the different phases defining the bending stages. High current density pulses do not have the same impact on aluminium than on stainless steel. Current density and frequency have a noticeably influence on the bending forces and the springback effect on 1050 aluminium, while stainless steel needs further study with higher current densities. The material's elastic restoring behavior was lower when the bending process was electrically assisted, especially for densities over 25 A/mm^2 . Finally, the frequencies used, 100 and 200 Hz, did not show a significant difference between them on the bending and restoring force results.

The athermal effect has been proved to be effective to reduce the bending force and the elastic restoring force during the bottom bending process. Still this technique presents modest results compared with the technique that combines thermal and athermal effects. Finally, the bending process electrically assisted with short current pulses is a feasible technique that does not require sophisticated equipment. Besides, the power consumed by this novel technique is significantly smaller than that of continuous current assisted techniques.

Chapter 3

Round turning process assisted by electropulsing

After having proved the electroplastic influence on material formability during a bottom bending process, in this chapter is reported on a novel machining process technique: *in situ* electrically assisted turning process based also on the electropulsing influence. A brand new specific generator is made capable of modifying the pulse duration and the frequencies discharge. The influence of different electropulsing configurations assisting the round turning process is studied, specifically on the surface properties and the power consumption in several steel alloys. The results show that the electrically assisted turning process improves material machinability by decreasing the power consumption up to 105.4 W and the specific cutting energy up to 25%. The assisted process also modifies the surface properties, the average surface roughness decreases within the range of 6 to 40% and material hardness decreases within the range of 6 to 16% when compared to the conventional process.

3.1 Introduction

Currently the prevailing trend is the development of hybrid production processes. Many of these consist of assisting conventional turning processes with non-conventional processes. On the one hand this allows for the product properties to be improved. On the other hand, it broadens the field of application for the conventional production process. Different researchers have performed important advances in the creation of hybrid processes with the goal of resolving the limitations of many conventional processes, especially when very hard materials must be mechanized. Some examples include the improvement of the silicon carbide (SiC) milling process when is assisted with electric charges studied by Renjie et al. (2011) [38]; the improvements of surface roughness when the modification process is assisted by an electro-chemical finish as reported by Pa (2008) [39]; the electro-chemically assisted burnishing process also shows improvements in surface roughness as presented by Newman (2000) [40], and finally, a machining enhancement when AZ91 alloy was previously assisted with current pulses during a rolling process, studied by Zhang et al. (2012) [41]. They concretely reported how the product machinability improved by decreasing the cutting forces and the surface roughness. Following this last line of research, the present study intends to

go one step further, studying the effect that *in situ* electropulses (EPs) have on the turning process.

In the fabrication of metallic materials by chip removal, some of the most important parameters to take in consideration are: the surface roughness, the material hardness and the machining power. Adequately choosing cutting conditions is a recurring problem with the goal of guaranteeing adequate surface roughness, knowing that these machining conditions are limited by the material strength and the power available for machining. In the turning process, surface roughness is principally related to the following parameters: the feed rate, the cutting depth, the material hardness and the cutting tool's radius, stated by Hocheng and Hsieh (2004) [42].

Surface roughness during the machining process is defined by the material elastoplastic behavior. During the turning process, prior to starting the chip removal and due to the elevated primary shear stress values, plastic strain is initiated in the material which is in contact with the principal face of the cutting tool. These stresses generate a plastic movement of the material called plastic side flow, which tend to create pile up on the secondary face of the cutting tool. This phenomenon generates greater peaks and valleys in roughness as described by Liu and Melkote (2006) [43]. The *in situ* high current density electropulsing assisted turning process is a novel technique that could solve this problem.

Electroplasticity has demonstrated that it reduces the stress necessary to create plastic strain in a material. Stolyarov (2009) [26] proved that the ultimate tensile strength decrease and Tang et al. (2000) [27] reported an increase in material elongation. Furthermore, it has been shown by Salandro et al. (2011) [30] that it attenuates the elastic recovery of the material. A previous study, Sánchez et al. (2014) [44], have proved that the formability of the material improves after plastic deformation. The electropulsing assisted turning process intends to improve surface roughness compared to the conventional process primarily due to two reasons. First, electroplasticity could influence the major shear stresses needed to start the chip removal, those stresses were studied by Khidhir and Mohamed (2010) [45]. The decrease in the shear stress is accompanied by a lower plastic side flow effect, which will induce less pile up on the secondary face of the material and therefore a lower average roughness (Ra). Secondly, electroplasticity affects the elastic recovery of the material by attenuating this feature, as it was proved by Green at al. (2009) [32]. These authors affirm that the elastic recovery behavior is reduced when thermal and athermal effects affect the material mechanical properties and / or the metallographic structure. That elastic behavior variation is another factor which can improve surface roughness in the machining process.

3.2 Objectives

This thesis section study the turning process when assisted by high current density electropulsing, paying special attention to the athermal effects of electroplasticity. A new micropulse current generator was designed and created with the goal of minimizing the Joule effect. The current pulses are induced in different metallic workpieces, while a turning pro-

cess of roughing and finishing is performed. The impact of the EPs is analyzed on the power consumed, the surface roughness and the material hardness of different steels. The goal is to study which differences are presented between the conventional turning process when compared with the electropulsing assisted turning process on term of power consumption and surface properties.

3.3 Methodology

3.3.1 Experimental configuration

The commercial materials that were used in the current study are listed in Table 3. The metallic cylindrical bars dimensions were 190 mm in length and 25 mm in diameter. A polymeric ring and platform was used to electrically isolate the workpiece from the lathe and to electrically isolate the carbon clamps from the dead centre of the lathe, respectively. The tool holder was also isolated all around with the same polymeric material.

Table 3: Materials chemical composition.

	% C	% Mn	% Si	% P	% S	% Cr	% Cu
SAE 1020	0.2	0.53	0.23	0.01	0.008	0.06	0.01
SAE 1045	0.45	0.7	0.25	0.008	0.007	0.07	0.01
SAE 4140	0.42	0.85	0.23	0.02	0.02	1.01	0.13

Turning test was performed on a TOZ, ZPS-R5 lathe. A tungsten carbide TNMG-16 tool with 0.8 mm nose radius and a cutting edge angle of 0° and a MTJNR 2525 M16 tool holder were used to turn the metallic bars. The machining parameters used and initial material hardness are shown in Table 4.

Table 4: Turning operation parameters.

Spindle speed (rpm)	Feed rate (mm/rev)	Depth cut (mm)	Hardness (HRB)
			88
460	0.046; 0.127; 0.254; 0.356	0.25	100
			105

The power consumed was continuously registered with a Fluke 434 energy analyser. The sampling rate was 200 KS/s with storage every 0.5 s. The surface roughness was measured with a rugosimeter (Mitutoyo SJ-201). Rockwell B hardness variations on the workpieces were also measured with a durometer (Wolpert Wilson 600-MRD).

A self-made short current pulses generator is manufactured to discharge multiple positive pulses. During the electropulsing, the surface temperature variation was measured for each test with a thermocamera (Wuhan Guide *TP8S*). The parameters of the current such as frequency, density and pulse duration were monitored by an oscilloscope. The EPs parameters used and the material maximum temperature measured are listed in Table 5.

Table 5: Electropulsing operation parameters and maximum bulk temperature.

Current intensity (A)	Pulse duration (μs)	Frequency (Hz)	Max. Temp. ($^{\circ}\text{C}$)
			92.0
90	50 / 200	100 / 300	138.5
			190.6

A schematic illustration of the electrically assisted turning process is presented in Figure 10.

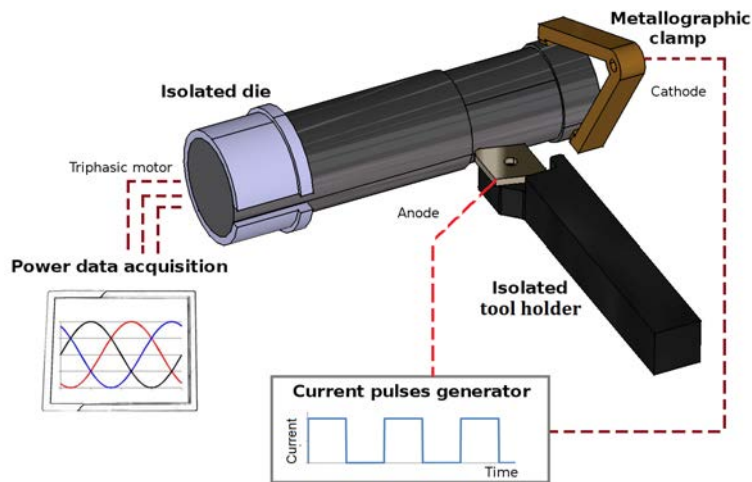


Figure 10: Electrically assisted turning process schema.

In order to electrically assist the turning process *in situ* several round conventional turning operations were previously done on each workpiece. This procedure ensures the workpiece concentricity and the optimal electric contact of the cutting tool and the carbon clamps during the turning process. Later, a round turning operation without electric pulses (conventional process) of 45 mm length was done. Subsequently, a round turning operation was performed assisted with EPs (assisted process). Therefore, the power consumption, surface roughness and material hardness of both processes have been compared.

3.3.2 Microcurrent pulse generator

Similar to previous study Sánchez et al. (2014) [44], a specific microcurrent pulse generator was designed and manufactured to minimize the thermal effects in the workpieces during the electrically assisted turning process. The generator has two circuits: the main circuit and

the trigger control circuit. The function of the main circuit is to induce the current intensity in the workpiece. The electrical discharges are controlled by powers MOSFET, which define when the EPs are transmitted through the material. A coil is needed to protect the transistors from sharp current drifts. The trigger system use astable and monostable oscillator circuits to control the frequency and the pulse duration of the induced EPs. The EPs characteristics are: 50 to 200 μs pulse duration, 100 to 400 Hz frequency range and a maximum current intensity of 90 A. The left hand half of Figure 11 outlines the main schema of the microcurrent pulse generator, while the right hand half exhibits the EP profile.

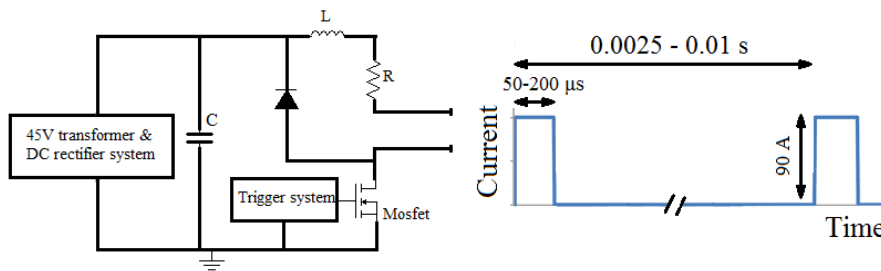


Figure 11: Microcurrent pulse generator schema and EP profile.

3.4 Results and discussion

3.4.1 Thermal behavior

The bulk temperature is measured in the cutting zone with a thermographic camera determining the thermal variation. The recorded bulk temperatures in the trials with pulses of 200 μs duration and discharge frequency of 300 Hz presented variations in the order of 10 $^{\circ}\text{C}$ above the registered temperature in the trial without pulses. The maximum temperature values registered for the different steel grades during the electropulsing assisted processes are shown in Figure 12. This figure is obtained for the condition with 0.356 mm/rev feed rate, 460 rpm spindle speed, 0.25 mm depth of cut, 200 μs pulses duration and 300 Hz pulse frequency. The maximum temperature value is an instantaneous measure which is registered in the cutting zone, at the intersection of the tool and stock.

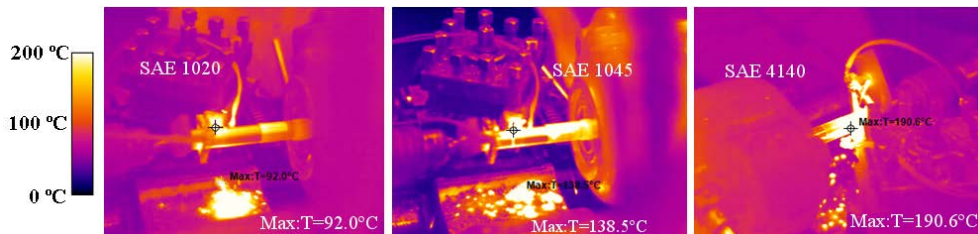


Figure 12: Maximum registered thermal values.

The average power generated by the EPs with 300 Hz frequencies and 200 μs duration is 48.6 W. As this is done with a duration in μs , the thermal contribution of the electric

field in the process can be considered to have little relevance, due to the heat dissipation by convection and conduction. However, in an atomic-level the EPs generate hotspots due to the change of the resistivity in the metallographic defects, like grain boundaries, dislocations, inclusion and so on, as it was stated by Conrad and Sprecher (1989) [9]. Then, those hotspots could be one of the reasons for the mechanical material modification.

3.4.2 Surface roughness

The average roughness Ra results obtained are shown in Figure 13. In Figure 13a, 13c and 13e, the experiments performed with EPs of 200 μ s pulses are shown. In Figure 13b, 13d and 13f, the experiments performed with EPs of 50 μ s duration are shown. The average roughness measured in 1020 carbon steel is shown in Figure 13a and 13b, 1045 carbon steel is shown in Figure 13c and 13d and 4140 steel is shown in Figure 13e and 13f. In these figures, the machining process without EPs is compared with the EPs assisted process. The experimental values of the average roughness are the result of 5 measurements performed in different parts of the workpiece. Each point of the graphic represents the average of these values. The error bars define the confidence interval with a 95% probability. The continuous line represents the calculated theoretic roughness with the equation $Ra_{th} = 31.25 \cdot (f^2/r_h)$ commonly used to estimate the average roughness Ra (μ m), Rabinowice (1965) [46], where f represents the feed rate (mm/rev) and r_h the cutting tool nose radius (mm).

The specimens assisted by EPs and 0.046 mm/rev feed rate show a better surface finished than those machined conventionally. The average registered decrease in Ra was 40%, 22% and 18% in 1020 carbon steel, 1045 carbon steel and 4140 carbon steel, respectively. When the harder material (4140 carbon steel) is machined an increase in surface roughness is registered at lower feed rates. Related to that, Shaw (1984) [47] has studied that the plastic side flow is greater when working in minimal shaving rate. This explains the increase in roughness that 4140 carbon steel experiences when it is machined with a 0.046 mm/rev feed rate. Even for this limited situation the effect of the pulses significantly reduces the value of Ra.

The roughness registered in the machined specimens with intermediate feeds (0.127 and 0.254 mm/rev) also improves when the process is assisted with EPs. But the difference found compared to the conventional process is not as large as in the lower feed rates. For 0.127 mm/rev feed rates, the decrease in average roughness Ra presented was 33%, 12% and 24% in 1020 carbon steel, 1045 carbon steel and 4140 carbon steel, respectively. While for 0.254 mm/rev feeds the decrease in average roughness presented was 8%, 7% and 17% in 1020 carbon steel, 1045 carbon steel and 4140 carbon steel, respectively.

Lastly, if it is analyzed the roughness registered in machined specimens with high feed rates (0.356 mm/rev) the roughness generally presents modest improvements when the process is assisted with EPs. The difference found with regards to the conventional process is not significant, the Ra values of the different populations are generally found within the error bars. Even so, the decreases registered of the population means for Ra were 6%, 10% and 12% in 1020 carbon steel, 1045 carbon steel and 4140 carbon steel, respectively.

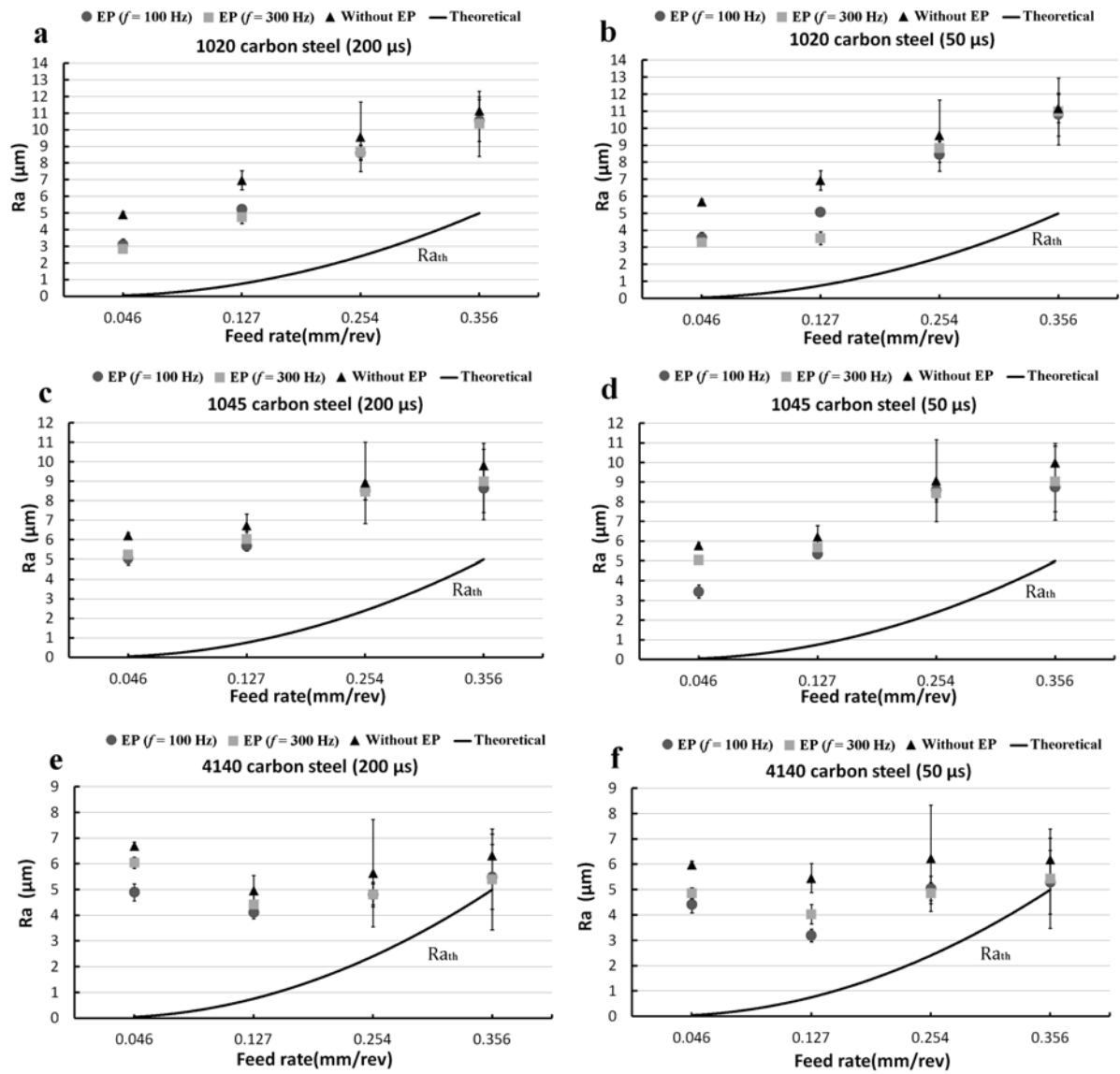


Figure 13: Roughness values for SAE 1020 (a-b), SAE 1045 (c-d) and SAE 4140 (e-f).

When the results obtained are compared according to the influence of the frequency and the duration of EPs on the roughness, the range of values used do not present statistically significant differences. As such, the different electric configurations used do not ensure that a greater frequency or duration improves the surface roughness, at least in the frequency ranges between 100 – 300 Hz and pulse duration between 50 - 200 μs . Even so, the assisted process always presents surface roughness results lower than the conventional process. However, a surface roughness variation using different EPs configurations was expected due to thermal expansion inertia, in an atomic – level, being faster than when lower frequencies and pulse duration are induced. That thermal expansion is expected to affect the material elastoplastic behavior reported by Liu and Melkote (2006) [43]. Although the experimental results confirm that the electrical configurations used are statistically significant for lower and intermediate feed rates, 0.046 and 0.127 mm/rev. For higher feed rates, 0.254 and 0.356 mm/rev, no evidence of improving the surface roughness was found.

Furthermore, the difference existing between the experimental values and the theoretical roughness curve can be due to the influence of the cutting speed as reported by Muñoz-Escalona and Cassier (1998) [48], vibrations studied by Wang et al. (2013), built up tool edge stated by Gokkaya (2010) [49] and tool wear reported by Khidhir and Mohamed (2010) [45]. Furthermore, the material type and hardness also influence the final roughness. Sata and Shaw (1964) [50] analyzed that those features are able to increase up to 6 μm in steel alloys, matching precisely with the difference obtained in this study.

Zhang et al. (2012) [41] reported that the average roughness decreased approximately between 20% and 30% when the process is previously assisted with current pulses. The electric parameters used were: current density between 274 and 347 A/mm^2 , frequency between 151 and 294 Hz and with a pulse duration of 70 μs . These results are similar to those obtained in the present study. It can be concluded that previous pulses as well as the *in situ* pulses improve the surface roughness of the machined material.

3.4.3 Material hardness

The surface hardness of the machined specimens were studied in both processes: the assisted process and the conventional one. Figure 14 shows the relative hardness of 1020, 1045 and 4140 carbon steel assisted with EPs of 100 Hz and pulse duration of 200 μs (Fig. 14a) and 50 μs (Fig. 14b), and the relative material hardness of same steel alloys when assisted with EPs of 300 Hz and pulse duration of 200 μs (Fig. 14c) and 50 μs (Fig. 14d).

The relative hardness is the quotient between the hardness of the machined material with EPs with respect to the hardness of the material machined in a conventional manner (HRB_e / HRB). The results observed are the product of 5 hardness measurements per registered workpiece across its length and applying the corresponding correction factor of cylindrical geometry indicated by ISO standard 6508-1: 2007.

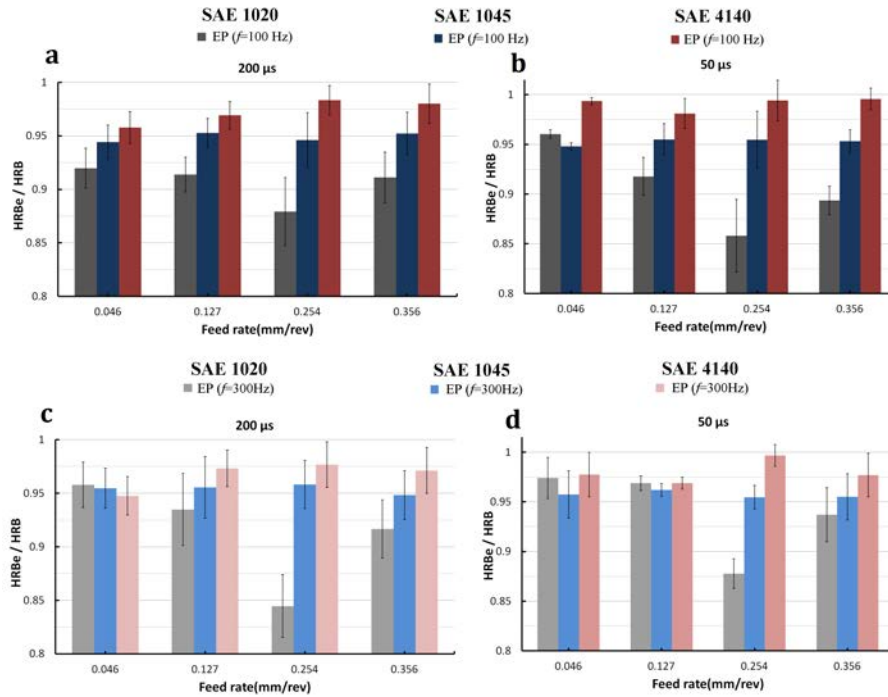


Figure 14: Relative material hardness.

Generally the electropulsing assisted machining process reduces the material hardness compared to the conventional mechanized process. The maximum reductions of relative hardness are: 16% for the 1020 carbon steel, 8% for the 1045 carbon steel and 6% for the 4140 carbon steel. The workpieces induced with 200 μs EPs, Fig. 14a and Fig. 14c, are those that show the greatest decrease in surface hardness, although the magnitude of the decrease depends on the material's type. For the hardest materials, 4140 carbon steel, the differences found in hardness for both processes is less significant than in the least hard material, 1020 carbon steel. Last material presents a greater decrease in material hardness when machined with a 0.254 mm/rev feed rate and a 300 Hz is induced, with a 200 μs pulse duration. Then, the greatest decrease in hardness in 1045 and 4140 carbon steel is observed for 100 and 300 Hz frequencies, respectively, with 0.046 mm/rev feed rates and 200 μs pulse durations. Assisted machining processes with 50 μs pulses and feed rates between 0.254 and 0.356 mm/rev also presented a decrease in relative material hardness.

In general the results show that the relative hardness for the different electric parameters used are within the error bars, therefore it can be concluded that there is no significant difference between the two populations. That is, no difference is observed between the averages of the populations induced with 100 and 300 Hz, hence, the frequency does not seem to influence final hardness. The greatest decrease in the hardness results is observed when EPs with 200 μs duration is applied when compared to those induced with 50 μs duration.

The decrease in surface hardness in the material affected by pulses is principally due to the electric flow passing through the material. In the previous results the electric flow is observed to affect the materials in different ways. The differences can be explained as, first,

the impact of this phenomenon depends on the previous state of material hardness detailed explained by Boothroyd (1989) [51], as the EPs release residual tensions and decrease the flow yield strength. Then, Conrad (2001) [5] described that the high density EPs promote material dislocation movements towards the interstitial space. This is accompanied by a decrease in the surface hardness of the material as was shown in the study by Zhang et al. (2012) [41]. These authors observe that the maximum decrease in hardness is approximately 20%, when the process had been previously assisted by EPs with 70 μs duration, 300 A/mm^2 average density and a 294 Hz frequency. The present study shows a maximum reduction of surface hardness of 11% when the process is assisted *in situ* with an electrical intensity of 90 A, a frequency of 300 Hz and 200 μs pulse duration. It must be highlighted that in both cases the EPs influenced the material structure improving its machinability.

3.4.4 Power consumption

The electric energy consumption by the engine is proportional to the cutting force necessary to initiate the chip removal. The specific cutting energy is the energy consumed per unit of volume of the material removed. In general, Pawade et al. (2009) [52] defined that the specific cutting energy is a parameter related directly to the chip formation, the cutting force and the tool wear. The specific cutting energy is known as the sum of the energy consumed in the primary, secondary and tertiary zones of deformation stated by Boothroyd (1989) [51].

The power consumed during the cutting process was measured by the energy quality analyser (Fluke 434). The net active power W_n is determined by subtracting the starting basal power from the average power when the cutting tool is removing material. In this section, the net active power obtained is compared in a conventional turning process with respect to the power obtained in an assisted turning process. The hypothesis in question is: the net active power consumed by the motor in an assisted turning process is less than the power consumed by the conventional process.

The energy consumed by the lathe during the 1045 carbon steel cutting process is shown in Figure 15. The cutting conditions for this experiment are: 0.127 mm/rev feed rate, 1 mm depth of cut, 300 Hz pulse frequency and 200 μs pulse duration.

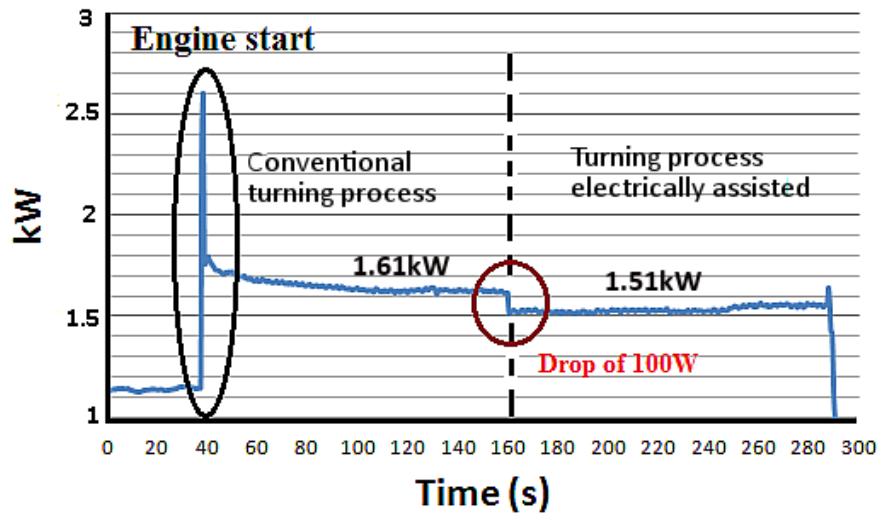


Figure 15: Active power consumption profile for the conventional and assisted turning process.

The initial power peak represents the engine start, followed by the active power consumed in a conventional round turning process, in particular a rough machining operation. At 160 seconds, a decrease of approximately 100 W in the power consumed was registered due to the application of EPs. The motor power basal consumption without machining is 1,509 W.

In Figure 16 the reduction in power consumed is shown, defined as the difference between the net active power of conventional turning and the net active power of a EPs assisted turning process ($W_n - W_{ne}$). Figure 16a shows the experiments performed with 200 μ s pulses for SAE 1045 and 4140 steel and 100 and 300 Hz frequencies. Figure 16b shows the experiments performed with 50 μ s pulses for the same steels and frequencies mentioned above. The power values shown in each case are the average of 3 values registered during the round turning operation. The error bars define the standard deviation of these values.

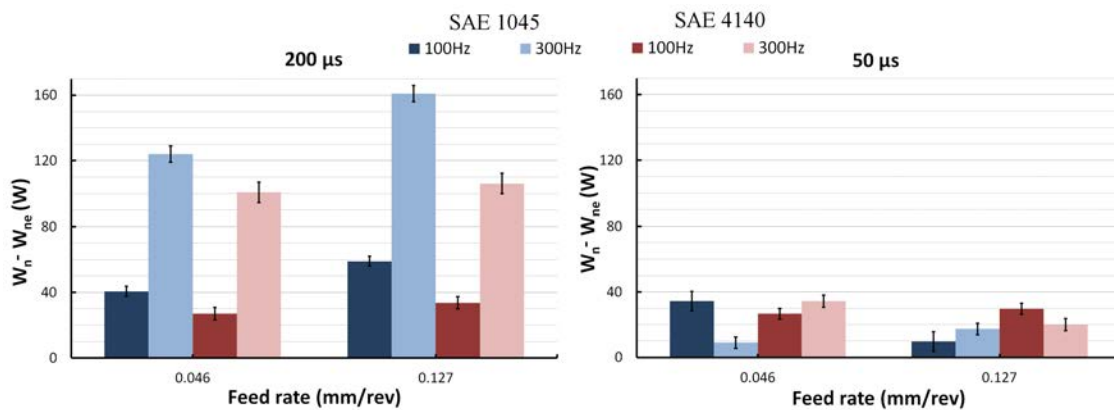


Figure 16: Power consumption comparison between conventional and assisted process for pulse durations of (a) 200 μ s and (b) 50 μ s.

In all the cases studied, the application of EPs has been observed to reduce the power consumption of the engine. The maximum reduction of power consumed was 160 W for a 0.127 mm/rev feed rate, 200 μ s pulses at 300 Hz charge frequency. However, for the 0.046 mm/rev feed rate, with 50 μ s pulses and 300 Hz frequency, the least power reduction was obtained, 9 W. The use of pulses with greater duration shows a larger reduction of the power consumed, especially if combined with high frequency values. For these cases, the power consumed tends to decrease about 105.4 W on average. For current pulses of lesser duration, the power consumed is attenuated, independently of the frequency utilized.

The energy consumed by the EPs generator is the sum of the energy provided in each pulse and the generator electronic control. The energy provided is different depending on the electrical configuration plus the energy consumed by the electronic control 8 W, as it is listed in Table 6. Then, to estimate the energy saved is calculated from the energy consumed by the generator with the registered power reduction found in Figure 16. The energy saved according to the electric configuration is also shown in Table 6.

Table 6: Energy consumed and saved under different electric configuration.

Frequency (Hz)	100	100	300	300
Pulse duration (μ s)	50	200	50	200
Energy consumed (W)	12.88	27.53	22.65	66.6
Energy saved (W)	10.2	12.7	2.48	38.8

The assisted turning process is more efficiently than conventional turning, especially when higher values of frequency and greater pulse duration are induced. However, the energy saved dramatically decrease when higher values of frequency and shorter pulse duration combination are used.

Sood et al. (2000) [53] defined that the specific cutting energy, the energy per unit of volume removed, is calculated as the quotient of the net active power and the material removal rate. The material removal rate Q_c is defined by:

$$Q_c = V_a \cdot A_c, \quad (3.1)$$

where V_a is feed rate (mm/min) and A_c is the removal material cross sectional area.

$$A_c = \pi \cdot [R^2 - (R - t)^2] = \pi \cdot t \cdot [D - t], \quad (3.2)$$

where R is the radius of the cylindrical workpiece and t is the thickness of the removal material ring. In Figure 17. The workpiece geometric parameters is showed.

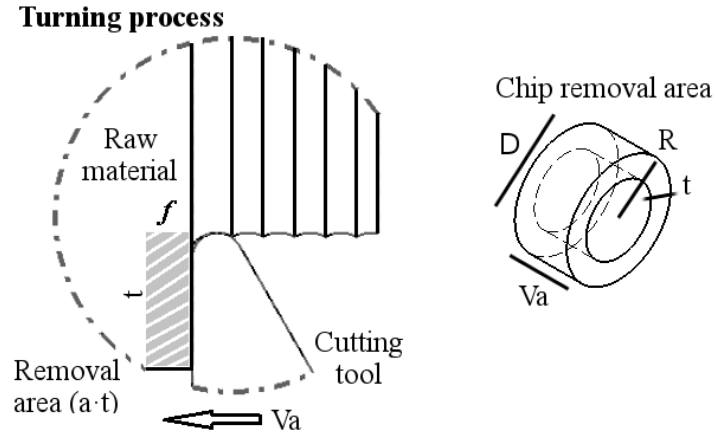


Figure 17: Mechanized workpiece geometric parameters.

The material removal rate is a function of the cutting conditions and of the operation performed. For a turning operation the material removal rate Q_c is:

$$Q_c = S \cdot f \cdot t \cdot (1 - t/D), \quad (3.3)$$

where S is the spindle speed (rpm), f is the feed rate (mm/rev), t is the depth of cut and D the diameter of the cylinder.

To compare the assisted process with the traditional process the percentage of reduction r_p experienced in the specific cutting energy is evaluated. This reduction is defined as:

$$r_p = \frac{E_s(\text{conventional}) - E_s(\text{assisted})}{E_s(\text{conventional})}, \quad (3.4)$$

where E_s is the specific cutting energy.

In Table 7 the reduction values obtained for the specific cutting energy are presented in percentages for 4140 and 1045 carbon steel, calculated from the previous equation for 0.046 and 0.127 mm/rev feeds, 50 and 200 μ s pulse durations and 100 and 300 Hz frequencies.

Table 7: Specific cutting energy percentage reduction.

f (mm/rev)	0.046				0.127			
Frequency (Hz)	100	100	300	300	100	100	300	300
Duration (μs)	50	200	50	200	50	200	50	200
SAE 1045 (%rp)	7.68	8.3	9.71	21.84	8.24	8.94	4.77	11.37
SAE 4140 (%rp)	5.28	10.99	5.21	24.2	2.49	15.1	5.73	25.83

The 4140 carbon steel registered a reduction of approximately 25%, independent of the feed used and for EPs of 200 μ s and a 300 Hz frequency. As such, the largest decrease in specific cutting energy is produced when the process is assisted *in situ* combining high frequency charges and a greater pulse duration. The results follow the same trend with those presented by Zhang et al. (2012) [41] the maximum decrease in specific energy was 54%, precisely when previously in the rolling process high frequency EPs are applied.

3.5 Conclusions

The electrically assisted turning process has been shown to be a feasible technique to improve the material machinability compared with the conventional turning process.

The surface roughness improves while the studied material hardness decreases when the turning process is electrically assisted, especially when smaller feed rates are used. However, the different frequency discharge and the pulse duration configurations influence on the surface roughness and material hardness neither present statistically significant differences, nor an obvious trend.

The power consumption and the cutting specific energy were reduced with the electropulses presence. The impact is particularly noticeable for high frequencies and long pulse duration.

The frequency and pulse duration seem to have an influence on improving the material machinability, but further studies need to be done with higher frequencies and longer pulse durations to determine the contribution tendencies of such parameters. However, when the process is assisted by electropulses, the reduction in the energy consumed by the spindle is always greater than the energy consumed by the pulse generator.

Chapter 4

Wire drawing process assisted by electropulsing

In previous chapters several mechanical parameters variations are observed in bottom bending and round turning processes. Although in this chapter is focused in study both the mechanical and metallurgic variations when the wire drawing process is assisted with electropulses. To do that, the electroplastic effects on wire drawing process assisted with different short time current pulses configurations are investigated experimentally and numerically. A current density of 185 A/mm^2 , a frequency range from 140 to 350 Hz and a pulse duration range from 100 to 250 μs are combined to electrically assisted the wire drawing process. The electropulsing influence is studied in several mechanical parameters, like drawing forces, stress - strain curves and the effective energy required for each electric configuration. The microstructure, material hardness, x-ray diffraction pattern and electro backscatter diffraction analysis of each specimen are compared in order to explain the mechanical variation. In conclusion, the results show greater metal forming depending on the different electropulsing configuration used to assist the wire drawing process.

4.1 Introduction

It is generally accepted that the wire drawing operation is characterized by the wire cross sectional area reduction due to plastic strain. To achieve that, a constant tensile force is applied to pull the material through a drawing die with a smaller cross section area, which has a particular design for this purpose. Talber and Avitzur (1996) [54] established that in a conventional drawing process the obtained thermal expansion is caused by friction and strength of the material due to plastic deformation. Nowadays, a current manufacturing tendency is to assist this conventional process with electropulsing to study the electroplasticity phenomenon where thermal and athermal effects are coupled. Much research in recent years has focused on this phenomenon which is revealed when an electromagnetic field is induced to the material with current pulses to achieve manufacturing improvements while it is plastically deformed. The main objective to assist the drawing process is to enhance the formability of the material. As it is reported in a recent review by Guan et al. (2010) [23], an increase of elongation, decrease of drawing forces, formability enhance and material microstructure

modifications have been achieved when different processes of severe plastic deformation were electrically assisted. Tang et al. (2000) [27] assisted with current the wire drawing process where, apart from increasing the elongation and decreases the drawing forces, a decrease of the ultimate tensile strength in 304 stainless steel wire was proved. Years later, Zhang et al. (2002) [25] stated that current pulses reduce the drawing forces and increase the ductility of the material when different metallic alloys are wire drawn with an industrial drawing speed of 60 m/min.

Numerical methods were widely used to understand the electric field influence on the material behavior. Dalong and Enlin (2009) [55] have analyzed the material plastic behavior affected by thermal expansion during wire drawing process assisted with current pulse. Therefore, the Joule effect impact on the deformed metal and its mechanical properties variations were numerically estimated. Tskhondiya and Beklemishev (2012) [56] have studied the contribution of thermal and athermal effects during the rolling process. They have proposed a constitutive equation to estimate the mechanical variation induced by the current pulses. Recently, Xie et al. (2015) [57] have studied the stress relaxation of AZ31B when bending process is electrically assisted. It was proved that the material springback is reduced when the process is electrically assisted and, to simulate this effect, they proposed a stress relaxation model. A numerical method have been also used in Sánchez et al. (2014) [44] to analyze different mechanical parameters such as stress-strain curves, stress distribution along the specimen, effective plastic strain and von Mises stresses. Furthermore, Roh et al. (2014) [58] proved the athermal electroplastic effects when tensile tests were done assisted with short time current pulses. This study showed how the aluminium formability enhanced when the tensile tests were assisted by current pulses with different current densities, pulse duration and frequency discharge, such that in each case the induced nominal electric energy changes.

4.2 Objectives

The aim of this work is to study the wire drawing process assisted with short time electropulses (EPs). Unlike the aforementioned studies, our objective here is to induce a constant nominal electric energy when the pulse duration and frequency discharge are combined in order to determine which parameter is more sensitive to assist the wire drawing process. To do that, an EPs generator was designed and manufactured with the purpose to minimize the thermal electroplastic effects. First, the influence of the electroplasticity effect on the drawing force when the process is assisted *in situ* with different EPs configurations is analyzed. Later, the study is focused on the stress-strain curve to determine the mechanical changes on the different assisted cases compared with those of the conventional process. Finally, a material characterization is carried out to determine which electrical configuration shows the greater material formability improvement in order to correlate the mechanical behavior variation with the metallographic structure for each specimen.

4.3 Methodology

4.3.1 Experimental configuration

The chemical composition of commercial material used in the current study is listed in Table 8. The metallic wires dimensions were 700 mm length, 1.6 mm diameter and 175 mm initial thread.

Table 8: Materials chemical composition and initial diameter.

Inox 308L	% C	% Cr	% Ni	% Si	% Mn	% P	% S	% Fe	ϕ_0 (mm)
	0.03	19	9.7	0.45	1.8	0.04	0.03	Balance	1.60 ± 0.01

The wire drawing process is performed by an Instron 4206 universal testing machine with a constant velocity of 0.5 m/min. A load cell, model reference sensortronics 98001, with a scale range of 1 Tn is used to measure the drawing forces. The electroplastic effects on the wire drawing forces are constantly registered with a data acquisition module. The manufactured parameters used are shown in Table 9. Specific polymeric matrixes are used to isolate the drawing die and the specimen from the machine. Powdered soap is used as wire drawing lubricant.

Table 9: Drawing operation parameters.

Drawing velocity (m/min)	Cross sect. area reduction (%)	Semi angle ($^{\circ}$)	Die type
0.5	15.6	6	Conic

A in-house EPs generator was built to discharge multiple positive pulses. The current parameters, like frequency, current density and pulse duration, were monitored by an oscilloscope. The EPs parameters used are listed in Table 10. The surface temperature variation was measured for each test with a contact K-type thermocouple.

Table 10: Electropulsing operation parameters.

Current intensity (A)	Current density (A/mm ²)	Pulse duration (μ s)	Frequency (Hz)	Av. output power (W) (W)
312	184.6	100	355	800
		150	237	
		200	177	
		250	142	

A schematic diagram and the engineering drawing of the wire drawing process assisted by electropulsing are presented in Figure 18.

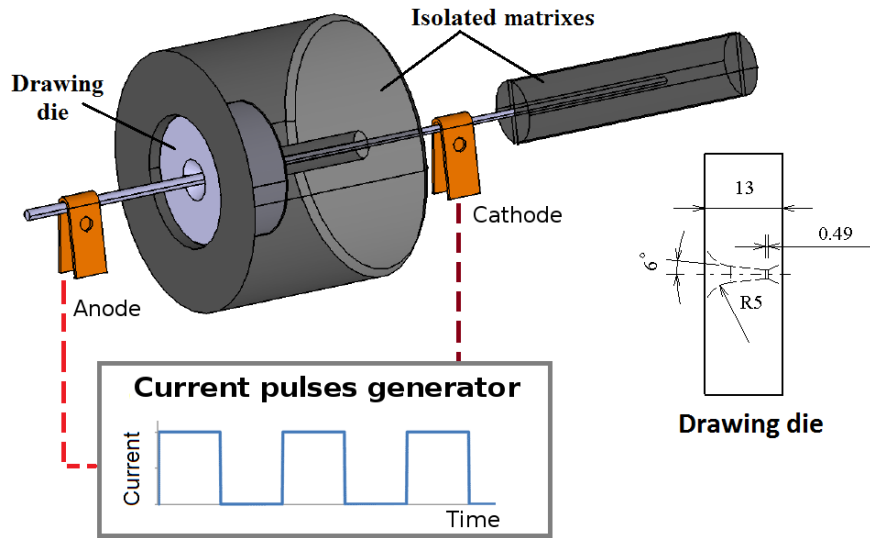


Figure 18: Electrically assisted wire drawing process schema.

After wire drawn all the specimens, a tensile test is performed by a Zwick / Roell Z100 universal tensile machine with a velocity of 2 mm/min and a load cell, model reference Xfoce P, was used with a scale range of 100 kN, in order to determine the mechanical behaviours. The material hardness was registered with a durometer (Micromet 5114). Moreover, The metallographic structure is observed by Nikon microscope (Optiphot-100) and x-ray diffraction (XRD) test is achieved to determine the amount of α martensite variation. Finally, the crystal preferred orientation, grain size and twins evolution are analyzed with electron backscatter diffraction (EBSD) technique, using a Scanning Emission Electron (SEM) microscope, model: JEOL JSM 7001-F, with field emission electron configuration of 20 kV. The software used to the post processing was Oxford Channel 5. More specifics details of the last two technique are commented in subsections 4.5.2 and 4.5.3.

4.3.2 Electropulses generator

As previously reported by Sánchez et al. (2015) [59], a self-made microcurrent pulse generator was designed and manufactured to minimize the thermal effects. This device was used in this particular case to electrically assist the wire drawing process. The generator has two circuits: the main circuit and the trigger control circuit. The function of the main circuit is to induce the current intensity in the test piece. The electrical discharges are controlled by several powers MOSFET, which determine when the EPs are transmitted through the material. A coil is needed to protect the transistors from sharp current drifts. The left hand side of Figure 19 outlines the main scheme of the microcurrent pulse generator, whilst the right hand side exhibits the EPs profile.

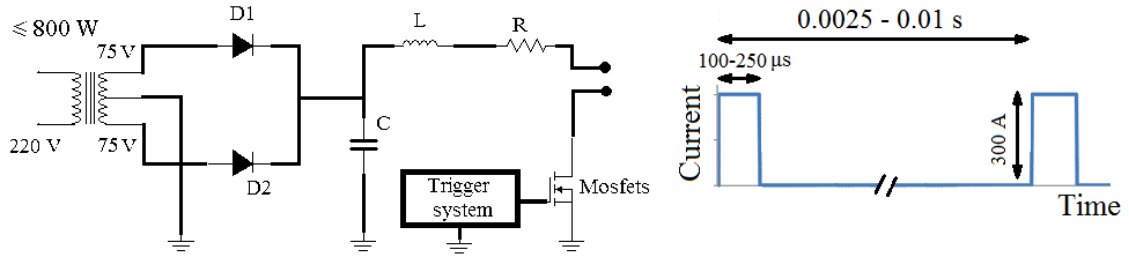


Figure 19: Microcurrent pulse generator schema and EPs profile.

The trigger system use stable and monostable oscillator circuits to control the frequency and the duration of induced EPs. The characteristics of EPs are: 100 to 250 μs pulse duration, 100 to 400 Hz frequency range and a maximum current intensity of 312 A. Similar electric parameters were used in a drawing process by Ye et al. (2014) [60], while the microstructure of Ti-6Al-4V alloy drawn strips were studied.

Figure 20 shows the generator operating curve. The area under the curve defines the generator operational region. Higher values above the curve cannot be used, otherwise the electronic equipment performance will be affected, and subsequently attenuate the output electrical parameters. The operational curve was obtained from the following equation.

$$P = I^2 \cdot R \cdot D \cdot f, \quad (4.1)$$

where P is the average electric output power (800 W), I is the current intensity, R is the electric resistance, D is the pulse duration and f is the frequency pulse discharge.

The estimated curve (dashed line) represents the average maximum output power, i.e., 800 W. The points of the curve define the configuration of frequency and pulse duration used to induce the maximum output power (800 W). Although the four configurations transmit the same electric output power to the material, different frequency and pulse duration values are used in each configuration. The mechanical behaviors during the conventional and assisted processes are compared when these four electrical configurations are used. It is also analyzed the stress – strain material behavior independently of the average output power during a wire drawing process assisted with EPs.

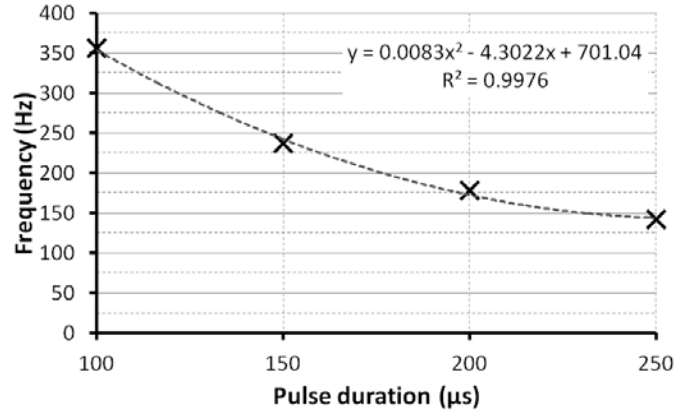


Figure 20: Maximum electric output power configuration.

4.3.3 Numerical simulation

As in the experiments, the wire specimens were numerically analyzed during two consecutive tests: first in a wire drawing process and then in a tensile test in order to assess the influence of the material response of both the internal stresses and the effective plastic strain distribution developed at the end of the wire drawing deformation stage. The mechanical formulation used is based on that proposed by Celentano et al. (2011) [33]. The governing equations together with the material constitutive and contact-friction models are discretized within the framework of the finite element method according to the numerical approach detailed by Celentano et al. (2004) [34]. In this study, axisymmetric conditions were assumed for both tests. In the wire drawing simulation, a Coulomb-type law with a friction coefficient of 0.07 was considered. Only relevant details of the constitutive material model are described below.

A classical plasticity model was adopted to describe the material behavior during the bending process in which the von Mises function F is defined as:

$$F = \sqrt{3 \cdot J_2} - \bar{\sigma}, \quad (4.2)$$

where J_2 is the second invariant of the deviatoric part of the stress tensor σ ($\sigma_{eq} = \sqrt{3 \cdot J_2}$ is the so-called equivalent or von Mises stress), and $\bar{\sigma}$ is the flow stress given by the linearization of the Ludwik equation:

$$\bar{\sigma} = \sigma_y + k \cdot \bar{\epsilon}, \quad (4.3)$$

where $\bar{\epsilon}$ is the effective plastic strain, k is the parameter aimed at characterizing the isotropic strength behavior of the material and σ_y is the yield strength defining the initial material elastic bound. The choice of the linear hardening law expressed by the last equation is justified by the fact that the values of initial yield strength and ultimate tensile strength (UTS) approximately fit a linear interpolation within the tensile strain interval of this material (which exhibits a relatively low ductility with a tensile rupture elongation of 6% to 8%).

The material parameters of the 308L alloy used in the numerical simulations are summarized in Table 11. The elastic parameters E and ν were taken from literature while that initial yield strength σ_y was obtained from tensile tests of the as-received material.

As reported by Roh et al. (2014) [58], this value is assumed here to be independent of the effect of electrical pulses. On the contrary, Liu et al. (2015) [61] reported that this effect has been long recognized to have a marked influence on the hardening response. In this context, the methodology proposed to separately determine the strength coefficient k for the standard and electrically assisted wire drawing processes consists basically in the simultaneous fulfilment, for a given k value, of two conditions:

1) Fitting of the numerical wire drawing force to the corresponding experimental measurement during the simulation of the wire drawing process.

2) Fitting of the numerical UTS to the corresponding experimental measurement during the simulation of the tensile test considering while both the internal stresses and the effective plastic strain distribution developed at the end of the wire drawing process.

The resulting k values obtained with this procedure for the standard and electrically assisted wire drawing process are listed in Table 11.

Table 11: Material parameters of 308L alloy used in the numerical simulation processes.

Young's modulus E [GPa]	195
Poisson's ratio ν	0.30
Initial yield strength σ_y [MPa]	850
Strength coefficient k [MPa]	1700
Strength coefficient k [MPa] (electrically assisted)	960

4.4 Results and discussion

4.4.1 Thermal behavior

The maximum bulk temperature is measured right after the drawing die with a type K thermocouple to determine the thermal variation. The recorded temperatures for all the combinations of pulse duration and frequency discharge are presented in Figure 21. The maximum bulk temperature value is an instantaneous measure which is registered beneath the drawing die, where current density reaches the maximum value.

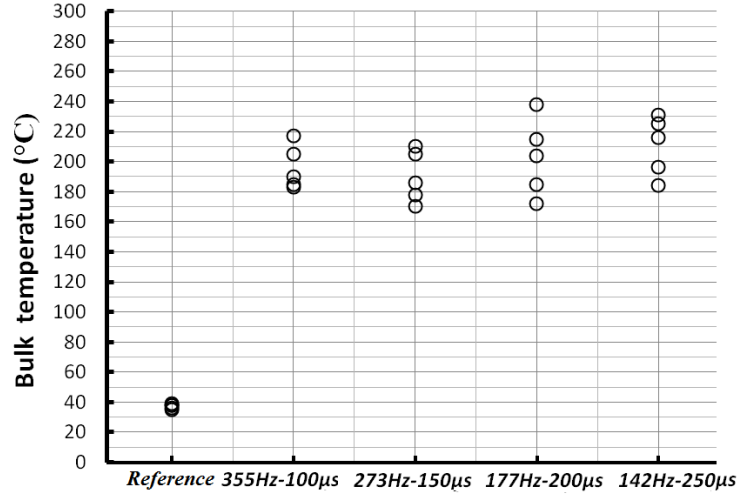


Figure 21: Maximum bulk temperature of the conventional and assisted processes.

The maximum thermal values registered in the assisted process are considerably lower than the conventional annealing temperature used to reduce internal stresses for stainless steel (450-800 °C) and much lower than the static recrystallization temperature (1100-1400 °C). Perkins et al. (2007) [37] registered similar thermal values when several metallic materials were studied under compression tests. Roh et al. (2014) [58] found also same thermal values on aluminium when the tensile test is assisted with greater EPs configurations. Then, it can be assured that the mechanical variation found in this study could not be justified only by the thermal contribution and, therefore, the athermal electroplastic effects are also responsible for enhancing the mechanical formability.

The instantaneous rise of temperature, when the specimen is induced by short time EPs, can be estimated as an adiabatic condition. The average temperature rise of the specimen by Joule heating is state as Conrad and Sprecher (1989) [9]

$$\Delta T = (c \cdot \rho)^{-1} \cdot \gamma \cdot \left(\frac{I}{S}\right)^2 \cdot D \cdot f, \quad (4.4)$$

where S is the specimen cross sectional area, γ ($7.2 \cdot 10^{-7} \Omega \text{ m}$), c ($500 \text{ J/kg} \cdot ^\circ\text{C}$) and ρ ($8 \cdot 10^3 \text{ kg/m}^3$) are the electrical resistivity, the specific heat and the density, respectively. The instantaneous maximum increase of temperature is estimated to be up to 216 °C for an adiabatic condition. A convection thermal dissipation by natural convection is estimated to be 3 °C approximately. Therefore, the thermal dissipation is not significant and can be neglected.

Then, based on the high-rate heating of electropulsing, an instantaneous thermal stress can be presented, and the maximum thermal expansion stress can be written as Tang et al. (1993) [10]:

$$\sigma_{max} = E \cdot \alpha \cdot \Delta T, \quad (4.5)$$

where E (195 GPa) is Young's modulus and α ($17.3 \cdot 10^{-6} \text{ m}/(\text{m} \cdot ^\circ\text{C})$) is the thermal expansion coefficient. Thus, the stainless steel will bear an instantaneous compressive stress of 0.7 GPa.

The effects responsible for the mechanical variation can be computed to many factors when the process is assisted with EPs, some of those factors are the high-rate heating, thermal compression stress, microstructure modification and a release of internal stresses. The microstructure and material characterization sections are focused on discussing which of these factors are the responsible mechanisms for the mechanical behavior variation.

4.4.2 Electropulsing effect

The acquired wire drawing forces are presented in Figure 22. The curves plotted correspond to the conventional wire drawing (CD) process (black line) and the different electrical wire drawing (EAD) configurations (coloured lines) used to assist the process with the same output power. These wire drawing tests were performed with the working and electrical parameters mentioned in Tables 9 and 10, respectively.

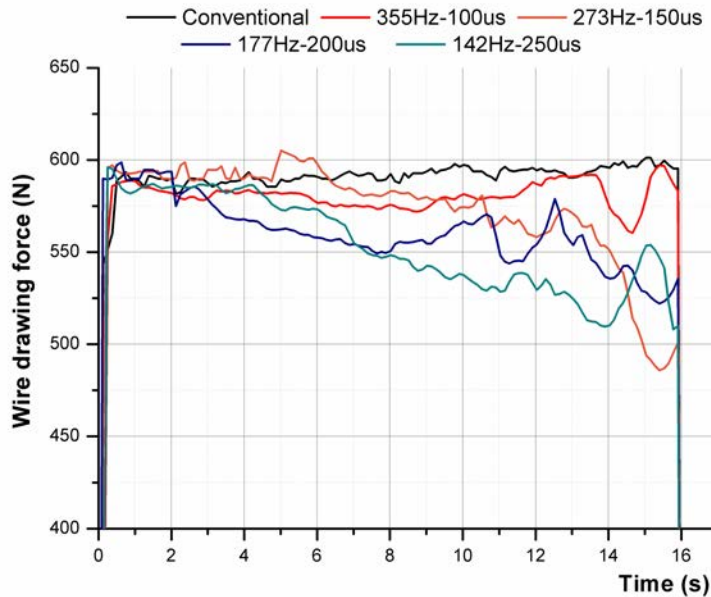


Figure 22: Wire drawing forces for convectional and assisted processes.

The results indicate that the assisted process decreases the drawing forces needed to plastically deform the material. The conventional process has a drawing force with a stationary trend, while the assisted processes have a drawing force with a decreasing trend. The registered average drawing forces are 582.8 N for CD process, 555 N for the EAD process with 355

Hz and 100 μs , 547.2 N for the EAD process with 273 Hz and 150 μs , 534.7 N for the EAD process with 177 Hz and 200 μs and finally 520.8 N for the EAD process with 142 Hz and 250 μs . This reduction in drawing forces is due to the electroplasticity phenomenon, which combines thermal and athermal effects. This phenomenon achieves a flow stress reduction to plastically deform the material and induces a greater material elongation improving consequently the material formability. In a previous work, Sánchez et al. (2014) [44], reported a reduction of bending forces up to 18% when bending strips of aluminium. Song and Wang (2012) [8] reported similar conclusions when titanium strips were drawn assisted with an electric field. Furthermore, Zhang et al. (2012) [41] proved that the electroplasticity also enhances the material machinability particularly when metallic alloys are previously drawn assisted by EPs. Here it is reported an *in situ* induction of electroplasticity phenomenon to the metallic material by short time EPs during the wire drawing process. In the present work, the experiments were done for four different frequency discharge and pulse duration configurations, while the induced output power remained constant (i.e., 800 W) in every configuration.

In order to study the mechanical behavior, the experimental results of the power consumed by the assisted drawing process $N_a = (\overline{F} \cdot v)_a$ are compared with the power consumed by the conventional process $N_c = (\overline{F} \cdot v)_c$. The result is an experimental coefficient represented by the following equation:

$$N^* = \frac{(\overline{F} \cdot v)_a}{(\overline{F} \cdot v)_c}, \quad (4.6)$$

where N^* is the experimental coefficient, \overline{F} is the average drawing force and v is the drawing velocity.

This coefficient determines the mechanical variation response of the material when the electrical parameters are used (i.e., frequency and pulse duration) to assist the wire drawing process. In all cases the drawing forces were continuously registered by the tensile machine data acquisition module considering the same drawing velocity. Therefore, the averaged force is obtained in each test by integrating the area under the curve for a period of time of 16 sec.:

$$\overline{F} = \frac{1}{T_t} \cdot \int_0^{T_t} F(t) \cdot dt. \quad (4.7)$$

Figure 23 shows the experimental coefficient N^* of each electrical configuration. These configurations have the same electrical output power of 800 W, a drawing velocity of 0.5 m/min and a cross sectional area reduction of 15.6%. Each experimental value is the average of five values and the error bars correspond to a 95% confidence interval.

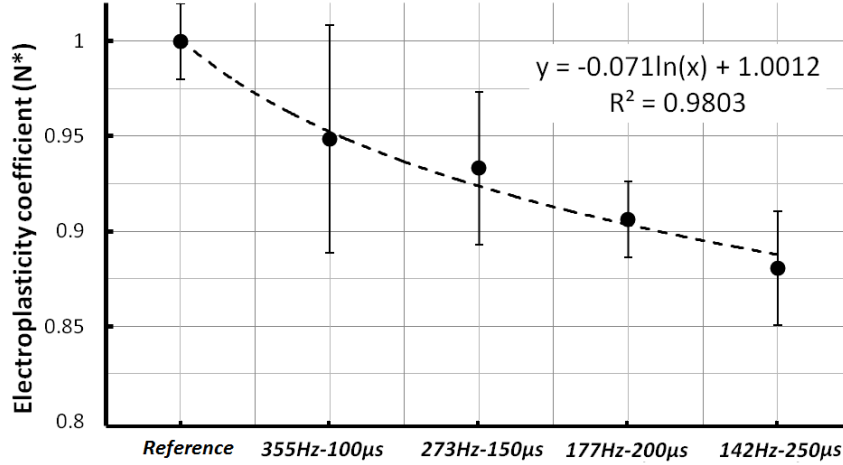


Figure 23: Electroplastic experimental fitting coefficient.

The configuration of longer pulse duration and a lower frequency discharge decreases the needed energy for wire drawing up to 11.9% on average. While a shorter pulse duration and higher frequency discharge configuration decreases, the needed energy for wire drawing increases up to 5.1%. The two others electrical configurations follow the same trend, for longer pulse duration and smaller frequency discharge, the applied drawing force to plastically deform the material decreases. Similar results have been reported by Zhu et al. (2013) [62], whereby a drawing force drop of 14.6% was found when the drawing process is assisted by EPs. They used similar electrical parameters: a current density range from 184 to 283 A/mm^2 , a frequency discharge range from 150 to 250 Hz and a pulse duration of 80 μs .

The relative energy efficiency is expressed by the comparison of the assisted process power consumption minus the average output power induced by the generator with respect to the conventional process average power consumption, as shown in the following equation:

$$\eta = \frac{\overline{N}_a - N_e}{\overline{N}_c}, \quad (4.8)$$

where \overline{N}_a is the assisted process average power consumption, N_e is the generator induced average output power and \overline{N}_c is the conventional process average power consumption.

Figure 24 shows the relative energy efficiency as a percentage of average power consumption for the different electric current configurations used to assist the wire drawing process.

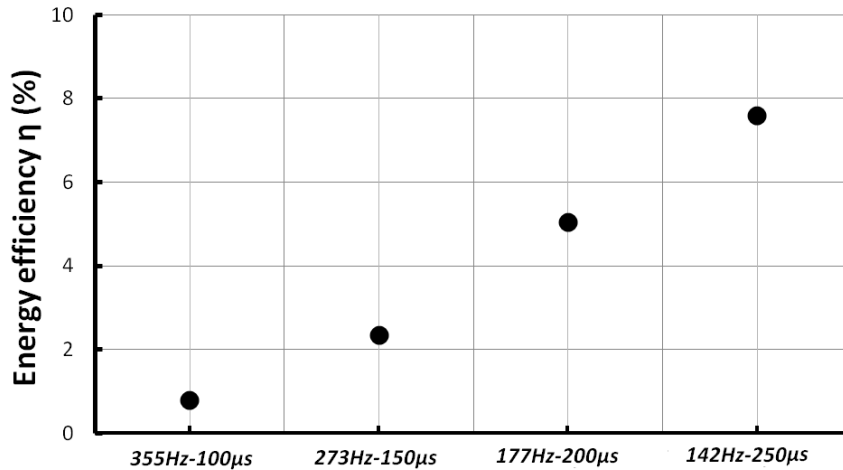


Figure 24: Relative energy efficiency for the different assisted processes configurations.

The relative energy efficiency improves up to a 7.6% when the EAD process combine pulses duration of 250 μ s and frequency discharge of 142 Hz. When the EAD process combine pulses duration of 100 μ s and frequency discharge of 355 Hz, the relative energy efficiency only improves 0.8% with respect to the CD process.

4.4.3 Mechanical behavior

Based on the experimental results, a numerical analysis to comprehend the stress-strain distribution during the wire drawing process was performed. To achieve this, the same cross sectional area reduction and friction coefficient were used. Figure 25 shows the von Mises and effective plastic strain distributions along radial coordinates for CD specimens (Fig. 25a) EAD specimens (Fig. 25b). The horizontal axis in both graphs represents the radial coordinate of the specimen, where 0.0 is the center point of the specimen and 0.735 mm is the wire surface.

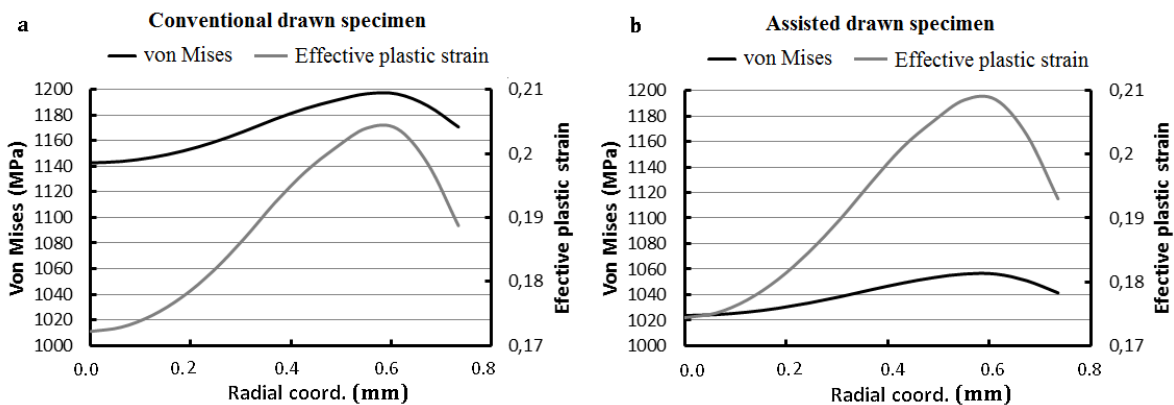


Figure 25: Effective plastic strain and von Mises stress evolution along radial coordinate.

The first difference is observed in the von Mises stresses, where the CD specimen reaches 1142 MPa at the inner region and 1200 MPa at the surface, while the EAD specimen reaches 1024 MPa at the inner region and 1057 MPa at the surface. Furthermore, the EAD specimen present a higher effective plastic strain distribution in both inner and surface regions as compared with the conventionally drawn specimen. These results indicate that the specimens assisted with EPs show smaller internal stresses and higher effective plastic strain evolution along the radial coordinate. Therefore, it could be ascertained that the material formability is enhanced when EPs treatment is used to assist the drawing process.

Once all the samples were drawn, a tensile test is performed to observe their mechanical behavior. Figure 26 shows the simulation of the average mechanical behavior variation when the samples are CD (black line) and when the samples are EAD with current pulses (grey line). Although different drawing forces were found when different electrical configuration were used to assisted *in situ* the drawing process, the tensile test result shows a common mechanical behavior for all the specimens assisted with different electrical configurations. The UTS variation between the EAD specimens with respect to the CD specimens is given by a reduction of 120 MPa. Tang et al. (2000) [?] reported a similar UTS decrease when 304L stainless steel was drawn assisted with current pulses. Magargee et al. (2013) [24] demonstrated a decrease of the yield stress when the tensile test is assisted with EPs. In our study, the yield strength decreases about 150 MPa when the specimens were electrically assisted. Finally, the material elongation has increased near 10% for the assisted specimens. This elongation results are in a higher magnitude with respect to the one stated by Tang et al. (2000) [27]. However, Zhang et al. (2002) [25] reported higher elongation values when the wire drawing process is assisted with EPs with drawing velocities within the range from 6 to 60 m/min.

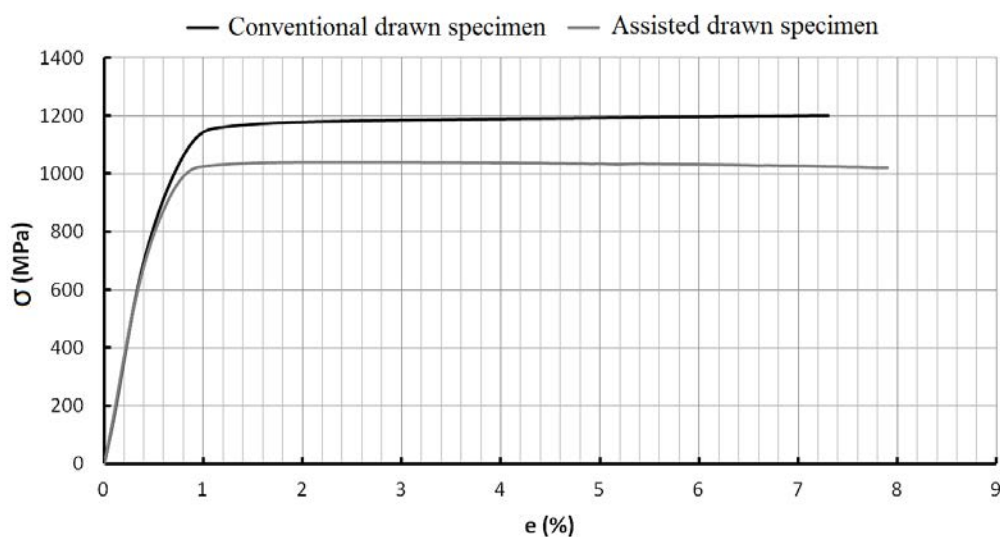


Figure 26: Tensile mechanical behavior of CD and EAD specimens.

4.4.4 Material hardness

The material hardness of the wire drawn specimens was registered. Figure 27 shows the material hardness distribution for a cross sectional area of as-received (B), CD and AED specimens. Each experimental value is the average of ten values and the error bars correspond to a standard deviation.

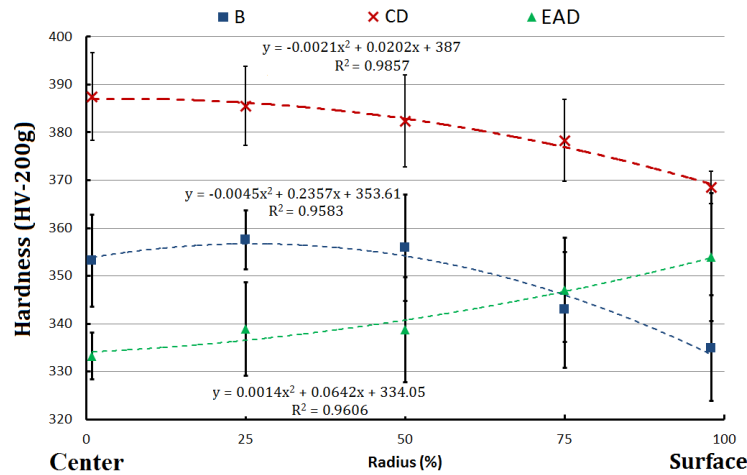


Figure 27: Material hardness distribution along the cross sectional area.

The hardness results show that the two specimens, B and CD, follow a similar hardness trend distribution, i.e., lower hardness values at the surface and higher hardness values at the inner regions. The CD specimens present higher material hardness values due to the fact that the cold working level increase in this case. The EAD specimens show a lower surface hardness compared with the CD specimens, which means that the EP treatment has induced in the specimens an annealing process. Furthermore, a different hardness trend distribution was found, where the inner regions have a lower hardness than that of the surface. A high-rate heating caused by a severe plastic deformation when the EAD specimen is forced to go through the drawing die could explain the surface irregularities in this sample (see Figure 28c). These irregularities could be explained by at least two reasons: first, the temperature expands non uniformly the specimen cross sectional area and, therefore, higher surface stresses during the plastic deformation could be achieved and, second, the specimen material adhesions can also be presented between the wire specimen and the drawing die because of the high temperature.

4.5 Metallography

4.5.1 Microstructure

The 308L stainless steel is an austenitic steel (FCC structure) with low quantity of carbon ($\leq 0.03\%$). Due to the low quantity of carbon, chromium carbides precipitation are likely to be found at the grain boundaries, which is possible if the steel is thermally treated with sensitization temperatures (450-850 °C) for a long period of time. On the other hand, the unstrained material behavior could be achieved with temperatures of 400 °C when regular

thermal treatments are used. The mechanical variation found is due to an unstrained material behavior which was induced by the EPs treatment.

In order to study the microstructure evolution, a conventional process of grinding and polishing is done up to a grain size of $0.05\ \mu\text{m}$. Figure 28 shows the polished surfaces for B, CD and EAD specimens without chemical attacking. Figure 28a shows a longitudinal section where cracks and inclusions oriented along the drawing direction are presented in the three specimens. It is also observed that inclusions bands are preferential paths to the cracks propagation. Figure 28b and 28c show the material cross sectional areas for CD and EAD specimens, respectively. The main difference is that the assisted specimen has surface irregularities and cracks with a radial orientation as it is shown in Figure 28d. These defects could be explained by thermal expansion stresses estimated in the Thermal behavior section. Both findings, i.e., cracks and a non uniform surface, are significant drawbacks when the process is assisted with respect to the conventional process, specially the cracks that could bring an early fatigue failure or intergranular corrosion.

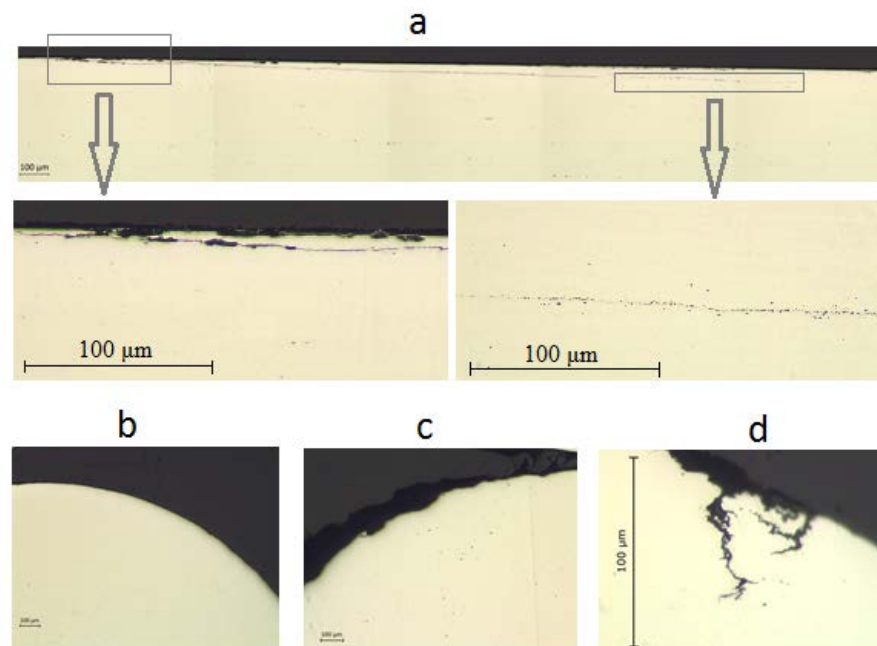


Figure 28: Surface observation of B material (a), CD specimens (b), EAD specimens (c) and cracks found in the EAD specimens (d).

The material surface is revealed with a metallographic electrolytic etching with oxalic acid as described in ASM Metal Handbook (2004) [63], in order to observe the material microstructure. Figure 29 shows the material microstructure for the B, CD and EAD specimens. In this figure the wire drawn specimens are characterized by microstructure without obvious grain boundaries. Song and Wang (2012) [8] proved that the electropulsing treatment changed significantly the microstructures, where a fine recrystallization grain and detwinning in the interior of grains are observed. During the recrystallization process the microstructure is rearranged by reducing the crystal dislocations number while increasing the number of

effective slip bands formed. Then, the electropulsing treatment due to coupling thermal and athermal effects could rearrange the microstructure by annihilating dislocations, as it was stated by Xie et al. (2015) [57], and enhancing the nucleation rate of recrystallization, as it was proved by Xu et al. (2007) [19] when AZ31 was drawn assisted with an electropulsing treatment. Later, Xu et al. (2011) [64] proved a faster recrystallization process when a drawn magnesium alloy was assisted with EPs. Finally, it is also seen that the cracks extended in a radial orientation are not linked to the grain boundaries, not either to the twins. Therefore the thermal expansion stresses seems to be the main factor to the cracks generation.

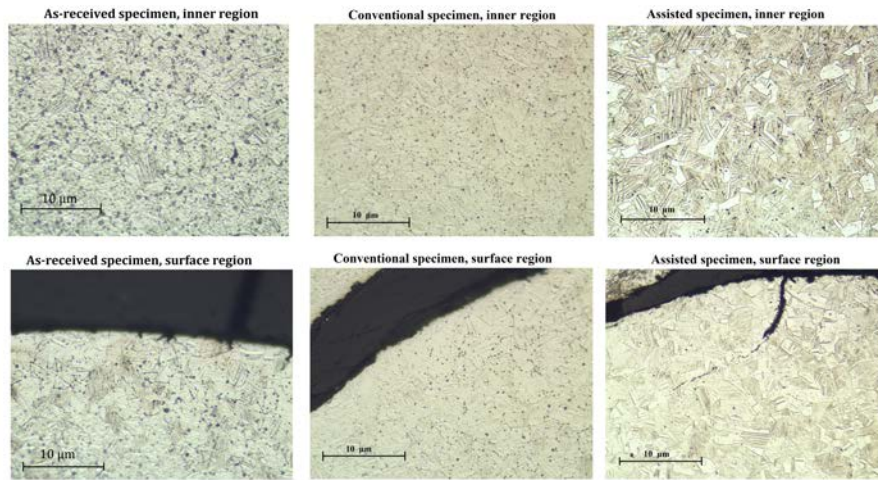


Figure 29: Etched microstructure of B (a), CD (b) and EAD (c) specimens.

An XRD analysis was carried out as it is described in the following subsection, to compare the phase transformation distribution and the volume fraction of each phase between the different wire drawn configurations.

4.5.2 Material phase determination

In some materials, like 308L stainless steel, during wire drawing process a phase transformation is achieved due to the increase of plastic deformation. That plastic deformation induces a transformation of austenite to martensite. Therefore, it is proposed here to study the phase transformation when the specimens are drawn conventionally and assisted with electropulsing. To do that, XRD patterns are done for identifying and evaluating the transformation induced by the plastic strain in 308L of an B, CD and an EAD specimens. A PANalytical X'Pert PRO MPD Alpha1 diffractometer with a θ - 2θ Bragg-Brentano configuration was used with a $\text{Cu} \cdot \text{K}\alpha_1$ radiation ($\lambda = 1.5406 \text{ \AA}$) and a Ge (111) primary monochromator. A phase analysis of the material was performed with a θ - 2θ scan from 40° to 153° with step size of 0.017° and measuring time of 150 seconds per step. The XRD patterns of B, CD, EAD material are presented in Figure 30.

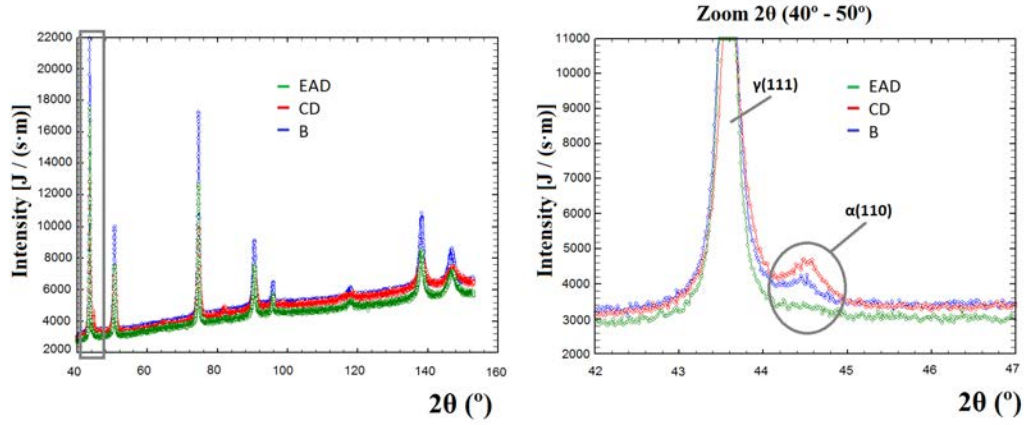


Figure 30: (a) XRD profile of B, CD and EAD specimens. (b) Main differences of phases composition at $\gamma(111)$ and $\alpha(110)$.

It can be seen clearly that the assisted drawing configuration compare with respect to the conventional process has significant influences on phases. The XRD patterns shows an α martensite phase formation due to a large amount of plastic strain induced when a conventional drawing process is carried out, as shown in Figure 30b. On the contrary, the α martensite formation is almost absent when the drawing process was assisted with EPs. The microstructure observation and the XRD patterns seem to show a dynamic recrystallization process (DRX) takes place at a relatively low temperature within a short time in those specimens assisted with EPs.

The quantitative estimation of phases by XRD is listed in Table 12. The estimation is based on the total integrated intensity of all observed diffraction peaks for each phase. Amar et al. (2004) [65] and Jorba (1990) [66] stated the integrated intensity I of any diffraction peak from the different phases according to the following equation,

$$I_{hkl} = k \cdot R_{hkl} \cdot \frac{V_i}{2 \cdot \mu}, \quad (4.9)$$

where I_{hkl} is the integrated intensity ($J/(s \cdot m)$) for (hkl) Miller indices of a specific phase: α or γ , k is the instrument factor; R_{hkl} is the material scattering factor and depends on θ , interplanar spacing of hkl, chemical composition and the crystal structure of the phase, V_i is the volume fraction of phase (m^3) and μ is the linear absorption coefficient (m^{-1}).

k is constant for each specific experimental conditions and diffractometer which is defined as,

$$k = \frac{I_0 \cdot A \cdot \lambda^3}{32 \cdot \pi \cdot r} \cdot \left[\left(\frac{\mu_0}{4 \cdot \pi} \right)^2 \cdot \frac{e^4}{m^2} \right], \quad (4.10)$$

where I_0 is the intensity of the incident beam ($J/(s \cdot m)$), r is the radius of diffractometer circle (m), μ_0 is a constant ($kg \cdot m \cdot C^{-2}$), A is the cross sectional area of incident x-ray beam (m^2), λ is the wavelength of incident x-ray beam (m), e and m are the charge (C) and mass (kg) of electron respectively

The material scattering factor is expressed as follow,

$$R_{hkl} = \frac{1}{v^2} \cdot [F_{hkl}^2 \cdot p \cdot \frac{1 + \cos^2 2\theta}{\sin^2 \theta \cdot \cos \theta}] \cdot (e^{-2M}), \quad (4.11)$$

where v is the volume of unit cell (m^3), F_{hkl} is the structure factor for reflecting plane (hkl), p is the multiplicity factor of each plane diffraction family and e^{-2M} is the Debye-Waller temperature factor.

In Table 12 the experimental Bragg angles associates to the Miller index for two different systems FCC and BCC for the diffraction conditions are listed. Also, it is collected the integrated intensity and the material scattering factor related to each crystal structure of the phase for the three specimen conditions B, CD, EAD specimens. First of all, it is noticed several differences of the integrated intensities depending on the drawing configuration. The assisted drawn specimen clearly shows no difference in the integrated intensity values of austenite, although the peak intensity of α martensite is practically neglected with respect the conventional specimen. Then, the absent of α martensite peak could be explained that the formation of strain-induced martensite is attenuated due to the electropulsing influence. Therefore, it is estimated the percentage of volume fraction of each phase, in order to be able to compare the effect of EPs on strain-induced martensite transformation.

Then, to estimate the steel containing fcc-austenite (γ) and the bcc-martensite (α) the general equation can be expressed as,

$$I_\gamma = \frac{K \cdot R_\gamma \cdot V_\gamma}{2 \cdot \mu}; \quad I_\alpha = \frac{K \cdot R_\alpha \cdot V_\alpha}{2 \cdot \mu}. \quad (4.12)$$

Additionally,

$$V_\gamma + V_\alpha = 1. \quad (4.13)$$

It is not considered V_ϵ because is not observed during the metallographic observations.

Therefore, the volume fraction of austenite and martensite can be derived for numerous peaks as,

$$V_i = \frac{\frac{1}{n} \cdot \sum_{j=1}^n \frac{I_i^j}{R_i^j}}{\frac{1}{n} \cdot \sum_{j=1}^n \frac{I_\gamma^j}{R_\gamma^j} + \frac{1}{n} \cdot \sum_{j=1}^n \frac{I_\alpha^j}{R_\alpha^j}}, \quad (4.14)$$

Table 12: XRD contribution for the different studied specimens.

System	h	k	l	$2\theta_{exp}$	As-received		Conventional		Assisted	
					R_{hkl}	I_{hkl}	R_{hkl}	I_{hkl}	R_{hkl}	I_{hkl}
FCC	1	1	1	43.576	$2.5 \cdot 10^8$	5740.50	$2.52 \cdot 10^8$	4484.60	$2.51 \cdot 10^8$	4814.93
	2	0	0	50.645	$1.1 \cdot 10^8$	3892.45	$1.13 \cdot 10^8$	3665.35	$1.12 \cdot 10^8$	3260.41
	2	2	0	74.612	$5.2 \cdot 10^7$	6902.70	$5.26 \cdot 10^7$	5823.36	$5.24 \cdot 10^7$	5709.34
	3	1	1	90.520	$5.7 \cdot 10^7$	3868.93	$5.77 \cdot 10^7$	3215.07	$5.74 \cdot 10^7$	3671.55
	2	2	2	95.880	$1.7 \cdot 10^7$	689.10	$1.70 \cdot 10^7$	498.22	$1.69 \cdot 10^7$	677.29
	4	0	0	117.877	$1.1 \cdot 10^7$	833.39	$1.10 \cdot 10^7$	953.65	$1.09 \cdot 10^7$	957.97
	3	3	1	138.225	$2.7 \cdot 10^7$	7090.79	$2.74 \cdot 10^7$	6604.96	$2.72 \cdot 10^7$	4945.70
	4	2	0	146.804	$6.8 \cdot 10^7$	4485.19	$6.98 \cdot 10^7$	3959.97	$6.87 \cdot 10^7$	4472.63
BCC	1	1	0	44.451	$8.8 \cdot 10^7$	563.95	$8.8 \cdot 10^7$	1158.66	$8.81 \cdot 10^7$	448.81
	2	0	0	64.553	$1.1 \cdot 10^7$	29.06	$1.1 \cdot 10^7$	221.32	$1.13 \cdot 10^7$	0
	2	1	1	81.820	$1.9 \cdot 10^7$	105.08	$1.9 \cdot 10^7$	416.38	$1.90 \cdot 10^7$	129.88
	2	2	0	98.359	$6.06 \cdot 10^6$	0	$6.10 \cdot 10^6$	0	$6.07 \cdot 10^6$	0
	3	1	0	115.553	$1.1 \cdot 10^7$	3.26	$1.1 \cdot 10^7$	3.26	$1.08 \cdot 10^7$	0
	2	2	2	135.753	$4.4 \cdot 10^6$	13.31	$4.32 \cdot 10^6$	13.31	$4.36 \cdot 10^6$	13.31

where $i = \gamma$ or α in this instance and n is the number of peaks examined.

The above equation estimate the volume fraction of austenite (γ) and martensite (α) in 308L stainless steel from a single XRD scan by measuring the integrated intensity of each reflecting plane of the respective phases and calculating the parameter R_{hkl} for each phase. In Table 13 is calculated the volume fraction of each phase in order to measure the martensite (α) in each specimen.

Table 13: Percentage of volume fraction of each phase for the different studied specimens.

V. fraction	As-received	Conventional	Assisted
V_γ [%]	96.72	89.12	96.77
V_α [%]	3.28	10.88	3.23

The results reveal that electropulsing treatment inhibits the formation of α martensite during the wire drawing process. On the contrary, the percentage of volume fraction of α martensite phase increase more than double when the specimens were conventional wire drawn. The smaller presence of this phase explains that the formation of strain-induced martensite is attenuated when the wire specimen is plastic strain with the electropulses influence. Similar results are found in the literature, Zhang et al. (2002) [25] presented also a decrease of α martensite phase in Cr17Ni6Mn stainless steel when the wire drawing process is assisted with current pulses. In our study, it has been proved the absence of ε martensite beyond the threshold given by the XRD technique. Nevertheless, Amar et al. (2004) [65] described the presence of this phase in 304L stainless steel during different types of plastic deformation. Therefore, it is assumed that the whole ε martensite has been transformed into

α martensite.

Information about material texture is needed to determine if there is any preferential microstructural orientation, in particular when the process is assisted with electropulsing. To do that, the quotient between the maximum intensity and the material scattering factor of each Miller index only for the austenite phase in the three specimens are listed in Table 14.

Table 14: Analysis of the preferential microstructural orientation in austenite phase.

h	k	l	$2\theta_{exp}$	As-received	Conventional	Assisted
				$I_{max_{hkl}} / R_{hkl} \cdot F$	$I_{max_{hkl}} / R_{hkl} \cdot F$	$I_{max_{hkl}} / R_{hkl} \cdot F$
1	1	1	43.576	$2.1 \cdot 10^{-8}$	$1.7 \cdot 10^{-8}$	$6.4 \cdot 10^{-9}$
2	0	0	50.645	$3.0 \cdot 10^{-8}$	$3.0 \cdot 10^{-8}$	$9.6 \cdot 10^{-9}$
2	2	0	74.612	$9.0 \cdot 10^{-8}$	$8.2 \cdot 10^{-8}$	$2.8 \cdot 10^{-8}$
3	1	1	90.520	$3.9 \cdot 10^{-8}$	$3.5 \cdot 10^{-8}$	$1.5 \cdot 10^{-8}$
2	2	2	95.880	$2.3 \cdot 10^{-8}$	$1.8 \cdot 10^{-8}$	$8.7 \cdot 10^{-9}$
4	0	0	117.877	$4.1 \cdot 10^{-8}$	$4.7 \cdot 10^{-8}$	$1.8 \cdot 10^{-8}$
3	3	1	138.225	$1.3 \cdot 10^{-7}$	$1.2 \cdot 10^{-7}$	$3.3 \cdot 10^{-8}$
4	2	0	146.804	$3.0 \cdot 10^{-8}$	$2.6 \cdot 10^{-8}$	$1.1 \cdot 10^{-8}$

Table 14 reveals that the Miller index (220) and (331) present higher values compare with respect to the other Miller index contribution, independent of the specimen configuration studied. Figure 31 presents the Miller indices contributions for the three different configuration.

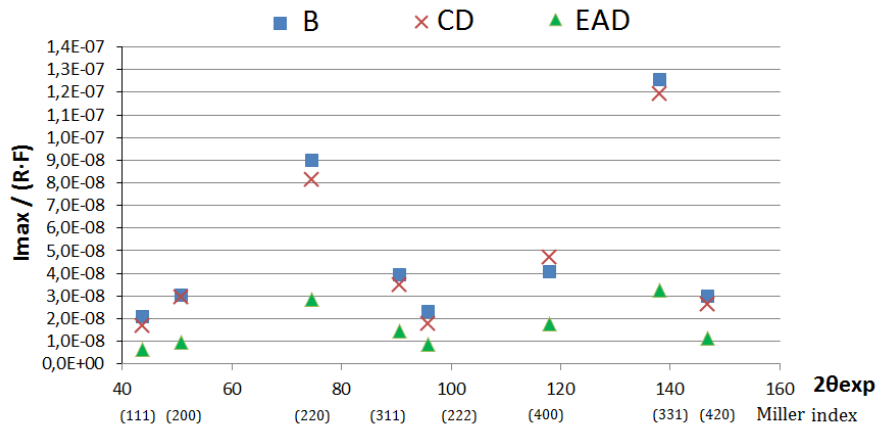


Figure 31: Preferential microstructural orientation for the B, CD and EAD specimens.

Figure 31 shows that the three different studied specimens follow the same trend. These results denote that the material has texture, which means a preferential microstructural orientation to the Miller index (220) and (331). Therefore, the wire specimens tend to orientated to the two aforementioned Miller index when they wire drawing processed. In order to study in detail the microstructure orientation an EBSD analysis is conducted in the following subsection.

4.5.3 Material texture

EBSD technique is utilized to study the crystal structure and the preferential orientation of the microstructure for the three specimens: B, CD and EAD. Therefore, a Scanning Emission Electron (SEM) microscope, model: JEOL JSM 7001-F, is used with a field emission electron configuration of 20 kV. The specimens are tilted at 70° and the working distance between the collector and specimen was 10 mm. Different magnifications and step sizes of electron microscope are used to study the grain distribution, grain boundaries and subgrains of the material misrostructure. The average of total EBSD indexation for each specimen was around 70%.

As in XRD, this diffraction technique satisfies also the Bragg equation define as:

$$n \cdot \lambda = 2 \cdot d \cdot \sin\theta, \quad (4.15)$$

where n is an integer, λ is the wavelength, d is the space of the diffraction planes and θ is the angle of the incidence of the electrons on the diffraction plane.

The electron diffraction captured on the phosphor screen for each diffracting plane shows a characteristic Kikuchi bands, which are formed where the regions of enhanced electron intensity intersect the screen. Figure 32 shows that the Kikuchi bands registered from the wire drawn specimens and the Miller indices related to the different band intersections.

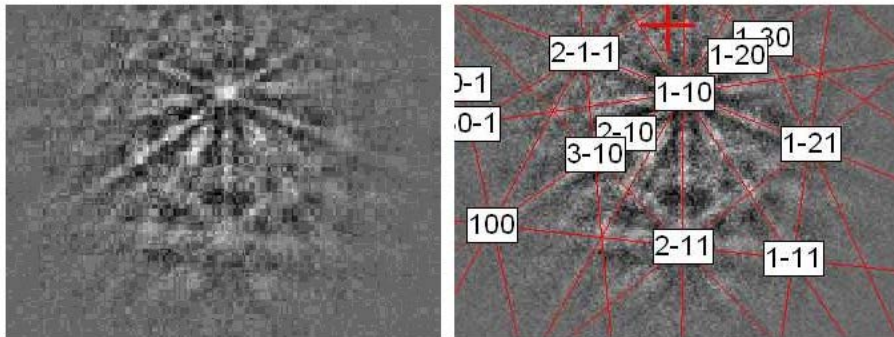


Figure 32: The Kikuchi bands registered during the EBSD with 20 kV field emission electron.

In EBSD the Kikuchi band intensity I_{hkl} of different diffraction angles for the plane (hkl) is described according to the following equation:

$$I_{hkl} = [\sum f_i(\theta) \cdot \cos 2\pi \cdot (hx_i + ky_i + lz_i)]^2 + [\sum f_i(\theta) \cdot \sin 2\pi \cdot (hx_i + ky_i + lz_i)]^2, \quad (4.16)$$

where $f(\theta)$ is the electrons scattering factor, (x_i, y_i, z_i) are the fractional coordinates in the unit cell for atom i and (hkl) are the three index to define the lattice plane.

A large microstructure information can be withdrawn from the registered Kikuchi bands, for example the crystal symmetry of the phases, the preferential crystal orientation, the grain boundaries formation, twin distribution, etc. First of all, in order to compare the different specimen the Figure 33 shows the microstructure of each specimen, where it is distinguished the grain boundaries and twins. Then, Figure 34 exhibits the low-angle grain boundaries distribution within the grain. The misorientation configuration defines high-angle grain boundaries (black lines) and low-angle grain boundaries (while lines) and was set up to 15° and 2° respectively.

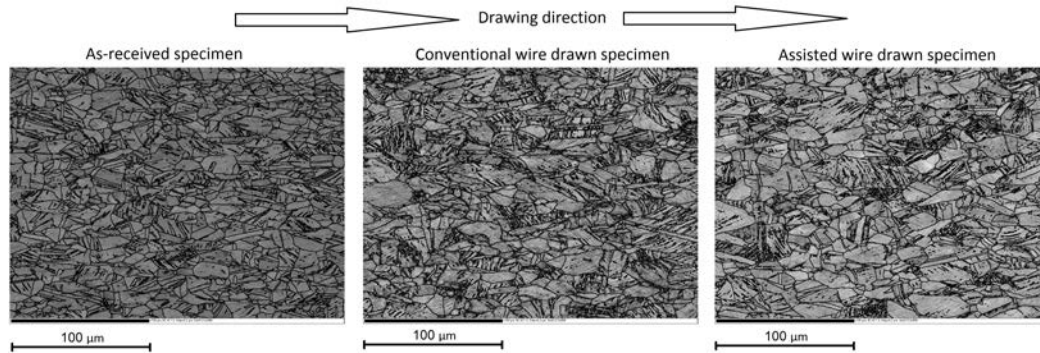


Figure 33: Grain boundaries and twins.

In all cases the microstructure shows a great number of twins, these twins and the curved grain boundaries indicate that the material microstructure is considerable deformed. The conventional wire drawn specimen presents a higher density of twins compare with respect to the electrically assisted specimen. The decrease of twins density demonstrates that a detwinning process occurs when electropulses are induced *in situ* to the wire drawn specimen. Similar detwinning process was found by Xie et al. (2015) [57] when magnesium alloy sheets were electrically assisted after a V-bending process. Nevertheless, in the grain substructure is found that conventional drawn specimen presents higher density of low-angle grain boundaries within the grain compare with respect to the assisted specimen. The low-angle grain boundaries distribution in the conventional specimen tends to orientate in a regular cross mesh, while in the assisted specimen the mesh tends to orientate in parallel. In the second case, the electropulses influence has affected the low-angle grain boundaries distribution, forcing them to orientate along the direction of the drift electron which in this case it is the same than the drawing direction.

In order to quantitatively compare the microstructures, it has been followed the Standard Test Methods for Determining Average Grain Size ASTM E112-13 to do all the grain size

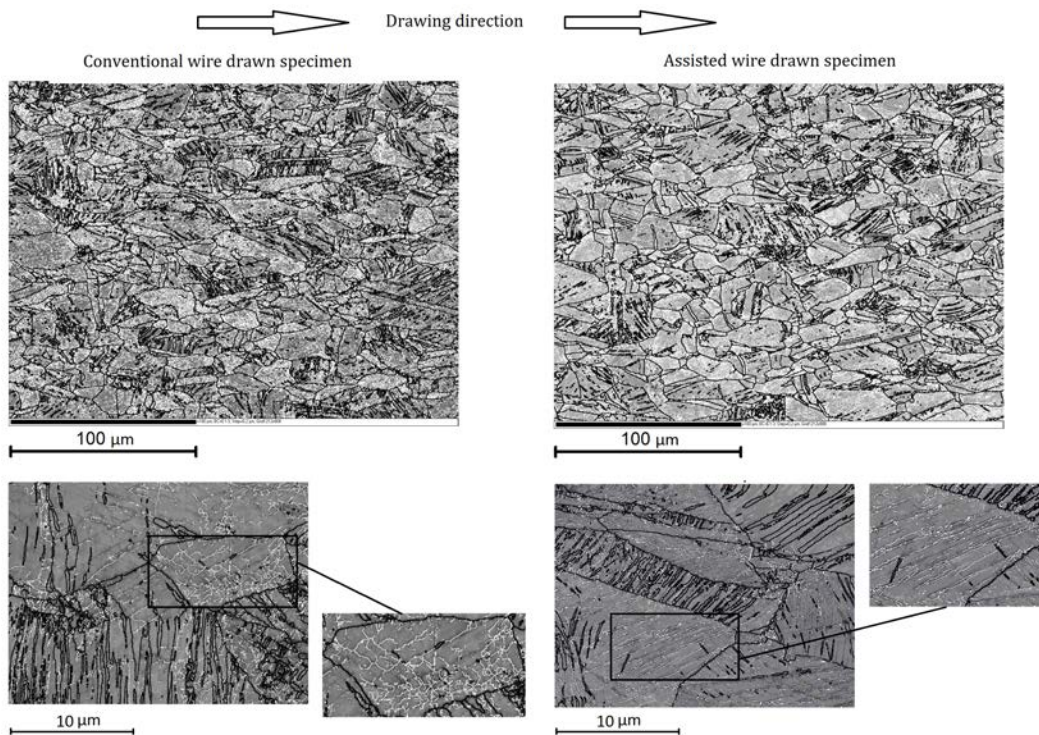


Figure 34: High-angle grain boundaries and low-angle grain boundaries distribution.

measurements. First, it is measured the grain size and area of the microstructure of each wire drawn specimen. Then, it is measured the ratio grain size between the vertical and horizontal directions, to outline the grain anisotropy. Later, the ratios are compared between the different specimens to see the grain size variation depending on the manufacturing configuration used compare with respect the as-received specimen. All these measured parameters are listed in Table 15. The as-received specimen is used as a reference to compare the other two specimens in order to calculate the grain size and area ratios.

Table 15: Grain dimensions and area measure in the three specimens.

Parameter	As-received	Conventional	Assisted
Horiz. diameter d_h [μm]	8.06	8.85	10.8
Vert. diameter d_v [μm]	13.58	12.42	19.2
Grain anisotropy [d_v / d_h]	1.68	1.40	1.78
Grain size ratio	1	0.84	1.06
Grain area [μm^2]	200	181.8	243.9
Grain area ratio	1	0.9	1.22

The grain measurements prove that grain size increase in the EAD specimen compared with respect the CD specimen. The grain dimension of the EAD specimen is 18% larger in horizontal direction and 35% larger in the longitudinal direction. It is also seen that all the specimens present the same grain anisotropy, where the vertical dimension is bigger than

the horizontal dimension. The grain area is around 32% bigger than grain area of the CD specimen. Therefore, the results bring to a conclusion that a DRX was achieved during the wire drawing process assisted with electropulses. This could be possible because the dislocations mobility increase with the temperature and the drifting electrons. The rearrangement of excess dislocations into low-angle grain boundaries leads to the formation of subgrains. After that, the increase of the subgrain size occurs when low-angle boundaries recruit more dislocations while growing.

After measure the grain sizes, it is studied the microstructure orientation. In Figure 35 the Inverse Pole Figure (IPF) of the FCC structure of each specimen are presented. The IPF reveals information of the orientations of specific crystallographic planes. A color palette is also presented to define the microstructure orientation in function of the crystallographic directions $[001]$, $[101]$ and $[111]$, which are parallel to the projection of the IPF (normal direction).

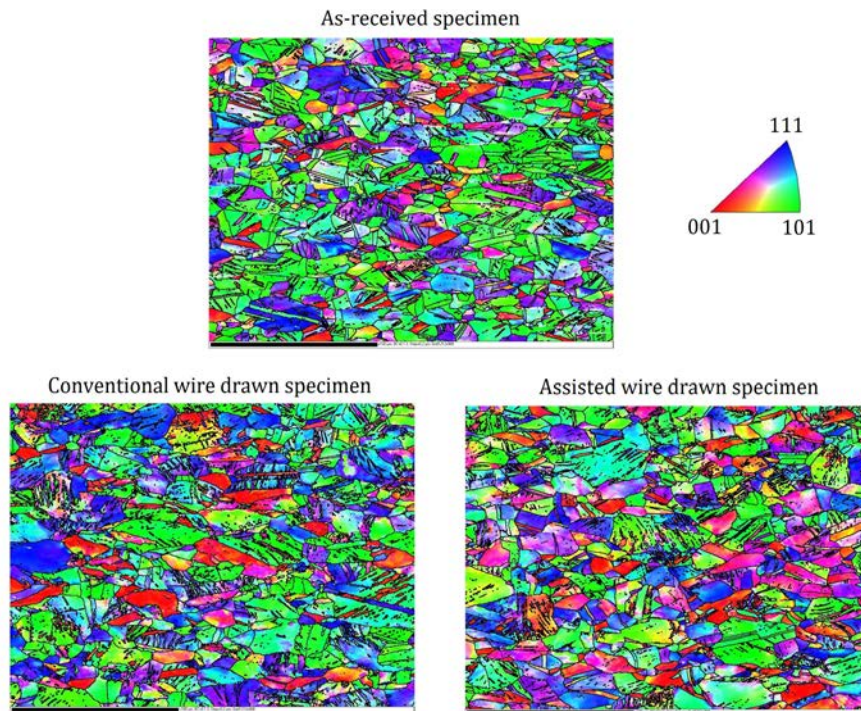


Figure 35: Surface normal-projected inverse pole figure microstructure mapping.

The IPF results present a clear preferential orientation due to a significant number of grains which are orientated close to $[101]$ along the drawing direction, as it is expected for a wire drawing process. The green/turquoise colours represent these points with the $[101]$ parallel to the drawing direction. In order to compare the IPF intensity and preferred orientation distribution between each specimen, the scattering values contribution of the IPF is presented in Figure 36 for each specimen.

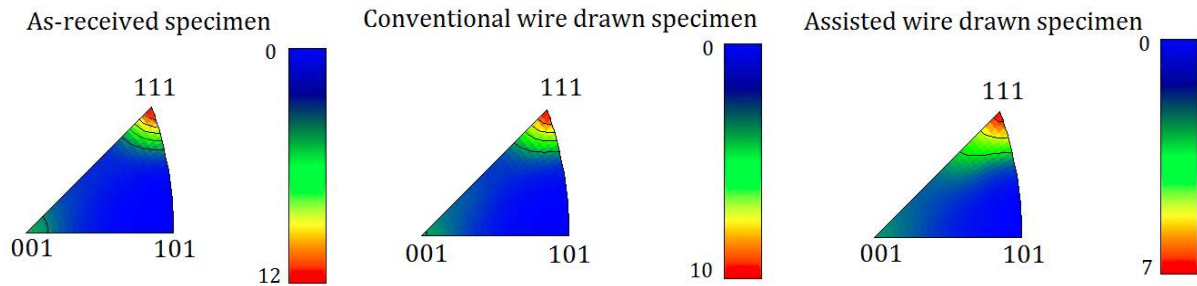


Figure 36: IPF scattering contribution of B, CD and EAD specimens.

The B material microstructure exhibits the highest intensity of preferred orientation towards the direction of $[111]$, as shown in Figure 36. After 16% cross sectional area reduction, the crystal orientation have not change for the CD and EAD specimens, but the intensities decrease compared with the B specimen. Additionally, for the EAD specimen the IPF distribution tends to rotate from $[111]$ to $[001]$. However, in all cases the IPFs prove that the specimens have a surface parallel texture, which meaning there is a strongly preferred orientation towards the primary texture peak $[111]$.

The stereographic projection of the pole figures for each specimen is represented in Figures 37, 38 and 39, where it is displayed the orientations of highest probability for each specific Miller indices of planes. The pole figures reveal information about the texture within a given phase.

The pole figures are shown for the preferential diffracted Miller indices (111) , (200) , (220) , (311) , (222) , (400) , (331) and (420) . The (111) and (222) indices have the higher densities oriented along the X axis. Then, it could ensure that for these two planes the crystals are oriented parallel to the wire drawing direction. A preferential orientation, material texture to (111) , is also observed in the IPF results which corroborates that the preferred crystal orientated is along the wire drawing direction. The scale orientation density depends on the studied specimen. The B and CD specimens show high densities values compare with respect the EAD specimen. It is also analyzed that the CD specimen has a better pattern definition of the crystal orientation, while the EAD specimen the color pattern definition of the crystal orientation is blurred.

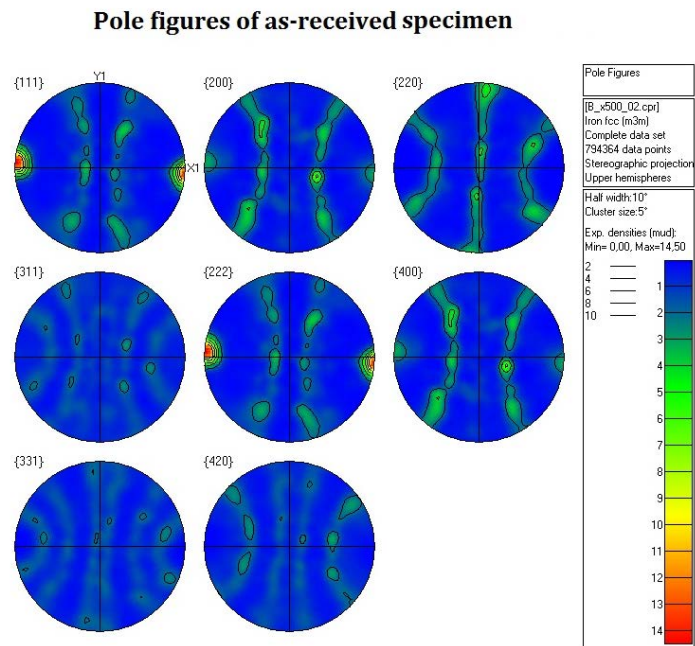


Figure 37: Pole figure of as-received specimen.

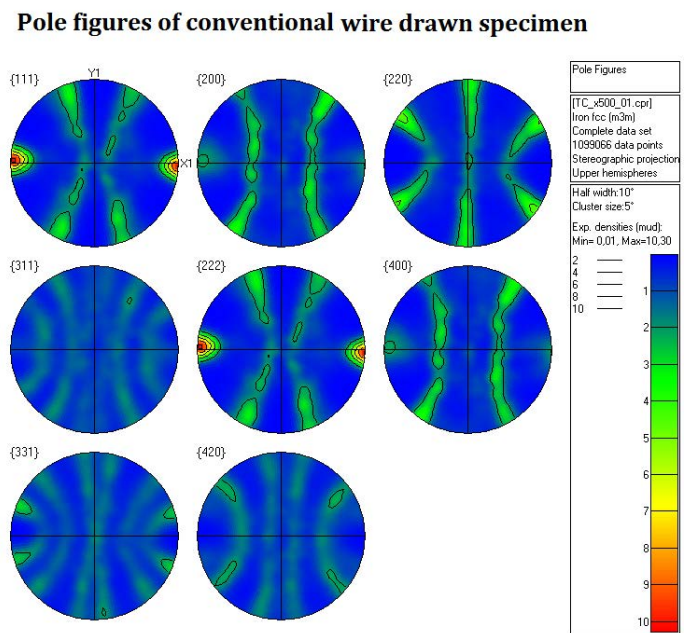


Figure 38: Pole figure of conventional wire drawn specimen.

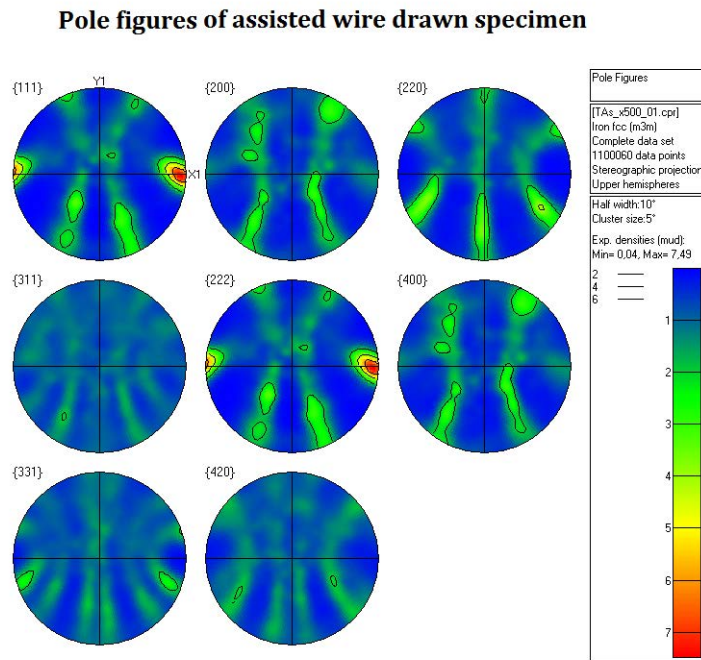


Figure 39: Pole figure of electrically assisted wire drawn specimen.

Finally, an Orientation Distribution Function (ODF) analysis was carried out to study the preferential microstructure orientation for each specimen. In order to understand the ODFs orientation, Figure 40 defines the 3D diffracted region representations with respect to the three Euler angles (ϕ_1 , Φ and ϕ_2). These Euler angles describe the orientation of a crystal forming and reveal the compound textures of the microstructure.

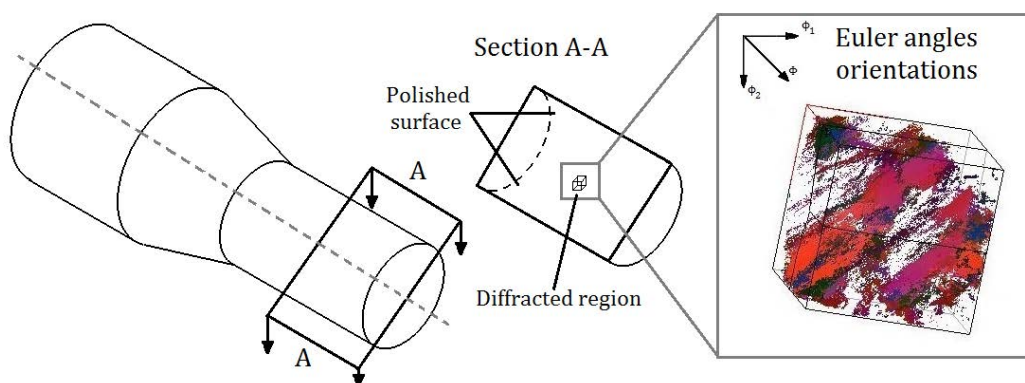


Figure 40: 3D diffracted region representations with respect to the three Euler angles.

In Figures 41, 42 and 43 the crystallographic orientation of each specimen are revealed. The spatial distribution of the texture is observed to be similar in the three specimens. The ODFs show the strongest texture in the $\phi_1 - \phi_2$ plane when Φ is within the range of 55° to 80° . Additionally, in the $\Phi - \phi_1$ plane case the strongest texture is observed when ϕ_2 is within the ranges of 15° to 35° and 60° to 75° . Despite the fact that the ODF of the

CD specimen presents stronger texture for each spatial distribution compare with respect the other two specimens, although in the B specimen is registered the maximum texture intensity 15.5. The OFD of the EAD specimen reveals a weaker material texture, where less contours lines and blurred color define a less compact crystal orientation. In this case the maximum texture intensity toward the preferred orientation is found to be 8. This weaker texture could be explained by the fast rise of temperature registered during the assisted drawing process. This high-rate rise of temperature caused a thermal expansion which could have released the material internal stresses, which come from previous and post wire drawing processes.

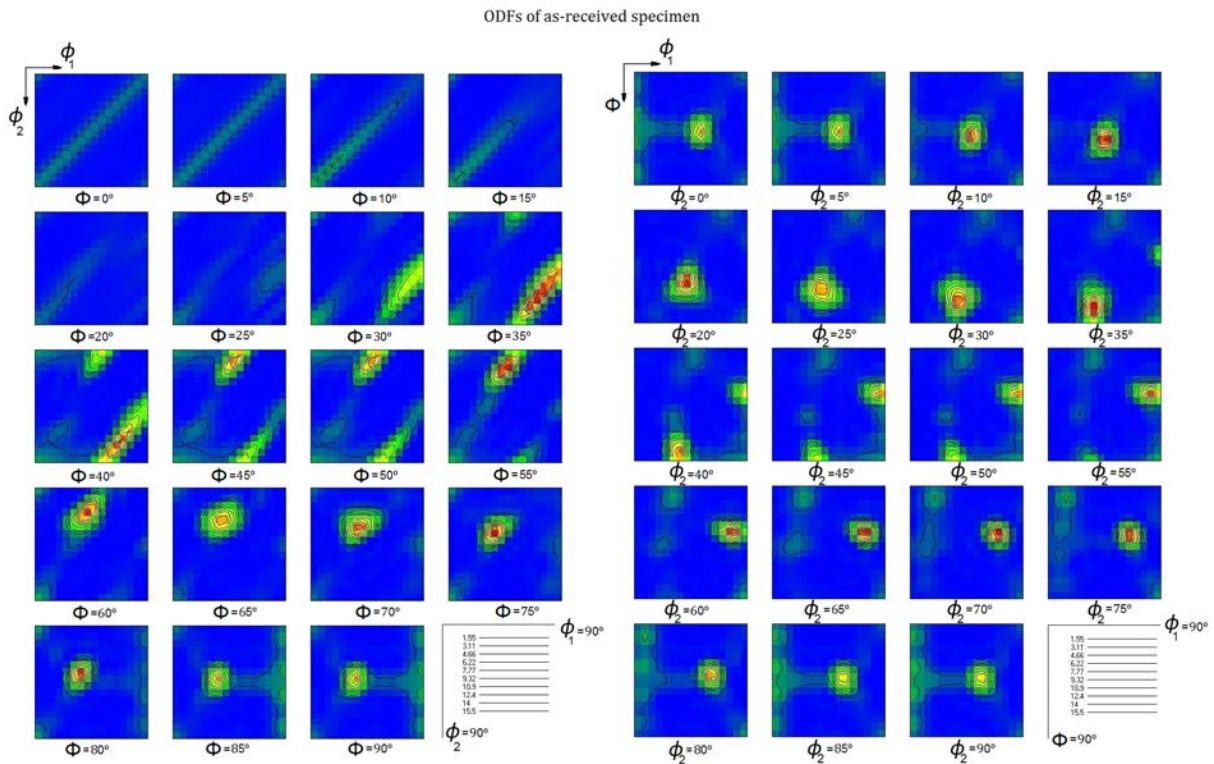


Figure 41: ODFs of as-received specimen.

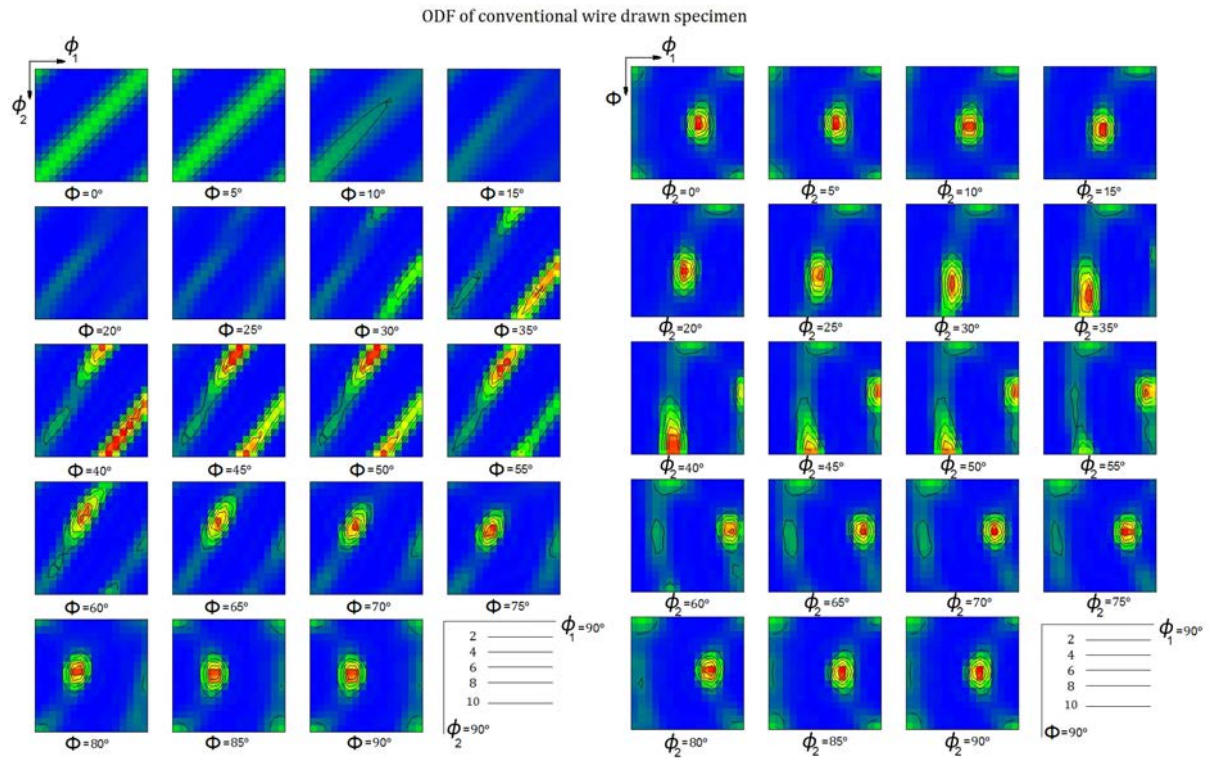


Figure 42: ODFs of conventional wire drawn specimen..

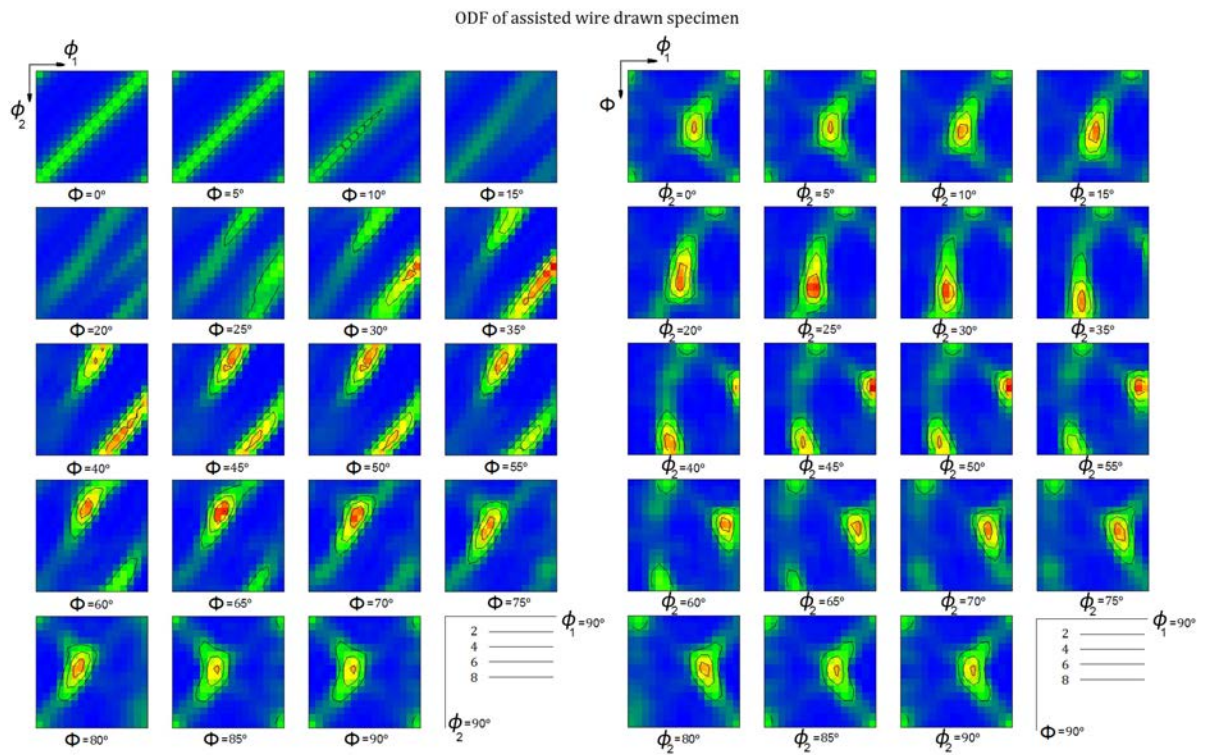


Figure 43: ODFs of electrically assisted wire drawn specimen.

4.6 Conclusions

Electrically assisted wire drawing process has been proved to be a feasible technique which enhances the material formability compared with the conventional wire drawing process.

The results reveal that the wire drawing forces were reduced when the wire drawing process was electrically assisted. The combination of frequency and pulse duration while the electrical output power remains constant seems to have an influence on decreasing the drawing forces. In particular, larger pulse duration and lower frequency discharge configurations seem to have a greater influence on decreasing the needed force to plastically deform the material.

The mechanical behavior of the assisted specimens change compared with respect to the conventional specimens by decreasing the ultimate tensile strength and the yield strength while increasing the material elongation, independently of the pulse duration and frequency configuration used.

The electrically assisted wire drawing process alters the metallography structure in following manners: decreasing the material hardness, altering the volume fraction of austenite and martensite and changing the material microstructure organization. The XRD and EBSD techniques have proved that the volume fraction of α martensite decrease, the low-angle grain boundaries density decrease, a detwinning process is achieved and the grain size increase when the wire drawn specimen was assisted *in situ* with electropulses.

Chapter 5

General Discussions

The following chapter is a discussion of the limitations upon the work and results in this thesis. The work presented in this thesis exhibits the initial stages of experimentation with electroplusing as a technique to assist different manufacturing processes. A major point to focus on the quantifying of the results as a function of electropulses configurations, in order to better determine the mechanism by which formability or machinability is improved. By showing that current density exhibits the current threshold effect seen in Chapter 2, pulse duration and frequency discharge are important parameters to take into account for improving the formability, machinability, manufacturing efficiency and surface properties.

In general, the discussion points can be listed in thermal behavior, electric material resistivity, electroplastic threshold, cutting tool and metallographic observation.

5.1 Thermal behavior

Throughout the processes performed along the thesis temperature measurements were taken when the processes were electrically assisted by electropulses. Bulk temperature measurements were taken using different infrared cameras focusing on the spot where the cathode and anode close the electrical circuit. Due to the high infrared reflectivity temperature measurements were observed not to be accurate. Figure 44 shows a thermal image of the tool and the turned specimens studied in Chapter 3.

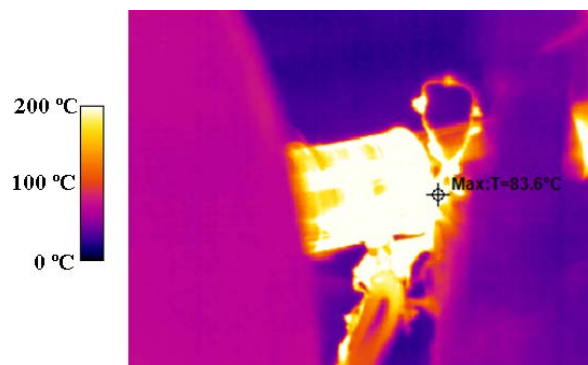


Figure 44: Infrared image of an electrically assisted round turning process.

To register more accurate thermal results, type k thermocouples were used in the wire drawing process studied in Chapter 4. Experiments were performed at 312 A, using a wire diameter of 1.60 mm. The thermocouples were attached to the underside of the drawing die, the temperatures recorded may not necessarily be representative of the temperatures in the forming zone. The results found suggest that the final bulk temperature is similar to all the electropulses configurations. However, the wire drawing forces present lower values depending on the configuration used, the biggest drawing force drop occurred when a combination of higher pulse duration and smaller frequency was used. Then, the electropulses induced a mechanical variation in the wire specimen similar to the annealing process. A study that could be addressed in future is to analyze the mechanical variation when electropulses are used compare with respect standard heat treatment reaching the same bulk temperature. To do that, a material hardness distribution needs to be observed in both methods to determine if the same hardness trend is registered along the radial coordinate. In Chapter 4, it is analyzed that electrically assisted wire drawn specimens performed in a different manner than the as-received and conventional wires drawn specimens.

In Chapter 4, a first thermal balance approach is achieved to determine the thermal contribution when short electropulses are inducted in 308L stainless steel. Therefore, the heat balance for this case is expressed as follow:

$$Q_J - Q_p = \forall \cdot \rho \cdot C_p \cdot \Delta T, \quad (5.1)$$

where Q_J is the thermal contribution caused by the Joule effect, Q_p is the thermal dissipation, \forall is the specimen volume, ρ is the density, C_p is the specific heat constant pressure and ΔT is the temperature difference.

Two different thermal approximations are analysed, first an adiabatic approximation and later a natural convection dissipation expression is considered in the heat balance.

1- Adiabatic approximation:

This first approximation does not take into account thermal dissipation, therefore the second term Q_p is neglected. Then, to estimate this first thermal approximation, it is necessary to find the thermal contribution caused by Joule effect. This term can be estimated by an electric analogy written as:

$$Q_J = V \cdot I = I^2 \cdot R, \quad (5.2)$$

where V is the voltage measured in both wire specimen ends, I is the current intensity through the wire specimen and R is the material electric resistance.

The thermal contribution caused by Joule effect due to the induced electric pulsating field is described as:

$$Q_J = I^2 \cdot R \cdot D \cdot f, \quad (5.3)$$

where D is the current pulse duration and f is the current pulse frequency discharge.

On the other hand, from a thermodynamic point of view the quantity of thermal energy that can be transfer to its boundary is estimated as:

$$Q = \forall \cdot \rho \cdot C_p \cdot \Delta T, \quad (5.4)$$

where Q is the internal thermal variation of the specimen, \forall is the specimen volume and ρ is the density.

Comparing the thermal contribution induced by the Joule effect and the internal thermal variation of the specimen, the following expression is obtained:

$$\forall \cdot \rho \cdot C_p \cdot \Delta T = I^2 \cdot R \cdot D \cdot f. \quad (5.5)$$

The thermal expansion when short current pulses is induced can be written as:

$$\Delta T = (\rho \cdot C_p)^{-1} \cdot I^2 \cdot \frac{R}{\forall} \cdot D \cdot f. \quad (5.6)$$

Assuming that the cross sectional area is constant along the specimen the above equation can be modified as follow:

$$\Delta T = (\rho \cdot C_p)^{-1} \cdot \left(\frac{I}{A}\right)^2 \cdot \gamma \cdot D \cdot f, \quad (5.7)$$

where A is the cross sectional area and $\gamma = \frac{R \cdot A}{L}$ is the material resistivity.

In Table 16 are listed the electric properties to estimate the Joule effect thermal expansion for an adiabatic condition of a 308L stainless steel.

Table 16: Electric properties of a 308L stainless steel.

Steel density [ρ]	8000 Kg/m ³
Specific heat [C_p]	500 J/(Kg · °C)
Resistivity [γ]	7.2 · 10 ⁻⁷ Ω · m

The thermal dissipation by natural convection estimated in a wire 308L stainless steel for an adiabatic condition represents 216 °C. It is necessary to consider that the estimated temperature is for an instantaneous time.

2- Natural convection dissipation approximation:

During the wire drawing process the specimens were not cooled down with any forced convection device. Therefore, in this second approximation a natural convection dissipation is take into account, while the conduction and radiation are considered neglected. Then, from the heat balance equation, it is only necessary to determine the thermal dissipation by natural convection. The equation for convection dissipation is written as:

$$Q_p = h \cdot S \cdot \Delta T, \quad (5.8)$$

where h is the heat transfer coefficient and S is the heat transfer surface area.

Therefore the heat transfer balance equation can be written as:

$$\forall \cdot \rho \cdot C_p \cdot \Delta T = I^2 \cdot R \cdot D \cdot f - h \cdot S \cdot \Delta T. \quad (5.9)$$

As ΔT is assumed to be similar in both terms, the expression can be simplified as:

$$\Delta T \cdot [\forall \cdot \rho \cdot C_p + h \cdot S] = I^2 \cdot R \cdot D \cdot f. \quad (5.10)$$

Then,

$$\Delta T = (\forall \cdot \rho \cdot C_p + h \cdot S)^{-1} \cdot I^2 \cdot R \cdot D \cdot f. \quad (5.11)$$

If the volume \forall is divided in the right hand side of the equation,

$$\Delta T = (\rho \cdot C_p + h \cdot \frac{S}{\forall})^{-1} \cdot I^2 \cdot \frac{R}{\forall} \cdot D \cdot f. \quad (5.12)$$

By assuming that the cross sectional area is constant along the specimen, the expression is simplified as:

$$\Delta T = (\rho \cdot C_p + h \cdot \frac{S}{A \cdot L})^{-1} \cdot \left(\frac{I}{A}\right)^2 \cdot \gamma \cdot D \cdot f, \quad (5.13)$$

where A is the specimen cross sectional area and L is the specimen length.

Then the equation can be reduced to the form,

$$\Delta T = (\rho \cdot C_p + h \cdot \frac{4}{D \cdot L})^{-1} \cdot \left(\frac{I}{A}\right)^2 \cdot \gamma \cdot D \cdot f, \quad (5.14)$$

where D is the specimen diameter.

Therefore, it is only necessary to determine a dimensionless natural convection correlation to estimate the natural convection heat transfer coefficient. These correlations take the form,

$$Nu = C \cdot (Gr \cdot Pr)^n = C \cdot Ra^n, \quad (5.15)$$

or

$$\frac{h \cdot L}{k} = C \cdot \left(\frac{g_r \cdot \beta \cdot C_p \cdot \Delta T \cdot L^3}{\gamma^2} \cdot \frac{\mu}{C_p \cdot k}\right)^n, \quad (5.16)$$

where g_r is the gravitational acceleration, Gr is the Grashof number, k is the thermal conductivity of air, C_p specific heat of air, Nu is the Nusselt number, Pr is the Prandtl number, Ra is the Rayleigh number, B is the coefficient of thermal expansion of air, ρ is the air density, γ is the cinematic viscosity of air, μ is the dynamic viscosity of air, C and n are constant depend upon the orientation of the heated surface.

The thermal properties of air are found in any basic literature of heat transfer, like Incropera and DeWitt (1985) [67]. The values of air properties is estimated from the temperatures difference, which is defined as the average of the surface temperature and the environment

air temperature. Base on a surface specimen temperature is known to be 290 °C, the environment temperature during the experiments was 20 °C the thermal air properties at 160 °C and 1 bar of pressure are listed in the Table 17.

Table 17: Thermal properties of the air at 160 °C and 1 bar.

Gravitational acceleration [g_r]	9.8 m/s^2
Thermal conductivity of air [k]	0.037 $W/m^{\circ}C$
Wire length [L]	1,5 m
Prandtl number [Pr]	0.683
Air thermal expansion coefficient [B]	$3.66 \cdot 10^{-3} 1/^{\circ}C$
Specific heat [C_p]	1.022 $KJ/(Kg \cdot K)$
Air dynamic viscosity [μ]	$30.1 \cdot 10^{-6} m^2/s$
Air cinematic viscosity [γ]	$31.7 \cdot 10^{-6} m^2/s$
Constants [C, n]	0.10 and 1/3 respectively

Using these thermal properties the heat transfer coefficient can be calculate as:

$$Nu = C \cdot Ra^n = 0.1 \cdot (2.3 \cdot 10^{10})^{1/3} = 284. \quad (5.17)$$

Then,

$$\frac{h \cdot L}{k} = 284; \quad h = \frac{284 \cdot k}{L} = 7 W/m^2^{\circ}C. \quad (5.18)$$

Finally,

$$Q_p = h \cdot \pi \cdot D \cdot L \cdot \Delta T = 9 W. \quad (5.19)$$

The thermal dissipation by natural convection represents just near the 1% (9 W) of the thermal heat dissipation induced by Joule effect (800 W). Therefore, if thermal expansion variation is calculated by taking into account the natural convention dissipation, the result is represented as follow:

$$\Delta T = (\rho \cdot C_p + h \cdot \frac{4}{D \cdot l})^{-1} \cdot \left(\frac{I}{A}\right)^2 \cdot \gamma \cdot D \cdot f. \quad (5.20)$$

The thermal dissipation by natural convection for a 308L stainless steel represents 3 °C approximately, the thermal expansion of the Joule effect for an adiabatic condition was 216 °C approximately. Therefore, it can be concluded that the thermal dissipation by natural convection can be neglected.

5.2 Electric material resistivity

Several metallic materials were performed to evaluate the mechanical response to applied current. These results were published without studying whether the resistivity of each material could be affected by the electropulses influence. It is well known that the stainless steel

has a much higher resistivity than the aluminium. Therefore, the bulk temperature of the steel should be higher than the one observed in aluminium, even for lower current densities. However, in Chapter 2, it was found that despite both studied materials show similar bulk temperatures, their mechanical behaviors are different. It is assumed that athermal effects were useful to improve the aluminium formability, while any change was registered for the steel until significant current densities were used. Zhang et al. (2002) [25] explained those changes by a modification of the crystalline defects distribution that subsequently change the material electrical resistivity. In Chapter 4, it is showed an increase of α martensite in the material microstructure, Then, it is expected to find different material electrical resistivity when the specimen is assisted with electropulses. Therefore, further studies need to be done on the material resistivity before and after the experimentation with electropulsing, in order to analyze how the material electric properties are affected.

5.3 Electroplastic threshold

From the experiments carried out in this thesis, it is shown that all the tested materials exhibit a threshold current density, which is different for each material. At densities below their specific threshold, the stresses required to have plastic deformation, at a given strain, are relatively constant, independently of the current density. However, above this threshold, the stress at a given strain is decreased as the current density increased. Perkins et al. (2007) [37] proved a electroplastic threshold existence which depends on the material when a compression test was done. Each material has a current density threshold to initiate improvements in workability, and minor current density changes could reveal significant altered results.

In Chapter 2, it is discussed the electroplastic threshold found in our experiments, where the current density and the pulse duration combinations begin to show improvements in material formability. In addition the results present clear trends showing the improved formability via reducing the relative force, see Figure 45. The conducted research seem to shows that further reductions of bending forces could be registered if higher current pulses amplitudes are used. Therefore for future research, it may be interesting to see if even higher current densities improve the formability and what is the associate influence of the electroplastic thermal effect.

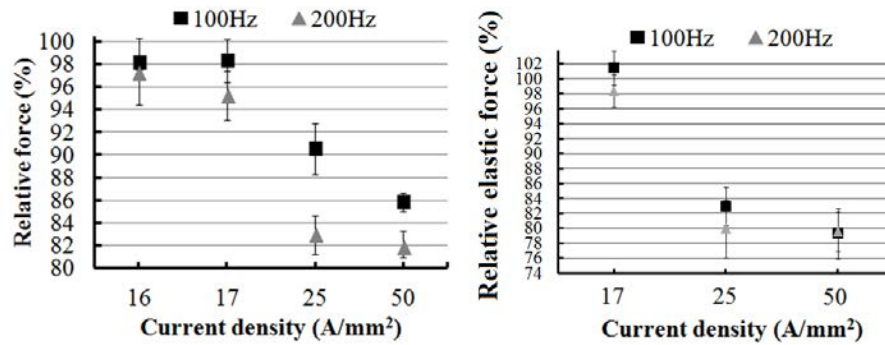


Figure 45: Aluminium bending forces and elastic recovery forces. It is seen that the bending force drops when is applied a certain values of current density. That force drops affected by the current density varies from one material to another. In this case a current density of 25 A/mm^2 reduces by 14% the necessary force to bend aluminium. While the elastic restoring force is significantly reduced, about 20% on average

5.4 Cutting tool

In Chapter 3, it is discussed the adversely effects like built up edge and built up layer that can deteriorate the material surface roughness. During the electroplastic cutting research has used several cutting tools have been used. Although the degradation study of the cutting tool was out of scope, during electrically assisted round turning process no significant degradation of the tools was observed. However, this topic it is expected to be conducted in future work.

In general, two mechanisms are responsible for the tool degradation. The first one is the material deposition on the tool, which could be achieved by two different effects: a built up edge (BUE) or a built up layer (BUL), both mechanisms studied by Khidhir and Mohamed (2010) [45] and Gokkaya (2010) [49], see Fig. 46. The second mechanism is the shape deformation or cracking of the tool. In advance, a current field is expected to increase the tool degradation due to higher thermal values and metallographic alteration. In particular, higher values of temperature predict to find an increase of material deposition on the cutting tool. From this future study, it could be found the ideal cutting tool for electroplastic cutting processes. This tool would need to ensure continuous contact and the lowest change of yield strength under applied electric current.

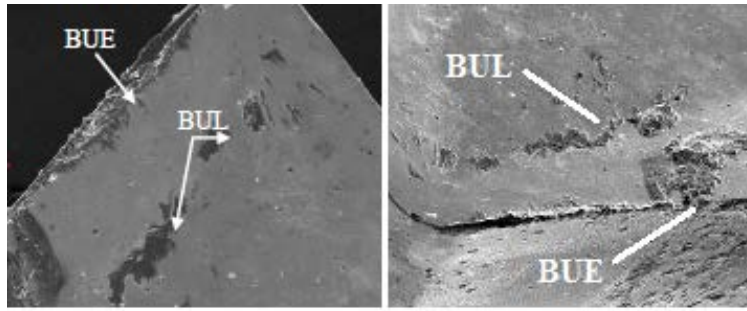


Figure 46: SEM images of BUE and BUL in machined AA2014 (T4) alloy [49].

5.5 Material characterization

Microstructure observation

In Chapter 4, it is studied the influence of the applied electropulses on the microstructural level during wire drawing process. Three different specimens, as-received, conventional wire drawn and assisted wire drawn, were polished manually. Later, an electrolytic etching with oxalic acid was done to observe the material microstructure. In addition, during the polishing and etching process, it is necessary to consider that an excessive chemical component or mechanical process may cause pitting. Figure 47 shows defects on the surface of 308L alloy etched with H_2S , these effects are a combination of a pitting effect and lack of cleanliness from previous etching process. The pitting effect is observed due to an excessive polishing treatment. Generally, this surface defects appear at the last polishing stages due to the polishing velocity, the corrosion from released gases arising from plastic resins and the last polishing stage abrasive disk which are made of a hairy disk. However, the pitting effect can be prevented by changing the etching technique or changing the polishing mechanism: spindle velocity, time and applied force are critical factors to avoid pitting effect.

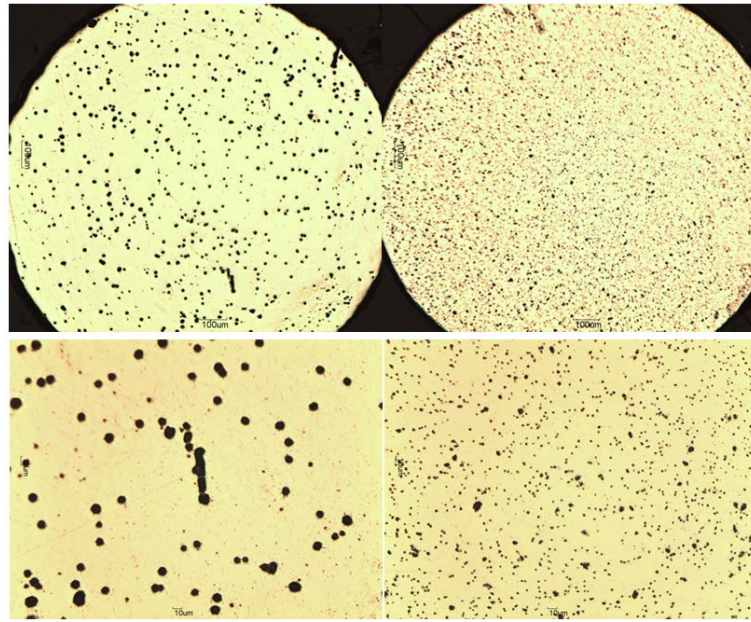


Figure 47: Surface defects on the 308L stainless steel.

Accordingly to basic literature, as Vander Voort (2004) [63], the geometric shape of the pits depends on the crystallographic orientation of the examined grain or crystal. The acid first attacks local defects, such as dislocations, vacancies, inclusions, or impurities. Etching errors may also lead to microstructural misinterpretation. A special care must be taken to avoid interpolation mistakes, for example precipitates from etching or washing solutions could be interpreted as additional phases. Therefore, a metallographic electrolytic polishing and etching was conducted to avoid the aforementioned problems. The etching was achieved with an oxalic acid, as described in ASM Metal Handbook [63]. Figure 48 shows the material microstructure for the as-received, conventional drawn and electrically assisted drawn specimens.

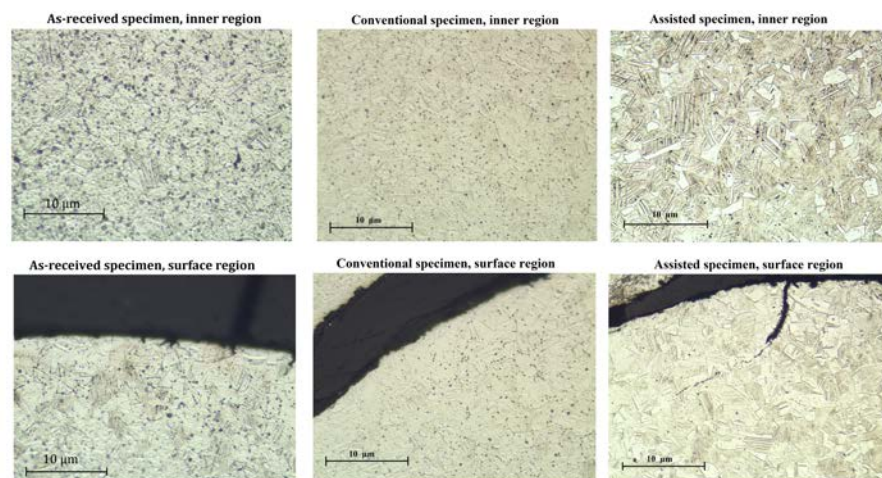


Figure 48: Etched microstructure of as-received (left column), conventional wire drawn (middle column) and electrical-assisted wire drawn (right column) specimens.

Despite that the electropulses have helped to decrease the needed drawing forces to plastically deform the wire specimen, some drawbacks have achieved in the electrically assisted specimens like surface micro cracks and a non uniform surface. As it was comment in Chapter 4, the cracks and the surfaces irregularities could be explained by an excessive surface stress due to the combination of the thermal expansion stresses and the stresses to plastically deform the wire specimen. With the aforementioned two poor surface quality indicators, it can be predicted that the specimens could suffer an early pitting or intragranular corrosion degradation mechanisms and also the specimen fatigue lifespan could be seriously affected. Therefore, these two research topics are open for future works.

From Figure 48, it is proved that electrolytic polishing and etching does not let us determine grain boundaries from twins due to the excessive material deformation. Therefore, further experiments were conducted to measure the grain boundary, material phase transformation and microstructure orientation. To do this, a X-ray diffraction and the Electron Backscatter Diffraction techniques were used to estimate the phase transformations, and subsequently quantify the amount of each phase, grain size and crystallographic orientation for each wire drawn specimen.

Phase determination

A XRD was conducted in Chapter 4 to identify and evaluate the phase transformation induce by the plastic strain in a wire drawing process. Despite that the obtained results clearly shows that electropulsing assisted drawn specimen has a lower presence of α martensite compare with respect to the conventional drawn specimen. In particularly, the XRD patterns reveals that electropulsing inhibit the formation of α martensite because the percentage of volume fraction is two times smaller compare with the non assisted specimen. This change of the volume fraction is explained by two effects which can be couple. From one side, a dynamic recrystallization process which took place at a relative low temperature, as it was also stated Xu et al. (2011) [64]. From the other side, the material thermal expansion has release internal matrix stresses when the material was plastic deformed during the wire drawing process. A contribution of both mentioned effects is probably what brings that percentage of α martensite decrease at least twice in the assisted specimen.

During the drawing process, it is known that the crystallographic system of the material tend to orientate to preferential microstructural orientation, which usually match with the drawing direction. Then, to study the microstructure orientation a EBSD analysis was conducted. The microstructural orientation analysis have withdrew information of the material anisotropy and subsequently its physic properties.

Material texture

EBSD was used in Chapter 4 to analyzed the orientation of microstructure and the material texture. The results showed that similar preferential microstructure orientation is presented for different wire drawn specimens, although a initial stage of misorientation and a

decrease of intensity in the preferred orientation was found in the assisted specimen. On the other hand, the EBSD images were used to estimate the grain dimension ratio, length versus width, and the grain average area. These parameters gave us more information about the evidences of a local dynamic recrystallization process which affected the material microstructure. The microstructure reorientation by the effects of the electropulses has brought two noticeable results: a detwinning process and the distribution and orientation of the low-angle grain boundaries. In spite of decreasing the number of twins, decreasing the low-angle grain boundaries density and orientation these low-angle grain boundaries toward the electron wind direction, the mechanisms which leads to explain those changes need further investigation.

In summery, all the material characterization techniques were used to give an explanation to the mechanical properties variation found in the wire drawing process. The metallographic variations findings can not be only justified by the thermal effect contribution, but also by the electroplastic athermal effects which contributed to improve the material formability and machinability. It is also proved that the electropulsing treatment induce a material thermal expansion. This thermal expansion have an influence on the material internal stresses, which could account as another factor to promote the mechanical properties variation. Nevertheless, further investigation need to be done at an submicron level to understand the mechanisms that modify those metallographic variations when electropulses are induced.

In the following chapter the general conclusions of this thesis are listed and prospects for future work are proposed.

Chapter 6

Conclusions and recommendations for future work

In this chapter conclusions of the work carried out during this thesis will be written. additionally, some prospects and suggestions on future work will be given.

6.1 Conclusions

Base on the research performed in this thesis, the following conclusions are accomplished.

- An electrical insulation system was designed and manufactured for each manufacturing processes. A detailed methodology for recording the desired electrical and mechanical parameters in each manufacturing process was implemented.
- Temperature and thermal expansion, Joule effect, were understood as not the unique determining factors in the mechanical behavior modification. Athermal effects are also found to affect the materials processed when they are assisted by short time high electropulses.
- Three electropulses generators were designed and manufactured in order to assist several manufacturing processes. Those generators are capable of modifying the induced electrical parameters, such as frequency and pulse duration.
- In Chapter 2 the electrical assisted bottom bending process was shown to reduce the bending forces and the elastic recovery forces compared to the conventional process when several metallic materials are bent.
- In Chapter 3 the electrically assisted turning process has been shown to be a feasible technique to improve the material machinability compared with the conventional turning process. The power consumption and the cutting specific energy were reduced under the electropulses presence. The impact is particularly relevant for high frequencies and long pulse duration. However, the different frequency discharge and the pulse duration configurations influence on the surface roughness and material hardness neither present statistically significant differences, nor an obvious trend.

- In Chapter 4 The electrical assisted drawing process enhance the energy efficiency as well as it modifies the material mechanical behavior. The longer duration pulses and lower discharge frequencies combination have the greatest improvement in the material formability.
- In Chapter 4 the material hardness distribution along the cross sectional area presented different trend and magnitude when the conventional specimen was compared with the electrically assisted specimen. In particular, the electrically assisted drawn specimen showed lower values of hardness compares with the conventional drawn specimen. Therefore the electropulses treatment revealed a mechanical variation in the specimen, as it also occurs when annealing treatment is achieved.
- In Chapter 4 the electrically assisted wire drawing process has proved to alter the metallography structure by altering the volume fraction of austenite and martensite and changing the material microstructure organization and orientation. The DRX and EBSD techniques have proved that the amount of α decrease, the low-angle grain boundaries density decrease, a detwinning process is found, while the grain size increase when the wire drawn specimen was assisted *in situ* with electropulses.

6.2 Contribution to research

Through the research presented the following contributions have been achieved. These several research contributions have either been published or are currently under review. The research contributions are listed below:

- Several electropluses generators were designed and manufactured to assist different conventional manufacturing processes.
- Specific tools to isolate each test machine from electricity were achieved.
- A detailed methodology for monitoring the electrical parameters and to study various mechanical and/or metallographic parameters was documented.
- A numerical method to characterize each conventional manufacturing processes was implemented.
- Electropulsing to assist conventional manufacturing process was proved to be a feasible technique which improves either the material formability or the material machinability compared with conventional processes.

All of these results have been published or are under review for publication. The study of the bottom bending process assisted with electropulses is published in Sánchez et al. (2014) [44], and the electrically assisted round turning process is published in Sánchez et al. (2015) [59]. Results regarding the wire drawing processes assisted by electropulsing are currently under review.

6.3 Recommendations for future work

Based on the conclusions that have been made in this research, the following prospects are suggested to be carried out for future work.

a. Current density threshold.

A electroplastic threshold was found in Chapter 2, where the aluminium strips showed a mechanical variation when the process was assisted by different current densities. Further experiments are necessary to investigate when that threshold takes place for the same and different materials. This threshold is assumed to be linked to the athermal electroplastic effects. Only when a certain amount of current density is induced, the athermal effects become effective and modify the material formability and machinability.

b. Tools analysis.

The cutting tools used in Chapter 3 were changed before any adhesion defect or fracture could be achieved, although the interaction between the cutting tool and the specimen was not studied. A potential next stage to this research could be to measure the tribological conditions between the tool and the specimen. It is believed that the electropulses will affect the interaction tool-specimen and no desired effects will appear, like built-up edge, built-up layer, chipping wear and tool fractures. This study could let us measure how the lifespan of the cutting tool is affected and also what is the appropriate tool depending on the machining conditions.

c. Feed rate and induced electric power.

Both mentioned parameters are significant when the electroplasticity phenomenon is under research. In Chapter 4, just the tensile test machine maximum feed rate was studied. The future proposition will be to determine if the manufactured material at industrial drawing velocities, around 5 m/s, could be assisted by the electropulses.

Moreover, a combined frequency and pulse duration was used to induce a maximum electric power of 800 W. Longer pulse duration and lower frequency discharge was shown to reach greater formability improvement compared with higher frequency discharge and shorter pulse duration. A future task could be to design an experimental abacus combining electrical parameters such as frequency, pulse duration, feed rate, current density and electric output power. This would allow to analyse the mechanical and metallographic material behavior.

d. Metallography.

The metallographic observation was studied in Chapter 4 and represents an initial stage of experimentation. Further researches in the metallographic observation of different materials need to be done, when they are assisted by different electrical configurations. It should be also thoroughly investigate if the electropulses can induce phase transformations, detwinning process, decrease the dislocation concentration, modify the grain boundary and/or grain size. This may help to understand at what point the meso-scale thermal effect is predominant in the electroplasticity phenomenon.

A potential next stage to this research could be the measure of internal compressive stresses by a X-ray diffraction technique. The internal stresses are induced on the material due to the thermal expansion caused by the electropulses. In addition, it is assumed that a thoroughly work on the Electron Backscatter Diffraction technique is essential. This will help us to withdraw further results and conclusion to explain the mechanical variations through a metallographic characterization, involving recrystallization, phase transformation, material texture, detwinning, dislocation annihilation and so on so forth.

Appendix A

Electric configuration of a current pulse generator

This appendix explains the electropulses generator electric schema designed and manufactured to assist different industrial manufacturing process. The electropulses generator can be divided into power circuit and trigger pulses circuit. The power circuit design is common to all the generator versions. Although the electric parameters, such as output power, current intensity and voltage, may vary depending on the generator version. Regarding the trigger pulses, circuit operation could be controlled by two different systems: first generator version use a silicon thyristor, whilst the second generator version uses power MOSFETs.

Figure 49 shows the main generator circuit, the power circuit and the trigger pulses circuits are subdivided into several stages, which are explained below.

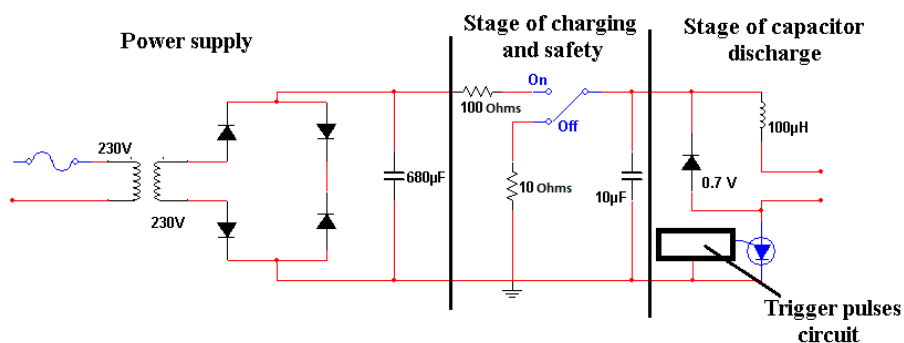


Figure 49: Electric schema of the main electropulse generator.

A.1 Electropulses generator power circuit

The power circuit is common for the three self made generators used. The unique difference among the three generators is the electric parameters magnitudes of the power supply. The power circuit is divided into three stages: power supply, stage of charging and safety and stage of capacitor discharge.

A.1.1 Power supply

The generators will be fed by an isolated transformer. The primary transformer coil is powered with a 230 V, while the secondary transformer coil change the voltage depending on the generator version from 30 to 230 V. The current flow is controlled by a fuse, located just before the entrance to the primary transformer coil. This fuse keeps the circuit energize and, therefore, the trigger capacitor loaded. However, there is no current pulses induction. There is also a Wheatstone bridge, which rectifies the full signal by converting the alternating current (AC) into direct current (DC). For that purpose, a capacitor was added in order to supply a constant voltage of 311 V. Figure 50 shows the capacitor output signal outline.

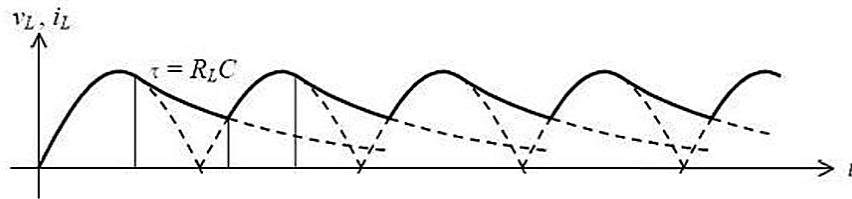


Figure 50: Rectifier system output signal outline.

A.1.2 Stage of charging and safety

This circuit stage is where the capacitor generates the electropulses and is controlled by the safety switch status. The capacitor charge is limited by the 100 Ω s resistance. The value of this resistor determines the capacitor charging speed, what is intended to operate at high frequencies, so the capacitor is needed to be charged and discharged in very short periods of time. Because of this, high temperature is reached at the resistance. For this reason the system needs good thermal dissipation to reduce the thermal effects that may affect the performance.

The safety system has a relay that operates in two positions: ON and OFF. The default setting will be OFF position, which avoids possible short-circuits and possible electrocutions when handling the specimen. While the ON position is the forced operation by two switches, one to maintain constant electropulses and another one to switch ON and OFF electropulses manually.

Figure 51 shows the capacitor output signals, which are the electropulses.

A.1.3 Stage of capacitor discharge

When the safety switch remains ON conducting current intensity, this stage comes into operation. A coil is used as a safety damping component for the electric field coming from the capacitor abrupt discharges. This component allows to extend the pulse duration and to soften the peak current intensity as a function of its inductance. The electropulses damping is essential, otherwise it may damage electronic circuit components such as diodes. The role

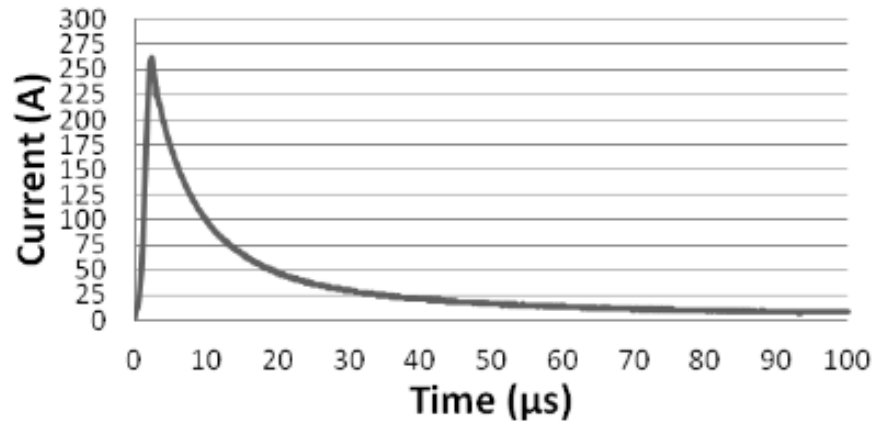


Figure 51: Capacitor output signal: electropulses.

of the diode, set in parallel with the coil and the resistance, will be to avoid that the electrical pulses flow in the opposite direction. If that occurs, the diode cuts the signal entrance and prevents signal spread.

Just before the capacitor output terminals a 0.05Ω resistance is added to facilitate the corresponding current flow direction. It also allows to circulate the maximum current intensity through the specimen. That resistance helps to connect measurement equipments such as an oscilloscope to a multimeter to measure the frequency, pulse duration, current intensity and power consumption.

In this final stage the trigger electropulses circuit operates. The trigger system is detailed in the following section.

A.2 Trigger electropulses circuit

Unlike the power circuit, the trigger circuit shows two different operation systems which characterize two respective electric current generator versions. The first version uses a silicon thyristors and the second one uses a several power MOSFETs. Both versions are explained below.

A.2.1 Electropulses generator with silicon thyristor

Figure 52 shows the trigger circuit schema operated by a silicon thyristor. That circuit is located within the pulse discharge operation stage. It is responsible for controlling the silicon thyristor, which allows the electric pulsing field go through the specimen. It has several stages similar to the previous circuits.

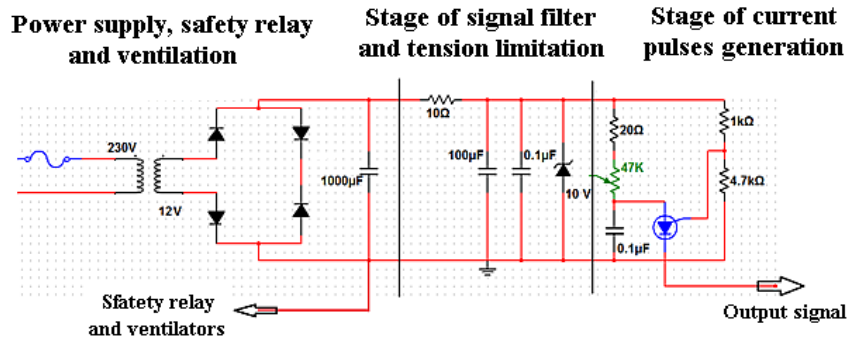


Figure 52: Silicon thyristor trigger electropulses circuit schema.

A.2.2 Power supply, safety relay and ventilation

The power supply stage is analogous to the power circuit one. It has a rectifier system and a capacitor that can induce a constant direct voltage. The main difference of this power supply is the transformer, since the required voltage in the secondary coil is just 12 V and a current intensity of 2 A. The DC voltage is obtained from the rectifier system and it will feed the ventilation system and some others electrical components, as the protection relay to change state from OFF to ON. The output signal of this first stage is similar to that shown earlier in Figure 50, but in this case the maximum voltage is 12 V.

A.2.3 Stage of signal filter and tension limitation

After the rectifier system, the capacitor generates a pulsating signal DC of 12 V. That signal goes to a 10 Ω resistor and two capacitors in parallel, one of 100 μF and another one of 0.1 μF . That electronic component set works as a low pass filter, removing high frequency noise, thereby leaving a signal of 12 V stable and without noise. Two capacitors are needed: an electrolytic condenser and a polyester condenser to ensure optimum filtration of high frequency noise. In this stage, there is also a Zener diode to keep a constant voltage of 10 V. That steady voltage without noise will reduce the false positives when the generator performs with high frequency discharge.

A.2.4 Electropulses generation stage

The trigger circuit last stage is where electropulses are generated. There, the frequency discharge induced to the specimen is also set. Figure 53 shows the oscillator system that controls the current pulses generation which is operated by a silicon thyristor.

The programmable unijunction transistor (PUT) performs base when comparing the branch 3 voltage to branch 2 voltage. If the voltages of both branches are equal, then the transistor becomes conductive. Thus, the branch 3 is connected to the branch 1 in order to allow the capacitor current discharge.

The frequency discharge is regulated by a potentiometer. If the ohmic resistance increases, less current intensity flows and slowly the capacitor is charged, which means a lower electropulse frequency discharge is induced to the specimen. If the ohmic resistance decreases,

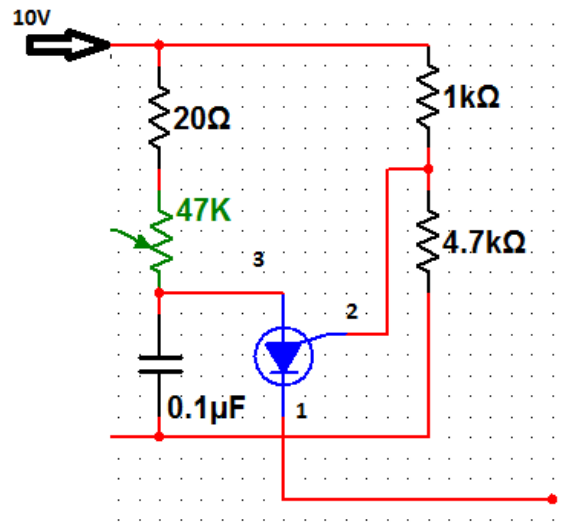


Figure 53: Electropulses generation schema operate by a silicon thyristor.

more current intensity flows and quickly the capacitor is charged. Subsequently, a frequency discharge is induced to the specimen. The circuit was designed to work under frequencies within a range of 75 to 250 Hz, a pulse duration of 50 μs and a current intensity about 300 A.

This generator was used to study the bottom bending process assisted with electropulses. During the experiments, it was observed that the induced pulse duration was an important parameter to take into account for future experiments. Therefore, it was come to a conclusion to manufacture a new electropulses generator controlled by power MOSFETs to be able to vary pulse duration.

A.2.5 Electropulses generator controlled by power MOSFETs

This second generator version not only allows modification of frequency discharge, as it happens for the previous generator version, but it can also modify the pulse duration. The trigger circuit of this second generator version is more complex and involves several stages as detailed below. Figure 54 presents the trigger circuit operated by power MOSFETs.

The trigger system uses astable and monostable timer circuits to control the current pulses frequency discharge and pulse duration. The electropulse features are: 50 to 200 μs pulse duration, 100 to 400 Hz frequency discharge and a maximum current intensity about 300 A.

The trigger circuit controlled by power MOSFETs disposes of the same steps than the trigger circuit controlled by silicon thyristor. The stages of the power supply and ventilation and the signal filter and tension limitation are identical in both generators. Therefore, only the electropulses generation stage differs between both generator versions. All the differences are detailed below.

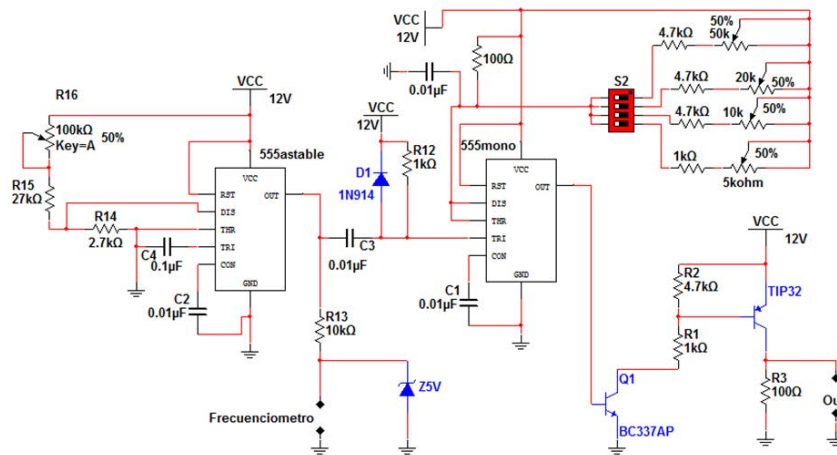


Figure 54: Power MOSFETs trigger electropulses circuit schema.

A.2.6 Electropulses generation stage controlled by power MOSFETs

In this stage the frequency discharge and the pulse duration is defined. The astable oscillator and the potentiometer (R16) determine the frequency discharge. The potentiometer set the frequency range between 100 and 400 Hz. Output terminals are added to measure and set the desired frequency discharge during the experiments with a frequencimeter. Figure 55 shows the generator circuit region and the output terminals to control the frequency discharge.

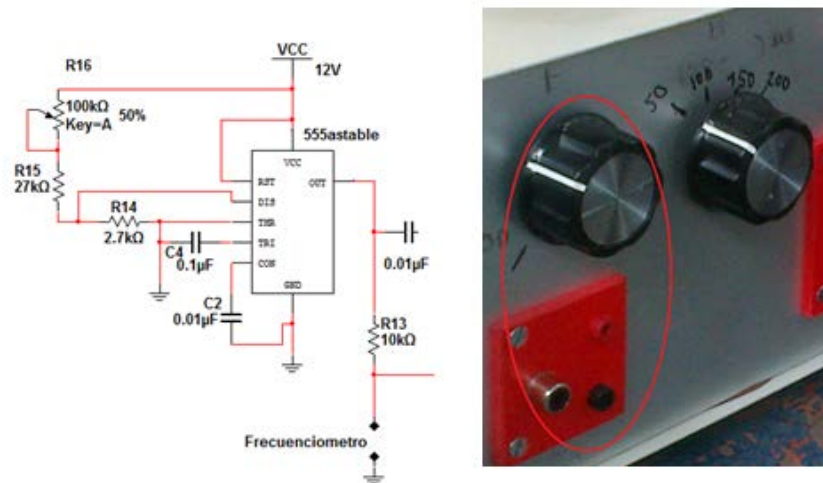


Figure 55: Electronic region and output terminals to control the frequency discharge.

On the right side of Figure 55, it is shown the spinner knob which controls the frequency discharge. At the bottom, it can also be seen the output terminals in red and black colors. These terminals allow to connect a multimeter with frequency counter to set the desired frequency discharge. The left side of Figure 55 shows the potentiometer resistance (R16), which is controlled by the spinner knob.

The other spinner knob modifies the monostable oscillator and commutator (S2) to control the pulse duration. The knob disposes four different statuses, each one connecting a resistor and a potentiometer with different magnitudes. According to the chosen status the pulse duration can be 50, 100, 150 and 200 μs .

Figure 56 shows the exposed generator circuit region and the spinner knob to control the pulses duration.

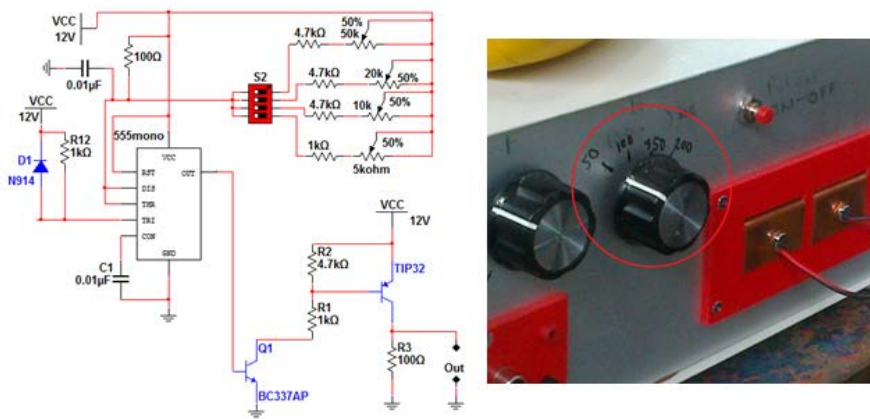


Figure 56: Electronic region and output terminals to control the pulse duration.

On the right side of Figure 56 it is shown that the pulse duration is controlled by a spinner knob, similar to the frequency control. In this case the spinner knob only has four possible positions. The knob is linked to the rotary commutator (S2), as it is presented in the left part of Figure 56. In order to measure the pulse duration *in situ* during experimentation, a specific terminal was added to connect the oscilloscope to monitor the pulses duration and current intensity.

Appendix B

Mechanical formulation

The mechanical formulation used in the bottom bending and wire drawing analysis is based on the one proposed by Celentano et al. (2011) [33]. The governing equations together with the constitutive material and contact-friction models are discretized within the framework of the finite element method, according to the numerical approach detailed by Celentano et al. (2004) [34]. A classical plasticity model has been adopted to describe the material behavior during the bending process in which the von Mises function F is defined as:

$$F = \sqrt{3 \cdot J_2} - \bar{\sigma}, \quad (\text{B.1})$$

where J_2 is the second invariant of the deviatoric part of the stress tensor σ ($\sigma_{eq} = \sqrt{3 \cdot J_2}$ is the so-called equivalent or von Mises stress), and $\bar{\sigma}$ is the flow stress given by the linearization of the Ludwik equation:

$$\bar{\sigma} = \sigma_y + k \cdot \bar{\epsilon} \quad (\text{B.2})$$

where $\bar{\epsilon}$ is the effective plastic strain, k is the parameter which characterizes the isotropic strength behavior of the material and σ_y is the yield strength defining the initial material elastic bound.

Since, in both processes, the values of initial yield strength and ultimate tensile strength approximately fit a linear interpolation within the tensile strain interval of this material, which exhibits a relatively low ductility with a tensile rupture elongation of 6% to 8%, a linear hardening law has been adopted for simplicity. The contact and friction model adopted in this work is based on the frictional-plasticity analogy that has been developed and successfully used in many applications over the last years. The main aspects of this model can be found in Celentano et al. (2011) [33]. The governing equations, together with the material constitutive and contact-friction models, are discretized within the framework of the finite element method according to the numerical approach detailed by Celentano et al. (2004) [34]. The contact model proposed is a simplification of the well known penalty method, which is used for solving constrained optimization problems. Therefore, the contact used here is described with a contact boundary $\Gamma_{f(i)}$ of the spatial configuration of a given body i , with i being the index accounting for the number of bodies that may mechanically interact. This boundary contact can be written as:

$$\Gamma_{f(i)} = -p_n \cdot n_{n(i)},$$

where p_n is the normal contact pressure and $n_{(i)}$ is the $\Gamma_{f(i)}$ outward unit normal vector. Moreover, the normal gap g_n between bodies 1 and 2 is conventionally expressed as $g_n = n_{(1)} \cdot (x_{(1)} - x_{(2)})$, where x is the spatial coordinate vector (as usual, $x = X + u$, with X and u being the material coordinate and displacement vectors, respectively).

Then, the contact model can be described as:

$$p_n = E_n \langle g_n \rangle,$$

where E_n is the normal rigidity aimed at restricting the inter penetration between the contact bodies and $\langle \rangle$ are the Macauley brackets (*i.e.* $\langle x \rangle = x$ if $x > 0$ and $\langle x \rangle = 0$ otherwise).

Therefore, the material constitutive and contact models presented above are discretized within the framework of the finite element method. In particular, the specimens were approached by a two-dimensionally discretized mesh with four noded isoparametric plane stress elements that consider a B-bar interpolation to avoid the numerical locking due to plastic incompressibility. On the one hand, a Coulomb type law with a friction coefficient of 0.10 was used in the punch-sheet and die-sheet interfaces described in the bottom bending process. On the other hand, a Coulomb type law with a friction coefficient of 0.07 was used in the wire-specimen and drawing-die interfaces described in the wire drawing process. The specimen formability was achieved by incrementally imposing a prescribed vertical displacement of the punch in bending and of the wire specimen in drawing. Finally, in Figure 18 there are listed the main characteristics of both finite element simulations.

Table 18: The main characteristics of the bottom bending and wire drawing finite element simulations.

Configuration	Bottom bending	Wire drawing
Mesh type	Bi-dimensional (2D)	
Mesh contact type	Uni-dimensional (1D)	
Element type	Quadrilateral	
N° of node per element	4 nodes (B-bar interpolation)	
N° of contact node	2 nodes (linear interpolation)	
Total nodes	724	2273
Total elements	848	2261
Simulation condition	Plain strain	Axisymmetric
Contact region	Punch-sheet and die-sheet	Wire specimen-drawing die
Accuracy	6 (sheet thickness)	10 (specimen radio)
Imposed steps	1000	550
Computational time	30 mints approx. (1 cpu with 3 GB Ram)	

Appendix C

Electropulses generator quotation

In this appendix there are listed all the electronic components and their prices to manufacture a current pulse generator, as it is shown in Table 19. The electronic component cost can differ due to the fact that the suppliers change their quotation policies.

Table 19: Electronic components list needed for a electropulse generator.

N°	Description	Units	Units price (€)	Total plus VAT (€)
1	Transformer 230/150V-800W	1	264.5	320.05
2	External shell 400x130x300mm	1	107.39	129.94
3	Radiator Fadi	2	5.5	13.31
4	Resistances 100W	6	7.56	54.89
5	Wheels control	2	1.84	4.45
6	Ventilator 12V	1	13.55	16.40
7	Power printed circuit	1	35	90.75
8	Trigger printed circuit	1	15	54.45
9	Mosfet 57A 100V	8	0.6	5.81
10	Rotating commutator	1	2	2.42
11	SemiKron diode	4	7.91	38.28
12	Electrolytic condenser	7	0.78	6.61
13	Potentiometer	2	7.98	19.31
14	Zener diode	1	0.02	0.02
15	Resistance 100H 4W	3	0.81	2.94
16	Resistance 10H 1/4W	4	0.02	0.10
17	Copper wire Φ 6mm x metre	4	3.5	16.94
18	Copper connection terminals	10	0.25	3.03
19	Varistor	1	0.43	1.56
20	Fuse holder	1	0.52	0.63
21	Ceramic circuit board	2	0.98	2.37
22	Female terminals	15	0.09	1.63
23	Female Ariston connection	1	2.99	3.62
24	Male Ariston connection	1	3.13	3.79
25	Electrical connection wire	1	1.84	2.23
26	Professional rotating condenser	1	8.11	19.63
27	Rubber wire holder	2	0.4	0.97
28	Thread system	4	0.09	0.97
29	Rotation BNC male connection	1	1.85	2.24
30	Female BNC adaptor	1	1.43	1.73
31	25 turns potentiometer 10K	1	0.5	0.61
32	25 turns potentiometer 20K	1	0.5	0.61
33	25 turns potentiometer 50K	1	0.5	0.61
34	ON/OFF switch	1	1.76	2.13
35	Toroidal chokes 30A	1	21.04	25.46
	Total		702.41	849.92

* It was applied a 21% of value added tax (VAT).

The design, manufacture and validation personal expenses are listed in Table 20. The estimate engineer salary per hour comes from the Colegio Oficial de Ingenieros Industriales de Álava, Bizkaia, Gipuzkoa y Navarra in 2014. The salary estimation is taken from the free professional exercise section within the Manufacturing Engineering sector.

Table 20: Personal list for manufacturing a current pulse generator.

Personal	Hours	€/hour	Total (VAT inc.)
Electronic Engineer	80	65	5,200
Mechanical Engineer	80	65	5,200
Manufacturing technician	80	32	2,560
Total			12,960

* It was applied a 21% of value added tax (VAT).

The generator final quotation would be around **13,810 €** approximately, including the materials cost, design and manufacturing working hours.

During the thesis 3 different electropulses generators have designed and manufactured, one for each manufacturing process.

Appendix D

Research activities schedule

In this appendix there are listed all the main research activities done along the thesis. All of them are mentioned in Figure 57. These activities are gathered in four phases: bottom bending process, round turning process, wire drawing process and thesis composition.

TASKS	2012												2013												2014												2015						2016																	
	JAN	FEB	MAR	APR	MAY	JUN	JUL	AUG	SET	OCT	NOV	DEC	JAN	FEB	MAR	APR	MAY	JUN	JUL	AUG	SET	OCT	NOV	DEC	JAN	FEB	MAR	APR	MAY	JUN	JUL	AUG	SET	OCT	NOV	DEC	JAN	FEB	MAR	APR	MAY	JUN	JAN	FEB	MAR	APR	MAY	JUN												
1st. PHASE																																																												
Manufacture 1st pulse generator																																																												
Mechanical system to assist the bottom bending process																																																												
Bottom bending assisted process experimentation																																																												
Data processing																																																												
Bottom bending article draft																																																												
2nd. PHASE																																																												
Manufacture 2nd pulse generator																																																												
Mechanical system to assist the round turning process																																																												
Short stay at Pereira, Colombia																																																												
Round turning assisted process experimentation																																																												
Data processing																																																												
Round turning article draft																																																												
3rd. PHASE																																																												
Short stay at Santiago de Chile, Chile																																																												
Manufacture 3rd pulse generator																																																												
Mechanical system to assist the round turning process																																																												
Cold drawing assisted process experimentation																																																												
Data processing																																																												
Cold drawing article draft																																																												
4th. PHASE																																																												
Short stay at Chicago, USA																																																												
Thesis redaction																																																												
Paperwork and thesis defense																																																												

Figure 57: Research activities schedule.

Appendix E

Short research stays

In this appendix, there are listed the research activities for the different short research stays. It is attached the invitation letters and the official stays certificates. Three research stays were done along the thesis, the first one at Technological University of Pereira, Colombia, the second one at Pontifical Catholic University of Chile, Chile, and the last one at Northwestern University, USA. Below, it is detailed the work done in each of those stays.

E.1 Short research stay at Pereira, Colombia

- Institution: Technological University of Pereira.
- Place: Department of Mechanical Engineering.
- Dates: 1 de October 2013 al 1 de December 2013 (total 61 days).
- Supervisor: Dr. Valentina Kallewaard.

The reason for doing this stay was to establish a scientific collaboration with the Department of Mechanical Engineering of the Technological University of Pereira, Colombia. The research activity was focused in the surface properties and power consumption of turning processes assisted by electropulses. The specific tasks of this research collaboration are listed below:

1. Use the equipments, workshops and laboratories from the host university. There are two essential equipments for this research: a power quality analyzer and a lathe with its own foundation.
2. Work with a research team on the electroplasticity field. Currently this research team has a PhD student (Carlos Montilla) who is studying the cutting electroplastic phenomenon. Therefore, the common goal was a collaboration research between the two groups.
3. Learn how to use a power quality analyzer in three-phase electric motors.

The invitation letter and the short research stay certificate are attached as a Figure 58 and Figure 59 respectively.

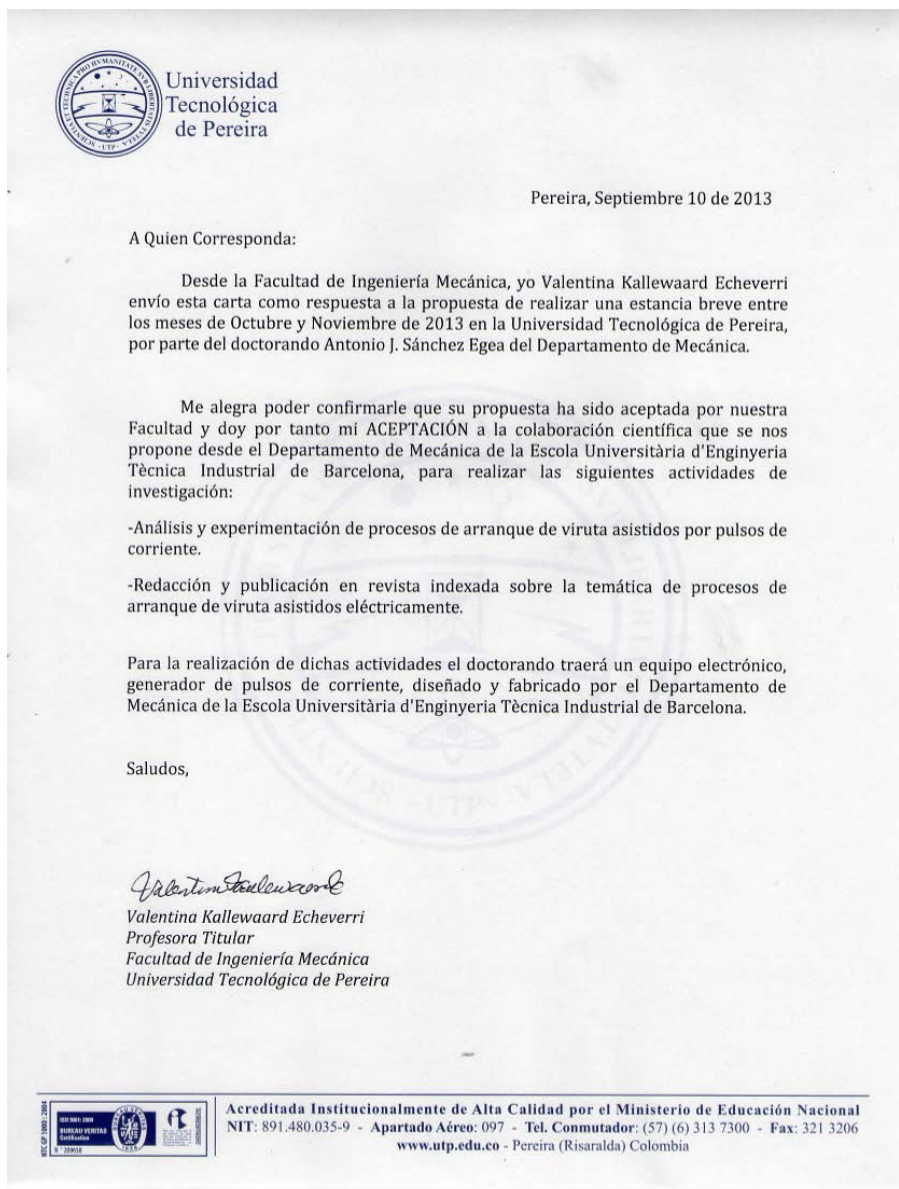


Figure 58: Invitation letter signed by Dr. Valentina Kallewaard.



Universidad
Tecnológica
de Pereira

CERTIFICADO DE REALIZACIÓN DE ESTANCIA BREVE

**EL DECANO DE LA FACULTAD DE INGENIERÍA MECÁNICA DE LA
UNIVERSIDAD TECNOLÓGICA DE PEREIRA (COLOMBIA.)**

CERTIFICA:

Que el doctorando D. Antonio J. Sánchez Egea, con DNI 48519932Y, del Departamento de Mecánica de la Escuela Universitaria de Ingeniería Técnica Industrial de la Universidad Politécnica de Cataluña, ha realizado en este Departamento una estancia breve los meses de Octubre y Noviembre de 2013, bajo la tutela de la profesora Valentina Kallewaard Echeverri.

Durante su estancia ha realizado las siguientes actividades de investigación:

- Análisis y experimentación de procesos de arranque de viruta asistidos por pulsos de corriente.
- Redacción y publicación en revista indexada sobre la temática de procesos de arranque de viruta asistidos eléctricamente.

Y para constancia, a los efectos que procedan, firmo la presente, en Pereira (Colombia) a dieciocho (18) días del mes de noviembre de dos mil trece (2013).

EDUCARDO RONCANCIO HUERTAS

Decano

Facultad de Ingeniería Mecánica



Acreditada Institucionalmente de Alta Calidad por el Ministerio de Educación Nacional
NIT: 891.480.035-9 - Apartado Aéreo: 097 - Tel. Conmutador: (57) (6) 313 7300 - Fax: 321 3206
www.utp.edu.co - Pereira (Risaralda) Colombia

Figure 59: Short research stay certificate of Pereira, Colombia.

E.2 Short research stay at Santiago de Chile, Chile

- Institution: Pontifical Catholic University of Chile.
- Place: Department of Mechanical and Metallurgic Engineering.
- Dates: 1 de April 2014 al 4 de August 2014 (total 126 days).
- Supervisor: Dr. Diego J. Celentano.
- Fund reference: EEBB-I-14-08214.

The relevance of this second research stay is to open a research collaboration line between the Universitat Politècnica Catalunya and the Pontifical Catholic University of Chile. The main objective is to learn how to use a numerical method software (VULCAN) to characterize the conventional manufacturing processes. It is used the metallographic laboratories for tensile tests assays and lattice structure observation. The research activity focuses in the manufacturing improvements of cold wire drawing process assisted by electropulsing.

The specific tasks of this research collaboration are listed below:

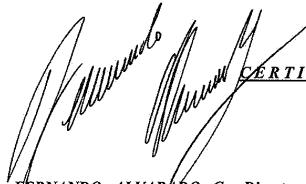
1. Design and manufacture the specific tools to isolate the drawing machine form electricity.
2. Study the electrical and operational parameters of the wire drawing process assisted with current pulses.
3. Perform experiments with this novel manufacturing technique.
4. Analyze the variation of the mechanical properties of the material when it is wire drawn assisted by current pulses.
5. Writing of an article for a Manufacturing Engineering Journal.

The invitation letter and the short research stay certificate are attached as Figure 60 and Figure 61 respectively.



PONTIFICIA
UNIVERSIDAD
CATÓLICA
DE CHILE

VICERRECTORÍA ACADÉMICA
DIRECCIÓN DE RELACIONES ACADÉMICAS INTERNACIONALES



CERTIFICADO

FERNANDO ALVARADO C., Director de Relaciones Académicas Internacionales, certifica que don **Antonio SANCHEZ EGEA**, estudiante de la **Universitat Politècnica de Catalunya** ha sido aceptado para realizar una estadía de investigación de posgrado en la Escuela de Ingeniería de la Pontificia Universidad Católica de Chile (UC) bajo la supervisión del profesor **Diego Celentano** durante el período comprendido entre **Abril y Julio del año 2014**.

Las estadías de investigación no habilitan al alumno a la obtención de Créditos, Grados Académicos o Títulos Profesionales de la UC.

El alumno deberá llegar en la fecha estipulada y deberá portar su seguro de salud obligatorio.

Se otorga la presente certificación a solicitud del interesado, para los efectos del otorgamiento de la visa de estudiante respectiva.

Santiago de Chile, diciembre de 2013.

www.uc.cl

Figure 60: Invitation letter signed by Dr. Diego J. Celentano.



Certificado de realización de estancia breve

**El Prof. Diego Celentano de la Facultad de Ingeniería de la
Pontificia Universidad Católica de Chile**

Certifica:

Que el doctorando D. Antonio J. Sánchez Egea, con DNI 48519932Y, del Departamento de Ingeniería Mecánica de la Escuela Universitaria de Ingeniería Técnica Industrial de la Universidad Politécnica de Cataluña, ha realizado en el Departamento de Ingeniería Mecánica y Metalúrgica de esta Universidad una estancia de 4 meses (abril a Julio del 2014) bajo la tutela del Profesor Dr. Diego J. Celentano.

Durante su estancia ha realizado las siguientes actividades de investigación:

- Estudio del comportamiento mecánico del proceso de trefilado convencional comparado con el proceso de trefilado asistido por pulsos de corriente.
- Fabricación y diseño del utillaje necesario para los ensayos de trefilado asistido con corriente.
- Observación y análisis metalográfico de la red cristalina de los metales trefilado con pulsos de corriente.
- Presentación de un seminario sobre la temática de la electroplasticidad como técnica para asistir procesos de fabricación.
- Redacción de un artículo para ser publicado en una revista indexada sobre la temática investigada durante la estancia.

Y para constancia, a los efectos que procedan, firmo el presente certificado.



Santiago de Chile, 04 de Agosto de 2014.

Figure 61: Short research stay certificate of Santiago de Chile, Chile.

E.3 Short research stay at Chicago, United States

- Institution: Northwestern University.
- Place: Department of Mechanical Engineering.
- Dates: 15 de August 2015 al 15 de December 2015 (total 122 days).
- Supervisor: Dr. Jian Cao.
- Fund reference: EEBB-I-15-09727.

The reason for this short stay is to establish a scientific collaboration with the Department of Mechanical Engineering at the Northwestern University, Chicago, United States. The research activity focuses on a single point incremental forming assisted through short current pulses.


The specific tasks of this research collaboration are listed below:

1. Use the equipments, workshops and laboratories from the host university. There are two essential equipments for this research: double-sided incremental forming tool and a specific numerical software to analyze the mechanical behavior of such process.
2. Work with a research team on the electroplasticity field. Currently this research line is being developed by an entire research group together with some industry consultants, who are doing some research with this novel forming electropulsing technique base on the electroplastic phenomenon.
3. Analyze the material mechanical and metallurgical variation when the incremental forming tool is assisted by current pulses.
4. Obtain some new results worthy to be published in a journal and open a collaboration research line between the two universities is a common goal.

The invitation letter is attached as a Figure 62 in this case.

McCormick Robert R. McCormick
School of Engineering and
Applied Science
Northwestern University
L254 Technological Institute
2145 Sheridan Road
Evanston, Illinois 60208

Office of Graduate Studies and Research
graduate-engineering@northwestern.edu
Phone 847-491-3553
Fax 847-491-5341


NORTHWESTERN
UNIVERSITY

April 6, 2015

Antonio Jose Sanchez Egea
Universitat Politècnica de Catalunya
Departament d'Enginyeria Mecànica
Barcelona, Spain

Dear Antonio Jose Sanchez Egea,


I am pleased to inform you that your appointment as a Visiting Predoctoral Fellow in the Department of Mechanical Engineering for the term August 15, 2015, through December 15, 2015, has been approved by the McCormick School of Engineering & Applied Science. It is our understanding that you will be supported by funds provided from the Ministry of Economy and Competitiveness in Spain.

Your appointment is full time (100%) and, as is true of all research staff appointments in the McCormick School of Engineering and Applied Science, is dependent upon satisfactory performance and the availability of funding.

University policies pertaining to research staff appointees include, but are not limited to, the Patent and Invention Policy, Policy on Staff Conflict of Interest, Policy on Integrity in Research and Procedures for Reviewing Alleged Misconduct, Northwestern University Staff Handbook, Policy on Employment of Relatives, and the University's Human Resources Policies and Procedures Manual. Each of these policies can be found at the Office for Research web page.

I welcome you to Northwestern University, where I hope that your time is both productive and enjoyable. Should you have any questions or problems, please do not hesitate to contact your department.

Sincerely yours,


Richard M. Lueptow
Senior Associate Dean

RML:jed

cc: Department of Mechanical Engineering
Professor Cao

Figure 62: Invitation letter signed by Dr. Jian Cao.

Bibliography

- [1] O. A. Troitskii and V. I. Likhtman, "The Anisotropy of the Action of Electron and gamma Radiation on the Deformation of Zinc Single Crystals in the Brittle State," in *Soviet Physics Doklady*, vol. 8, p. 91. 1963.
<http://www.osti.gov/scitech/biblio/4752610>.
- [2] O. A. Troitskii, "Electromechanical effect in metals," *ZhETF Pisma Redaktsiiu* **10** (1969) 18. <http://adsabs.harvard.edu/abs/1969ZhPmR..10...18T>.
- [3] V. Y. Kravchenko, "Effect of directed electron beam on moving dislocations," *Sov. Phys. JETP* **24** no. 6, (1967) 1135–1142.
http://jetp.ac.ru/cgi-bin/dn/e_024_06_1135.pdf.
- [4] H. Conrad, "Effects of electric current on solid state phase transformations in metals," *Materials Science and Engineering: A* **287** no. 2, (2000) 227–237.
- [5] H. Conrad, "Space charge and the dependence of the flow stress of ceramics on an applied electric field," *Scripta materialia* **44** no. 2, (2001) 311–316.
- [6] K. Okazaki, M. Kagawa, and H. Conrad, "An evaluation of the contributions of skin, pinch and heating effects to the electroplastic effect in titanium," *Materials Science and Engineering* **45** no. 2, (1980) 109–116.
- [7] A. F. Sprecher, S. L. Mannan, and H. Conrad, "Overview no. 49: On the mechanisms for the electroplastic effect in metals," *Acta Metallurgica* **34** no. 7, (1986) 1145–1162.
- [8] H. Song and Z. J. Wang, "Improvement of mechanical properties of cold-rolled commercially pure Ti sheet by high density electropulsing," *Transactions of Nonferrous Metals Society of China* **22** no. 6, (2012) 1350–1355.
- [9] H. Conrad and A. F. Sprecher, *The Electroplastic Effect in Metals, Dislocation in Solids*, vol. 8. F.R.N. Nabarro Elsevier, Amsterdam, 1989.
<https://books.google.es/books?id=eFyhW9SsLikC>.
- [10] D. W. Tang, B. L. Zhou, H. Cao, and G. H. He, "Thermal stress relaxation behavior in thin films under transient laser-pulse heating," *Journal of applied physics* **73** no. 8, (1993) 3749–3752.
- [11] P. D. Goldman, L. R. Motowidlo, and J. M. Galligan, "The absence of an electroplastic effect in lead at 4.2K," *Scripta Metallurgica* **15** no. 4, (1981) 353 – 356.

- [12] R. S. Timsit, "Remarks on recent experimental observations of the electroplastic effect," *Scripta Metallurgica* **15** no. 4, (1981) 461–464.
- [13] O. A. Troitskii, "Pressure shaping by the application of a high energy," *Materials Science and Engineering* **75** no. 1, (1985) 37–50.
- [14] V. B. Kravchenko *Fiz.Tverd.Tela (Leningrad),Sov.Phys. Solid State* **8** no. 1157, (1966) .
- [15] D. Yang and H. Conrad, "Exploratory study into the effects of an electric field and of high current density electropulsing on the plastic deformation of TiAl," *Intermetallics* **9** no. 10–11, (2001) 943–947.
- [16] S. D. Antolovich and H. Conrad, "The Effects of Electric Currents and Fields on Deformation in Metals, Ceramics, and Ionic Materials: An Interpretive Survey," *Materials and Manufacturing Processes* **19** no. 4, (2004) 587–610.
- [17] H. Conrad, "Thermally activated plastic flow of metals and ceramics with an electric field or current," *Materials Science and Engineering: A* **322** no. 1–2, (2002) 100–107.
- [18] M. Molotskii and V. Fleurov, "Magnetic effects in electroplasticity of metals," *Phys. Rev. B* **52** (1995) 15829–15834.
- [19] Z. Xu, G. Tang, S. Tian, F. Ding, and H. Tian, "Research of electroplastic rolling of {AZ31} Mg alloy strip," *Journal of Materials Processing Technology* **182** no. 1–3, (2007) 128–133.
- [20] R. D. Doherty, D. A. Hughes, F. J. Humphreys, J. J. Jonas, D. Juul Jensen, M. E. Kassner, W. E. King, T. R. McNelley, H. J. McQueen, and A. D. Rollett, "Current issues in recrystallization: a review," *Materials Science and Engineering: A* **238** no. 2, (1997) 219–274.
- [21] S. To, Y. H. Zhu, W. B. Lee, X. M. Liu, Y. B. Jiang, and G. Y. Tang, "Effects of current density on electropulsing-induced phase transformations in a Zn–Al based alloy," *Applied Physics A* **96** no. 4, (2009) 939–944.
- [22] Y. Jiang, G. Tang, C. Shek, Y. Zhu, and Z. Xu, "On the thermodynamics and kinetics of electropulsing induced dissolution of B-Mg17Al12 phase in an aged Mg–9Al–1Zn alloy," *Acta Materialia* **57** no. 16, (2009) 4797–4808.
- [23] L. G. Guan, G. Tang, and P. K. Chu, "Recent advances and challenges in electroplastic manufacturing processing of metals," *Journal of Materials Research* **25** (2010) 1215–1224.
- [24] J. Magargee, F. Morestin, and J. Cao, "Characterization of flow stress for commercially pure titanium subjected to electrically assisted deformation," *Journal of Engineering Materials and Technology* **135** no. 4, (2013) 041003.
- [25] J. Zhang, G. Y. Tang, Y. J. Yan, and W. Fang, "Effect of current pulses on the drawing stress and properties of Cr17Ni6Mn3 and 4J42 alloys in the cold-drawing process," *Journal of Materials Processing Technology* **120** no. 1–3, (2002) 13–16.

- [26] V. V. Stolyarov, "Deformability and nanostructuring of TiNi shape-memory alloys during electroplastic rolling," *Materials Science and Engineering: A* **503** no. 1–2, (2009) 18–20.
- [27] G. Tang, J. Zhang, M. Zheng, J. Zhang, W. Fang, and Q. Li, "Experimental study of electroplastic effect on stainless steel wire 304L," *Materials Science and Engineering: A* **281** no. 1–2, (2000) 263–267.
- [28] J. C. Heigel, J. S. Andrawes, J. T. Roth, M. E. Hoque, and R. M. Ford, "Viability of electrically treating 6061 T6511 aluminum for use in manufacturing processes," *Trans. North Am. Manuf. Res. Inst. SME* **33** (2005) 145–152.
- [29] Z. Hu, J. L. Marciniak, and S. J. Duncan, *Mechanics of Sheet Metal Forming (Second Edition)*. Butterworth-Heinemann, Oxford, second edition ed., 2002.
- [30] W. A. Salandro, C. Bunget, and L. Mears, "Electroplastic modeling of bending stainless steel sheet metal using energy methods," *Journal of Manufacturing Science and Engineering* **133** no. 4, (2011) 041008–041018.
- [31] J. J. Jones and L. Mears, "A process comparison of simple stretch forming using both conventional and electrically-assisted forming techniques," *ASME 2010 International Manufacturing Science and Engineering Conference* (2010) 623–631.
- [32] C. R. Green, T. A. McNeal, and J. T. Roth, "Springback elimination for Al-6111 alloys using electrically-assisted manufacturing (EAM)," *Trans. North Am. Manuf. Res. Inst. SME* **37** (2009) 403–410.
- [33] D. Celentano, R. Rosales, and J. Peña, "Simulation and Experimental Validation of Tube Sinking Drawing Processes," *Materials and Manufacturing Processes* **26** no. 5, (2011) 770.
- [34] D. Celentano, E. E. Cabezas, C. M. García, and A. E. Monsalve, "Characterization of the mechanical behaviour of materials in the tensile test: experiments and simulation," *Modelling and Simulation in Materials Science and Engineering* **12** no. 4, (2004) S425.
- [35] D. Hull and D. J. Bacon, *Introduction to Dislocations*. Butterworth Heinemann, Oxford, fourth edition ed., 2001.
<http://dx.doi.org/10.1016/B978-075064681-9/50000-6>.
- [36] D. Roylance, "The Dislocation Basis of Yield and Creep," *Modules in Mechanics of Materials* (2001) 1999–2001.
<http://ocw.mit.edu/courses/materials-science-and-engineering/3-11-mechanics-of-materials-fall-1999/modules/dn.pdf>.
- [37] T. A. Perkins, T. J. Kronenberger, and J. T. Roth, "Metallic forging using electrical flow as an alternative to warm/hot working," *Journal of manufacturing science and engineering* **129** no. 1, (2007) 84–94.
- [38] J. Renjie, Y. Liu, Y. Zhang, X. Dong, Z. Chen, and B. Cai, "Experimental research on machining characteristics of SiC ceramic with end electric discharge milling," *Journal of Mechanical Science and Technology* **25** no. 6, (2011) 1535–1542.

- [39] P. S. Pa, “Design of continuity processes of electrochemical finishing and grinding following turning,” *Journal of Mechanical Science and Technology* **22** no. 11, (2008) 2197–2202.
- [40] D. C. Newman, “Novel uses of electric fields and electric currents in powder metal (P/M) processing,” *Materials Science and Engineering: A* **287** no. 2, (2000) 198–204.
- [41] D. Zhang, S. To, Y. Zhu, H. Wang, and G. Tang, “Static Electropulsing-Induced Microstructural Changes and Their Effect on the Ultra-Precision Machining of Cold-Rolled AZ91 Alloy,” *Metallurgical and Materials Transactions A* **43** no. 4, (2012) 1341–1346.
- [42] H. Hocheng and M. L. Hsieh, “Signal analysis of surface roughness in diamond turning of lens molds,” *International Journal of Machine Tools and Manufacture* **44** no. 15, (2004) 1607–1618.
- [43] K. Liu and S. N. Melkote, “Effect of plastic side flow on surface roughness in micro-turning process,” *International Journal of Machine Tools and Manufacture* **46** no. 14, (2006) 1778 – 1785.
- [44] A. J. Sánchez Egea, H. A. González Rojas, D. J. Celentano, J. A. Travieso-Rodríguez, and J. Llumà i Fuentes, “Electroplasticity-assisted bottom bending process,” *Journal of Materials Processing Technology* **29** no. 4, (2014) 444–450.
- [45] B. Khidhir and B. Mohamed, “Study of cutting speed on surface roughness and chip formation when machining nickel-based alloy,” *Journal of Mechanical Science and Technology* **24** no. 5, (2010) 1053–1059.
- [46] E. Rabinowicz, *Friction and wear of materials*. Wiley, 1965.
<http://books.google.es/books?id=kuVSAAAAMAAJ>.
- [47] M. C. Shaw, *Metal Cutting Principles*. Oxford science publications. Clarendon Press, 1984. <http://books.google.es/books?id=gYcoAQAAMAAJ>.
- [48] P. Muñoz-Escalona and Z. Cassier, “Influence of the critical cutting speed on the surface finish of turned steel,” *Wear* **218** no. 1, (1998) 103–109.
- [49] H. Gokkaya, “The effects of machining parameters on cutting forces, surface roughness, built-up edge (BUE) and built-up layer (BUL) during machining AA2014 (T4) alloy,” *Journal of Mechanical Engineering* **56** no. 9, (2010) .
http://ojs.sv-jme.eu/index.php/sv-jme/article/view/140_DOI_not_assigned.
- [50] T. Sata and M. C. Shaw, “Behavior of cellular materials undergoing plastic flow,” *CIRP Annals* **12** no. 190, (1964) .
- [51] G. Boothroyd, *Fundamentals of Metal Machining and Machine Tools, Third Edition*. Taylor & Francis, 1988. <http://books.google.es/books?id=sMmqNKc1BV8C>.
- [52] R. S. Pawade, A. S. Harshad, and S. S. J., “An analytical model to predict specific shear energy in high-speed turning of Inconel 718,” *International Journal of Machine Tools and Manufacture* **49** no. 12–13, (2009) 979–990.

- [53] R. Sood, C. Guo, and S. Malkin, "Turning of hardened steels," *Journal of manufacturing processes* **2** no. 3, (2000) 187–193.
- [54] S. H. Talbert and B. Avitzur, *Elementary mechanics of plastic flow in metal forming*. Wiley, 1996. <http://books.google.es/books?id=Uu9TAAAAMAAJ>.
- [55] L. Dalong and Y. Enlin, "Computation method of metal's flow stress for electroplastic effect," *Materials Science and Engineering: A* **505** no. 1–2, (2009) 62 – 64.
- [56] G. Tskhondiya and N. Beklemishev, "Simulating the effect of a high density electric current pulse on the stress field during plastic deformation," *International Journal of Material Forming* **5** no. 2, (2012) 157–162.
- [57] H. Xie, Q. Wang, K. Liu, F. Peng, X. Dong, and J. Wang, "Investigation of influence of direct-current pulses on springback during V-bending of AZ31B magnesium alloy sheet," *Journal of Materials Processing Technology* **219** (2015) 321–327.
- [58] J. H. Roh, J. J. Seo, S. T. Hong, M. J. Kim, H. N. Han, and J. T. Roth, "The mechanical behavior of 5052-H32 aluminum alloys under a pulsed electric current," *International Journal of Plasticity* **58** no. 0, (2014) 84–99.
- [59] A. J. Sánchez Egea, H. A. González Rojas, C. Montilla Montaña, and V. Kallewaard Echeverri, "Effect of electroplastic cutting on the manufacturing process and surface properties," *Journal of Materials Processing Technology* **222** (2015) 327–334.
- [60] X. Ye, J. Kuang, X. Li, and G. Tang, "Microstructure, properties and temperature evolution of electro-pulsing treated functionally graded Ti–6Al–4V alloy strip," *Journal of Alloys and Compounds* **599** no. 0, (2014) 1–9.
- [61] K. Liu, X. Dong, H. Xie, and F. Peng, "Effect of pulsed current on the deformation behavior of AZ31B magnesium alloy," *Materials Science and Engineering: A* **623** no. 0, (2015) 97–103.
- [62] R. Zhu, G. Tang, S. Shi, and M. Fu, "Effect of electroplastic rolling on deformability and oxidation of NiTiNb shape memory alloy," *Journal of Materials Processing Technology* **213** no. 1, (2013) 30–35.
- [63] G. Vander Voort and A. I. H. Committee, *ASM Handbook*. ASM International, 2004. <https://books.google.es/books?id=W0dLAQAIAAJ>.
- [64] Q. Xu, G. Tang, Y. Jiang, G. Hu, and Y. Zhu, "Accumulation and annihilation effects of electropulsing on dynamic recrystallization in magnesium alloy," *Materials Science and Engineering: A* **528** no. 7–8, (2011) 3249–3252.
- [65] K. Amar, C. David, C. Martin, G. John, and K. David, "Quantitative measurement of deformation-induced martensite in 304 stainless steel by X-ray diffraction," *Scripta Materialia* **50** (2004) 1445–1449.

- [66] J. Jorba Peirò, *Transformación inducida por plasticidad como procedimiento para mejorar la tenacidad de rotura del acero F-140 C de alto límite elástico*, vol. Thesis doctoral. Publicacions Universitat de Barcelona, 1990.
- [67] F. P. Incropera and D. P. DeWitt, *Fundamentals of Heat and Mass Transfer*. John Wiley and Sons, 1985. <http://www.abebooks.com/Fundamentals-Heat-Mass-Transfer-2nd-Incropera/2803926474/bd>.